

© 2018 by Yu-Tsun Shao. All rights reserved.

DETERMINATION OF LOCAL CRYSTAL SYMMETRY IN COMPLEX, MULTI-
ELEMENT, FERROELECTRIC PEROVSKITES AND ALLOYS

BY

YU-TSUN SHAO

DISSERTATION

Submitted in partial fulfilment of the requirements
for the degree of Doctor of Philosophy in Materials Science and Engineering
in the Graduate College of the
University of Illinois at Urbana-Champaign, 2018

Urbana, Illinois

Doctoral Committee:

Professor Jian-Min Zuo, Chair
Professor James Eckstein
Assistant Professor Daniel Shoemaker
Assistant Professor André Schleife

ABSTRACT

Structural change arising from correlated lattice and charge interaction in complex, multi-element, crystals has a profound effect on their physical properties. Examples include charge ordering in complex oxides, polarization nanodomains in ferroelectrics, and vortex matter. A common scheme to these systems is that there exists a distinction between local crystal symmetry and the average, macroscopic symmetry imposed by fluctuations in the crystal lattice. Before we can control and exploit these fluctuation-induced emergent properties, the crucial first step is to fully characterize any correlation that may exist.

This thesis explores the crystallographic aspect of local charge, polarization, and lattice interactions in complex, multi-element, crystals by developing scanning convergent beam electron diffraction (SCBED) based techniques. The applications of SCBED characterization demonstrated here include: ferroelectric BaTiO₃ single crystal, relaxor-ferroelectric (1-x)Pb(Zn_{1/3}Nb_{2/3})O₃-xPbTiO₃ (x=0.08) single crystal, and multi-principal-element alloy Al_{0.1}CrFeCoNi.

First, we show the local crystal symmetry and polarization fluctuations in BaTiO₃ single crystals as determined using SCBED. An improved algorithm for CBED symmetry quantification is used to map the ferroelectric domains and local symmetry across the ferroelectric phase transition temperatures. The symmetry in BaTiO₃ was found inhomogeneous; regions of a few tens of nanometers retaining almost perfect symmetry are interspersed in regions of lower symmetry. The SCBED results suggest the coexistence of displacive and order-disorder phase transition, affected upon by the local

structure.

Next, we examine the local symmetry, polarization nanodomains, and the domain wall (DW) structures in relaxor-ferroelectrics. Nanometer-sized domains having the monoclinic Pm symmetry in PZN-8%PT single crystals are identified by performing SCBED along the [100], [001], and [111] zone axes. Intensity distribution in the (000) disks in the CBED patterns is used to determine lattice-rotation at the precision of $\pm 0.012^\circ$ by performing SCBED on a standard Si sample. A careful examination of the polarization DWs revealed the presence of lattice-rotation vortices of $\sim 15\text{nm}$ in diameter in PZN-8%PT, which can be attributed to bound charge discontinuity and depolarization fields.

The lattice distortion effect in high entropy alloys (HEAs) is explored as a model of multi element alloys. Lattice distortion is one of the four core effects of HEAs, which results from different atom sizes and influences solid solution hardening. However, so far quantification of lattice distortion effects by X-ray and neutron diffraction has provided contradictory results. Using SCBED, we visualize the sub-nanometer strain fluctuations and local symmetry breaking in single phase $\text{Al}_{0.1}\text{CrFeCoNi}$. Our results reveal $10\pm 3\text{nm}$, disc-shaped, clusters having $\sim 7.1\%$ tensile displacements along $\langle 110 \rangle$ directions distributed throughout the specimen; local strain, on the contrary, was found to be fluctuating within $\pm 1.3\%$ and slow-varying over $\sim 50\text{nm}$. The observed inhomogeneous lattice distortion using scanning electron diffraction thus provides a new perspective on structure and property relations in multi-principal-element systems.

To my parents Syou and Thomas, my sisters Annie and Joy.

ACKNOWLEDGEMENTS

I am extremely grateful to my advisor, Professor Jian-Min Zuo, for his generous advices throughout my PhD study and research, for giving me the opportunity to enjoy the fun of technique development and problem solving, and for being exceptionally supportive of developing my young scientific career across continents. He has inspired me of not only for exploring challenges in materials characterization, but also the enthusiasm and rigorous attitude towards scientific research. I could still recall one of his advices during a dinner conversation: “Science is about trust. Because most people don’t have access to the technique or samples, we have to be extremely careful about the interpretations on the experimental results and what we claim.”

I would like to thank my thesis committee members, Prof. James Eckstein, Prof. Daniel Shoemaker and Prof. André Schleife. I would also like to thank Prof. Tai-Chang Chiang and Prof. Waltraud Kriven for serving on my preliminary exam committee. They have provided me helpful discussions and encouragements. I would like to thank Prof. David Payne and Prof. Kenji Tsuda for the helpful discussions on ferroelectrics, and Prof. Robert Averback for the discussion on high entropy alloys.

I am thankful to many collaborators for all the inspiring discussions and providing me various perspectives: Prof. Paul Braun, Dr. Huigang Zhang, Dr. Hailong Ning, Prof. Hong Yang, Dr. Yung-Ting Pan, Prof. Les Allen, and Dr. Zichao Ye from UIUC; Prof. Beatrice Noheda and Dr. Arnoud Everhardt from University of Groningen, The Netherlands. I wish to give special thanks to Prof. Philip Nakashima, Prof. Laure Bourgeois, and Tianyu Liu from Monash University, Australia; Prof. Randi Holmestad and Maryam Vatanparast from Norwegian University of Science and Technology,

Norway; they have made my two summer research exchanges far more fruitful and enjoyable than ever imagined.

I wish to thank all Zuo's past and current group members, Dr. Jihwan Kwon, Dr. Jianbo Wu, Dr. Wenpei Gao, Dr. Honggyu Kim, Dr. Hyuk Kim, Dr. Yifei Meng, Dr. Yang Hu, Dr. Qun Yang, Dr. Xun Zhan, Aram Yoon, Renliang Yuan, Haw-Wen Hsiao, Jocelyn Lai, and Saran Pidaparthi. They helped me in many ways throughout the years and made the life at this small town enjoyable. I thank Dr. James Mabon, Dr. Changqiang Chen, Dr. Honghui Zhou, and Dr. Waclaw Swiech for training me on TEMs. I thank the staff at MRL for their assistance on many occasions.

A collective, big and warm thank to the "CCC" basketball team members and affiliates at UIUC: Dr. Lewis Tseng, Dr. Chih-Chi Chu, Dr. Jun-Li Lin, Hsiao-Hsuan Liu, Dr. Curtis Wang, Sean Yu, Dr. Kai-Wen Hsiao, Dr. Amy Chu, Dr. Michael Liu, and Yu-Chun Yen. We have defeated many opponents and obtained many trophies, and motivated each other whether we have won or lost the game. After all, tomorrow is another day (that usually starts with a tough hangover).

Last but not least, I would like to thank my whole family for being supportive, including invaluable feedback on figure color scheme and layout from artists' perspective. Finally, I would like to send my special gratitude to my dear girlfriend Gina Hu, for her support and understanding. Without my loved ones, this thesis wouldn't exist.

TABLE OF CONTENTS

CHAPTER 1: INTRODUCTION.....	1
1.1 Ferroelectricity and crystallographic symmetry.....	4
1.2 BaTiO ₃	9
1.3 (1-x)Pb(Zn _{1/3} Nb _{2/3})O ₃ -xPbTiO ₃	10
1.4 Al _{0.1} CrFeCoNi.....	13
1.5 Motivation and organization of this thesis.....	15
1.6 References.....	17
CHAPTER 2: SCANNING CONVERGENT BEAM ELECTRON DIFFRACTION.....	23
2.1 Transmission electron diffraction.....	23
2.2 Illumination semi-convergence angle α	24
2.3 Probe size.....	27
2.4 Beam scanning system.....	29
2.5 Operation procedures.....	31
2.6 Symmetry quantification.....	36
2.7 CBED simulation.....	41
2.8 References.....	43
CHAPTER 3: NANOSCALE SYMMETRY FLUCTUATIONS IN FERROELECTRIC BARIUM TITANATE, BaTiO ₃	45
3.1 Introduction.....	46
3.2 Experimental methods.....	49
3.3 Results.....	52
3.4 Discussion.....	58

3.5 Conclusions.....	61
3.6 References.....	62
CHAPTER 4: LATTICE ROTATION VORTEX AT THE MONOCLINIC DOMAIN BOUNDARY IN RELAXOR FERROELECTRIC CRYSTAL.....	66
4.1 Introduction.....	66
4.2 Experimental methods.....	68
4.3 Results.....	71
4.4 Discussion.....	77
4.5 Conclusions.....	80
4.6 References.....	81
CHAPTER 5: DIRECT IMAGING OF DISTORTED LATTICE IN A HIGH ENTROPY ALLOY.....	85
5.1 Introduction.....	86
5.2 Experimental methods.....	88
5.3 Results.....	91
5.4 Discussion.....	101
5.5 Conclusions.....	104
5.6 References.....	105
CHAPTER 6: SUMMARY AND OUTLOOKS.....	109
6.1 Summary.....	109
6.2 Outlooks.....	110
6.2.1 Quantitative refinement of SCBED: SQCBED.....	110
6.2.2 Rocking beam SCBED: SRCBED.....	111
6.2.3 Time-resolved SCBED.....	112
6.3 References.....	113

APPENDIX A: DM SCRIPT FOR SCBED.....	114
A.1 Scanning electron diffraction acquisition.....	114
A.2 Symmetry quantification.....	122
 APPENDIX B: PYTHON SCRIPT FOR CBED SIMULATION.....	 143
B.1 CBED simulation of $\text{Al}_{0.1}\text{CrFeCoNi}$ with random displacements	143
 APPENDIX C: INPUT DATA FILES FOR CBED SIMULATION.....	 145
C.1 Data file of $(1-x)\text{Pb}(\text{Zn}_{1/3}\text{Nb}_{2/3})\text{O}_3-x\text{PbTiO}_3$ ($x=0.08$).....	145
C.2 Data file of tetragonal BaTiO_3	145
C.3 Data file of FCC $\text{Al}_{0.1}\text{CrFeCoNi}$	146

CHAPTER 1

INTRODUCTION

This thesis focuses on nanoscale characterization of correlated local order or disorder in the relaxor-ferroelectric and high entropy alloy crystals based on the improved scanning convergent beam electron diffraction (SCBED) techniques, as implemented in a transmission electron microscope (TEM). Diffraction in general forms the basis of crystal structures determination, where diffraction patterns are obtained by scattering of X-rays, neutrons or electrons. Scattering from a ordered structure, whether it is a crystal, a quasicrystal, or even an incommensurately modulated crystal, produces a set of sharp diffraction spots; while diffraction patterns recorded from liquids or glasses show continuous broad rings with no sharp diffraction spots at all. In between the aforementioned two extremes, scattering from crystals with correlated order/disorder gives rise to diffraction patterns having discrete Bragg reflections as well as continuous diffuse scattering. The diffuse scattering reflects the correlations of local structural order. However, the interpretation of such patterns is challenging (1).

The local structural disorder results from correlated lattice, spin, and charge interactions in complex, multi-element crystals, and often gives rise to exceptional properties. Examples include charge ordering in complex oxides (2), spontaneous polarization in ferroelectrics (3, 4), vortex matter (5), and unconventional superconductivity (6). These interactions must be understood in order to optimize and

design new functional materials based on the emergent properties. For example, barium titanate was discovered as ferroelectric and used for sonar during the World War II, yet the exact phase transition mechanism features local crystal symmetry breaking is still not fully understood; the relaxor-ferroelectric with polarization nanodomains show giant electromechanical response that is important for transducers, medical imaging, and nanoelectronic devices applications; the multi-principal element high entropy alloys are promising materials for their excellent thermomechanical properties and irradiation resistance. Thus, the outstanding experimental challenge is to image and characterize quantitatively the local structure and order parameters of materials with correlated disorder.

Ferroelectric perovskites are characterized by a non-volatile electric dipole moment, the spontaneous polarization P_s vector, whose direction can be switched under the constraints of the crystal space group. Analogous to ferromagnets, ferroelectric samples often comprise domains with different orientation of the polarization depending on the local electromechanical boundary conditions. The interface between domains, known as domain walls, can contribute significantly to ferroelectric switching as well as adopt novel properties such as the formation of conducting planes in insulators (7, 8). Relaxor ferroelectrics are solid solutions between relaxors and ferroelectric crystals, characterized by the high dielectric permittivity over a broad temperature range. The relaxor-ferroelectrics exhibit exceptional piezoelectric response (9), which their nm-sized domains

and disordered polar nanoregions have been regarded as “hopeless mess” for structural characterization (10, 11).

Multi-principal element alloys, including high entropy alloys (HEAs), is another interesting class of material with local disorder due to their exceptional mechanical properties at cryogenic and elevated temperatures (12, 13). HEAs are composed of five or more elements of equal or near-equal molar percentage, resulting in a large contribution of mixing entropy in the Gibbs free energy that stabilizes a single solid solution phase (14, 15). Due to the varying sizes of the constitutive elements coordinated at the same crystallographic site, HEAs are expected to have severe lattice distortion. However, systematic and quantitative studies of lattice distortion are still missing due to lack of the suitable probe (13, 16).

In what follows, we introduce the key concepts of ferroelectricity and crystallography, as well as the materials presented in this thesis: BaTiO_3 , $(1-x)\text{Pb}(\text{Zn}_{1/3}\text{Nb}_{2/3})\text{O}_3-x\text{PbTiO}_3$, and $\text{Al}_{0.1}\text{CrFeCoNi}$. The central focus of this thesis, whether one can determine the local crystal structure in complex multi-element crystals, is raised and discussed in terms of local crystal symmetry associated with physical order parameters. Finally, this chapter ends with a brief summary of the organization of this dissertation and the findings within this document.

1.1. Ferroelectricity and Crystallographic Symmetry

When subjected to an applied stress, crystals undergo a small change in dimensions and develop a small strain. Some crystals develop electric polarization when strained under the applied stress, which is known as the ‘direct’ *piezoelectric* effect. Piezoelectric crystals also show a ‘converse’ effect, which the strain would develop proportional to an applied electric field. Crystals in general are classified by their symmetry. There are 32 point groups and thus 32 classes of crystals according to their point symmetry. Among the 32 crystal classes, 11 possess center of symmetry (Fig. 1.1). For centrosymmetric crystals, the applied stress results in symmetrical atomic displacements, in which the center of positive charge coincides with the center of negative charge, hence exhibit no polar properties. Of the remaining 21 non-centrosymmetric crystal classes, 20 of these possess polar axis and exhibit the piezoelectric effect. Of the 20 piezoelectric crystal classes, 10 of these have a unique polar axis, which mean they meet the necessary conditions to be *pyroelectric*. These crystals are called *polar* because they possess a spontaneous polarization (P_s). Therefore, if pyroelectric crystals have a spontaneous polarization along unique polar axes they will exhibit temperature dependent changes in the spontaneous polarization. Finally, a small subset of crystals within the pyroelectric crystal class have two or more orientation states in the absence of external electric field, and can be switched between these states by an applied electric field are *ferroelectric* (17).

Crystal system	Triclinic	Monoclinic	Orthorhombic	Tetragonal	Trigonal	Hexagonal	Cubic
32 Point groups	1	2	222	4	3	6	23
	$\bar{1}$	m	$2mm$	$\bar{4}$	$\bar{3}$	$\bar{6}$	$\frac{2}{m}\bar{3}$
		$\frac{2}{m}$	mmm	$\frac{4}{m}$	322	$\frac{6}{m}$	432
				422	$3m$	622	$\bar{4}3m$
				$4mm$	$\bar{3}m$	$6mm$	$\frac{4}{m}\bar{3}\frac{2}{m}$
				$\bar{4}2m$		$\bar{6}2m$	
				$\frac{4}{m}mm$		$\frac{6}{m}mm$	

:Piezoelectric Crystal Class
 :Polar Crystals

Figure 1.1. Hierarchy of the 32 crystallographic classes. Blue box and red circles indicate piezoelectric and polar crystal classes, respectively.

A more rigorous definition of the ferroelectricity is based on the pyroelectric coefficient, i.e., the change of polarization with respect to temperature. When an electric field \mathbf{E} is applied to a polar material the total electric displacement \mathbf{D} is given by

$$\mathbf{D} = \varepsilon_0 \mathbf{E} + (\mathbf{P}_s + \mathbf{P}_{induced}) = \varepsilon \mathbf{E} + \mathbf{P}_s \quad (1.1)$$

Therefore

$$\frac{\partial \mathbf{D}}{\partial T} = \frac{\partial \mathbf{P}_s}{\partial T} + \mathbf{E} \frac{\partial \varepsilon}{\partial T} \quad (1.2)$$

, where $\vec{p} = \partial \mathbf{P}_s / \partial T$ is the pyroelectric coefficient, a vector. The crystallographic symmetry places strict restrictions on the orientation of \vec{p} . Ferroelectric phase transition is defined by the crystal undergoing from a high-temperature, high symmetry phase to a low-temperature, low symmetry phase in which the vector of pyroelectric coefficients acquires

new components which were zero in the high-symmetry phase (18). Similarly, a crystal is considered *ferroelastic* if the phase transition results in a low symmetry phase in which the second-rank thermal dilatation tensor α_{ij} changes the number of its independent components with respect to those in the high symmetry phase (19). Therefore, the change in the tensor α_{ij} is associated with the change of the unit cell dimension. In the phenomenological theory of phase transition (Landau theory), the physical quantity which appears in the lower symmetry phase and is fully responsible for the symmetry change is called the *order parameter* of the transition.

Perovskite oxides are widely studied and technologically important because the versatile structure can accommodate a wide variety of cations, which leads to a wide range of properties, including ferroelectricity, ferromagnetism and colossal magnetoresistance, piezoelectricity, multiferroicity, and metal-insulator transitions (20). Perovskite ferroelectrics of the form ABO_3 can be represented by 8 corner sharing A-site cations, 6 oxygen atoms at face centers, and a B-site cation at body center (inside an oxygen octahedron). The high-temperature paraelectric phase has a primitive cubic structure of $Pm\bar{3}m$, as shown in Fig. 1.2. Upon cooled down from high temperature through the Curie temperature T_c , the material undergoes a structural distortion where the ions are displaced, resulting in the symmetry lowering and a net dipole moment. Figure 1.2 shows an example of the tetragonal distortion, where the A-site displacement produces a tetragonal distortion

in the unit cell, and the displacements of B-site and oxygen atoms lead to a non-zero polarization along the c-axis.

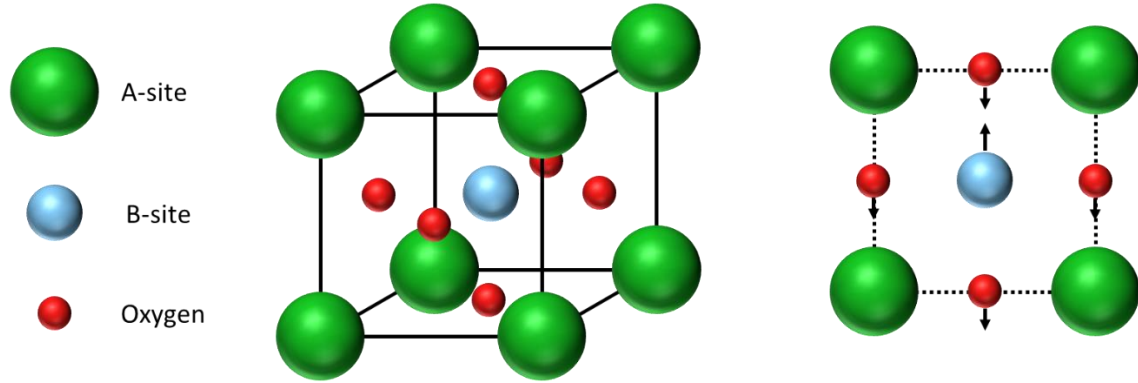


Figure 1.2. Schematic drawing of the perovskite structure in the cubic paraelectric phase above Curie temperature (left) and the tetragonal distortion occurring below the Curie temperature (right).

The perovskite structure is extremely flexible enabling a wide variety of A- and B-site cations with various valence states and defect chemistries of up to a few percent (21). From a geometric perspective, the resulting structure depends on the atomic radii of the A- and B-site cations, which can be predicted by calculating the Goldschmidt tolerance factor

$$t = \frac{R_o + R_a}{\sqrt{2}(R_o + R_b)} \quad (1.3)$$

, where R_o , R_a and R_b are the atomic radii of the oxygen, A-site and B-site cations, respectively (22). Goldschmidt has shown that the perovskite structure is formed when $t \approx 1$. For $t > 1$, the unit cell dimension is imposed by the distance $R_o + R_a$ and the B-site cation is too small for the octahedron, which the structure would develop a small polar

distortion. For $t < 1$, the A-site cation is small compared to the hole in oxygen octahedra, meaning the A-site cation cannot effectively bond with all 12 neighboring oxygens. In perovskites with low tolerance factors, the octahedral rotations help to optimize the coordination environment of the A-site cations which suppress ferroelectricity (23). An example is the *Pnma* space group, which is a commonly adopted structure for ABO_3 perovskites with octahedral rotations.

Another form of ferroelectric distortions is a result of symmetry breaking displacements of the B-site cation within the oxygen octahedra. The B-site driven ferroelectricity can be described by a second-order Jahn-Teller distortion, which involves a delicate balance between short-range forces and long-range Coulomb interactions. The long-range Coulomb interactions favor ferroelectric state, while short-range repulsions between charged ions are minimized for centrosymmetric structures. In the case of $BaTiO_3$, the hybridization of Ti $3d$ and O $2p$ orbital is essential for stabilizing the ferroelectric distortion, while the Ba $5p$ orbital remains stereochemically inactive. On the other hand, $PbTiO_3$ is a more robust ferroelectric with A-site driven ferroelectric distortion, where the hybridization of Pb $6s$ orbital lone-pair electrons with the O $2p$ orbitals resulted an increase of the tetragonality of the unit cell (24).

1.2. BaTiO₃

Barium titanate (BaTiO₃) is the first perovskite compound being identified as ferroelectric (25). Macroscopically, it has a cubic structure of $Pm\bar{3}m$ in the high temperature paraelectric phase. Upon cooling down, it successively transforms from a cubic phase to tetragonal (T) phase of $P4mm$ at 393K, then to orthorhombic (O) structure of $Amm2$ at 278K, and to the low-temperature rhombohedral (R) phase of $R3m$ at 183K (26).

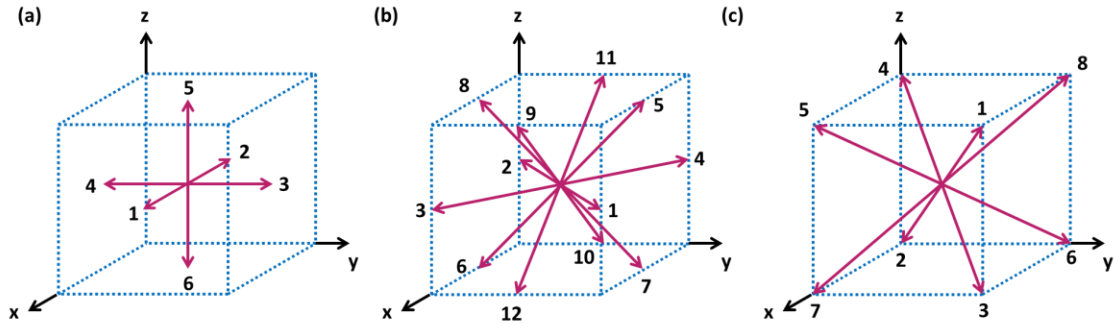


Figure 1.3. Schematic drawing of the domain states of BaTiO₃ in (a) tetragonal phase $4mm$, (b) orthorhombic phase $mm2$, and (c) rhombohedral phase $3m$. The red arrows with numbers represent the P_s vectors (redrawn after ref (18)).

The symmetry permissible polarization orientations in each ferroelectric phase of BaTiO₃ are different, hence the different domain configurations. For example, Fig. 1.3 shows the polarization along the $\langle 100 \rangle$, $\langle 110 \rangle$ and $\langle 111 \rangle$ directions corresponding to the directions of the atomic displacements in T, O, R phases, respectively. The domain configuration can be characterized by the angles between the respective P_s vectors, for T

phase the 180° (1,2) and 90° (1,3) domains; in O phase 180° (1,2), 90° (1,3), 60° (11,5), and 120° (11,7) domains; and for R phase the 180° (1,2), 71° (1,2), and 109° (1,4) domains [Fig.1.3]. In real crystals, the domain configuration is subjected to the mechanical (strain) and electrical (charge) boundary conditions (27, 28). The details of domain structures characterization and the phase transition mechanism will be discussed in Chapter 3.

1.3. (1-x)Pb(Zn_{1/3}Nb_{2/3})O₃-xPbTiO₃

Relaxor ferroelectrics are site- and charge-disordered solid solutions between relaxors and ferroelectric crystals. The name ‘relaxor’ came from the high dielectric permittivity over a broad temperature range, whereas in conventional ferroelectrics the permittivity is peaked around the Curie temperature (29). Lead-based relaxor ferroelectric perovskites having the formula $(1-x)Pb(B'_{1/3}B''_{2/3})O_{3-x} - xPb(B'''+4)O_3$ ($B', B'', B''' = \text{Zn, Nb, Ti}$ for PZN-PT, and Mg, Nb, Ti for PMN-PT) exhibit exceptional piezoelectric properties (9) near the morphotropic phase boundary (MPB), which is useful for transducer and ultrasound applications. Fig. 1.4 show the dielectric constant d_{33} as a function of composition, where the piezoelectric constant is defined as $d_{ij} = \frac{\text{Induced strain along direction } i}{\text{Applied field along direction } j}$. The MPB refers to a chemically driven change in phase, and is defined in a narrow composition region between the rhombohedral (R) $R3m$ and tetragonal (T) $P4mm$ phases, at lower x and higher x, respectively. For PMN-xPT, the MPB lies in the region of x=28~35% (30, 31), and the reported x=8~11% for PZN-xPT (32-34).

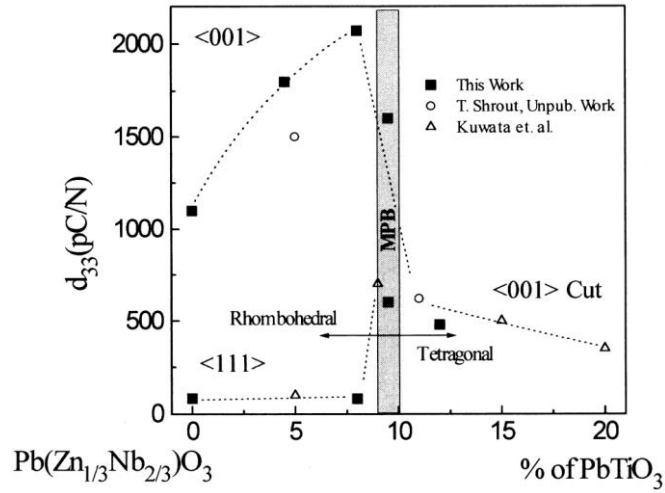


Figure 1.4. Piezoelectric constant d_{33} as a function of crystal composition and orientation in PZN-PT published in ref (34).

For relaxor-ferroelectric such as PZN-xPT and PMN-xPT, it is still unclear how underlying polar structure gives rise to their properties, including unusually large electromechanical response and high permittivity over a broad temperature range. A model of local inhomogeneities known as polar nanoregions (PNRs) inside a non-polar matrix has been widely used to describe the structure of relaxor-ferroelectrics. The inhomogeneities arise from chemical and valence mixing at the B cation site in the perovskite structure. While the PNR is evidenced by strong X-ray diffuse scattering (35) and piezoresponse force microscopy measurements (36), recent studies have questioned the validity of this model (37, 38). The butterfly shape in the diffuse scattering pattern can be reproduced by molecular dynamics simulations of a multi-domain structure, consisted of domains having sizes of 2-10 nanometers (11).

Nanometer-sized monoclinic domains has been reported by X-ray diffraction (39, 40), neutron diffraction (41-45), and electron microscopy (46, 47) for PZN-xPT in the MPB region. Suggested by the polarization model, the presence of monoclinic phases ease the polarization rotation from rhombohedral to tetragonal phases (48, 49). However, recent CBED results suggested the local structure of PMN-31%PT is triclinic, but showed monoclinic Cm symmetry when averaged over a volume of larger than $\sim 4.7 \times 10^3 \text{ nm}^3$ (47, 50, 51).

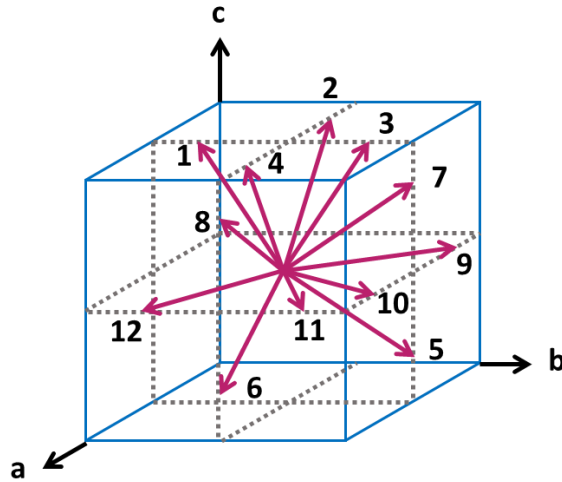


Figure 1.5. Schematic drawing of the possible domain states of monoclinic phase Pm . The red arrows with numbers represent the P_s vectors (redrawn after ref (52)).

For the monoclinic phase Pm , there are 24 symmetry permissible polarization orientations. For example, Fig. 1.5 shows the polarization along the representative 12

$\langle u0v \rangle$ directions corresponding to the directions of the atomic displacements. The directions between adjacent domains usually satisfy the mechanical compatibility and electrical neutrality conditions. In real crystals, the domain walls may be misoriented relative to the permissible directions predetermined by mechanical conditions (28, 52). The characterization of monoclinic nanodomains and their disinclination strain will be detailed in Chapter 4.

1.4. $\text{Al}_{0.1}\text{CrFeCoNi}$

High-entropy alloys (HEAs) are a new class of materials characterized by their unconventional compositions, which comprise 5 or more principal alloying elements in equimolar or near equimolar fraction. The rationale for the alloy design is that the large contribution of mixing entropy to the Gibbs free energy stabilizes a single solid solution phase (14, 15). HEAs have attracted much research attention for their interesting mechanical, electronic, and magnetic properties (14, 15, 53). For example in $\text{Al}_x\text{CrFeCoNi}$ system, the Al contents have a large effect on the crystal structure. At low Al contents, the as-cast $\text{Al}_x\text{CrFeCoNi}$ alloy adopt fcc crystal structure, which changes to bcc structure as Al contents increase (54-59). HEAs such as $\text{Al}_x\text{CrFeCoNi}$ alloys also show exceptional structural stability under irradiation (12, 60-62), suggesting self-healing properties such as local melting and recrystallization happen easily under irradiation, wiping out much of structural defects.

The severe lattice distortion effect is one of the core effects for describing HEAs (63). Due to the various atomic sizes of elements in a concentrated solution, one would speculate that the constituent atoms would inevitably be displaced away from their ideal lattice positions. The lattice distortion is claimed to be more severe than in conventional alloys, contribute to excess entropy, and impede dislocation movements and lead to pronounced solid solution strengthening (13, 16, 64-66).

Due to the lack of suitable structural characterization approaches, however, the exact nature of lattice distortion effect in MPEAs is still unknown (13, 16, 65, 66). For single phase solid solution HEAs, the reported X-ray and neutron diffraction studies have shown sharp Bragg peaks belonging to a simple Bravais lattice (53, 55, 58). The Debye-Waller factors determined by the Rietveld refinement analysis, however, are noticeably larger than that expected for the thermal Debye-Waller factors, consistent with local lattice distortions (65, 67, 68). Furthermore, the X-ray or neutron total scattering and extended X-ray absorption fine structure (EXAFS) analysis suggests short-range ordering (SRO) and strong distortion away from the average Bravais lattice (69-74). While X-ray and neutron diffraction are highly quantitative, the main drawback of such studies is the difficulty in distinguishing between ordered and disordered phases with the same base crystal structure. The characterization of local symmetry and strain will be detailed in Chapter 5.

1.5. Motivation and organization of this thesis

The above discussions introduces the structure of ferroelectric crystals, their symmetry and structure-property relations. Local structures of ferroelectrics such as polarization nanodomains play an important role on their piezoelectric properties. Determination of local structure requires a general and robust method having spatial resolution at nanometer scale. To meet the challenges in characterizing local crystal structure, the major motivation associated with this research are 1) to develop a general method, or a ‘local probe’, for the determination of crystallographic symmetry at nanometer resolution, 2) to automate the data analysis for extracting structural information, and 3) to correlate local crystal symmetry variations with underlying materials physics.

In this thesis, we report on the development of scanning convergent beam electron diffraction (SCBED) for probing local structure. SCBED is a technique based on CBED, which takes the advantages of the dynamical diffraction effects, or strong interaction between electron and crystal potential, and the high resolution nature due to the small wavelength of high energy electrons. We have further improved this technique for local symmetry and strain analysis in complex, multi-element crystals.

The thesis is organized in 6 chapters. Chapter 2 introduces the principles of the SCBED technique that is used throughout this thesis as the main characterization technique. Experimental details and algorithms for extracting structural information are presented in Ch. 2. Chapters 3-5 describe the applications of SCBED to different materials. Chapter 3

investigates the nanoscale fluctuations of the ferroelectric phase transition order parameter in single crystal BaTiO_3 . Chapter 4 discusses about the symmetry determination of nanodomains in PZN-8%PT and the discovery of a new type of defect, lattice-rotation vortex. Chapter 5 describes the study of local lattice distortion in $\text{Al}_{0.1}\text{CrFeCoNi}$. The local crystal symmetry and strain are directly visualized using SCBED and a sub-nanometer electron probe. Conclusions along with discussions on future perspectives are described in Chapter 6.

1.6 References

1. D. A. Keen, A. L. Goodwin, The crystallography of correlated disorder. *Nature* **521**, 303 (May 21, 2015).
2. J. Tao *et al.*, Direct Imaging of Nanoscale Phase Separation in La_{0.55}Ca_{0.45}MnO₃: Relationship to Colossal Magnetoresistance. *Phys Rev Lett* **103**, (Aug 28, 2009).
3. M. E. Lines, A. M. Glass, *Principles and applications of ferroelectrics and related materials*. Oxford classic texts in the physical sciences (Clarendon Press; Oxford University Press, Oxford New York, 2001), pp. xiii, 680 p.
4. K. A. Rabe, M. Dawber, C. Lichtensteiger, C. H. Ahn, J. M. Triscone, Modern physics of ferroelectrics: Essential background. *Top Appl Phys* **105**, 1 (2007).
5. S. Muhlbauer *et al.*, Skyrmion Lattice in a Chiral Magnet. *Science* **323**, 915 (Feb 13, 2009).
6. M. R. Norman, The Challenge of Unconventional Superconductivity. *Science* **332**, 196 (Apr 8, 2011).
7. N. Balke *et al.*, Enhanced electric conductivity at ferroelectric vortex cores in BiFeO₃. *Nat Phys* **8**, 81 (Jan, 2012).
8. J. Guyonnet, I. Gaponenko, S. Gariglio, P. Paruch, Conduction at Domain Walls in Insulating Pb(Zr_{0.2}Ti_{0.8})O₃ Thin Films. *Adv Mater* **23**, 5377 (Dec 1, 2011).
9. S. E. Park, T. R. Shrout, Ultrahigh strain and piezoelectric behavior in relaxor based ferroelectric single crystals. *J Appl Phys* **82**, 1804 (Aug 15, 1997).
10. R. E. Cohen, Materials science - Relaxors go critical. *Nature* **441**, 941 (Jun 22, 2006).
11. H. Takenaka, I. Grinberg, S. Liu, A. M. Rappe, Slush-like polar structures in single-crystal relaxors. *Nature* **546**, 391 (Jun 15, 2017).
12. B. Gludovatz *et al.*, A fracture-resistant high-entropy alloy for cryogenic applications. *Science* **345**, 1153 (Sep 5, 2014).
13. D. B. Miracle, O. N. Senkov, A critical review of high entropy alloys and related concepts. *Acta Mater* **122**, 448 (Jan 1, 2017).
14. B. Cantor, I. T. H. Chang, P. Knight, A. J. B. Vincent, Microstructural development in equiatomic multicomponent alloys. *Mat Sci Eng a-Struct* **375**, 213 (Jul 15, 2004).

15. J. W. Yeh *et al.*, Formation of simple crystal structures in Cu-Co-Ni-Cr-Al-Fe-Ti-V alloys with multiprincipal metallic elements. *Metall Mater Trans A* **35A**, 2533 (Aug, 2004).
16. E. J. Pickering, N. G. Jones, High-entropy alloys: a critical assessment of their founding principles and future prospects. *Int Mater Rev* **61**, 183 (2016).
17. K. Aizu, Possible Species of Ferromagnetic, Ferroelectric, and Ferroelastic Crystals. *Phys Rev B* **2**, 754 (1970).
18. A. K. Tagantsev, L. E. Cross, J. Fousek, Domains in Ferroic Crystals and Thin Films. *Domains in Ferroic Crystals and Thin Films*, 1 (2010).
19. K. Aizu, Possible Species of Ferroelastic Crystals and of Simultaneously Ferroelectric and Ferroelastic Crystals. *J Phys Soc Jpn* **27**, 387 (1969).
20. D. G. Schlom, L. Q. Chen, X. Q. Pan, A. Schmehl, M. A. Zurbuchen, A thin film approach to engineering functionality into oxides. *J Am Ceram Soc* **91**, 2429 (Aug, 2008).
21. L. W. Martin, D. G. Schlom, Advanced synthesis techniques and routes to new single-phase multiferroics. *Curr Opin Solid St M* **16**, 199 (Oct, 2012).
22. V. M. Goldschmidt, The laws of crystal chemistry. *Naturwissenschaften* **14**, 477 (1926).
23. N. A. Benedek, C. J. Fennie, Why Are There So Few Perovskite Ferroelectrics? *J Phys Chem C* **117**, 13339 (Jul 4, 2013).
24. R. E. Cohen, Origin of Ferroelectricity in Perovskite Oxides. *Nature* **358**, 136 (Jul 9, 1992).
25. A. Vonhippel, R. G. Breckenridge, F. G. Chesley, L. Tisza, High Dielectric Constant Ceramics. *Ind Eng Chem* **38**, 1097 (1946).
26. G. H. Kwei, A. C. Lawson, S. J. L. Billinge, S. W. Cheong, Structures of the Ferroelectric Phases of Barium-Titanate. *Journal of Physical Chemistry* **97**, 2368 (Mar 11, 1993).
27. S. Wada *et al.*, Domain wall engineering in lead-free piezoelectric crystals. *Ferroelectrics* **355**, 37 (2007).
28. J. Sapriel, Domain-Wall Orientations in Ferroelastics. *Phys Rev B* **12**, 5128 (1975).
29. A. A. Bokov, Z. G. Ye, Recent progress in relaxor ferroelectrics with perovskite structure. *J Mater Sci* **41**, 31 (Jan, 2006).

30. S. W. Choi, T. R. Shrout, S. J. Jang, A. S. Bhalla, Dielectric and Pyroelectric Properties in the $\text{Pb}(\text{Mg}_{1/3}\text{Nb}_{2/3})\text{O}_3\text{-PbTiO}_3$ System. *Ferroelectrics* **100**, 29 (1989).
31. B. Noheda, D. E. Cox, G. Shirane, J. Gao, Z. G. Ye, Phase diagram of the ferroelectric relaxor $(1-x)\text{PbMg}_{1/3}\text{Nb}_{2/3}\text{O}_3\text{-xPbTiO}_3$. *Phys Rev B* **66**, (Aug 1, 2002).
32. D. La-Orautapong *et al.*, Phase diagram of the relaxor ferroelectric $(1-x)\text{Pb}(\text{Zn}_{1/3}\text{Nb}_{2/3})\text{O}_3\text{-xPbTiO}_3$. *Phys Rev B* **65**, (Apr 1, 2002).
33. B. Noheda *et al.*, Electric-field-induced phase transitions in rhombohedral $\text{Pb}(\text{Zn}_{1/3}\text{Nb}_{2/3})(1-x)\text{Ti}_x\text{O}_3$. *Phys Rev B* **65**, (Jun 1, 2002).
34. S. E. Park, T. R. Shrout, Relaxor based ferroelectric single crystals for electro-mechanical actuators. *Mater Res Innov* **1**, 20 (Jun, 1997).
35. G. Y. Xu, Z. Zhong, H. Hiraka, G. Shirane, Three-dimensional mapping of diffuse scattering in $\text{Pb}(\text{Zn}_{1/3}\text{Nb}_{2/3})\text{O}_3\text{-xPbTiO}_3$. *Phys Rev B* **70**, (Nov, 2004).
36. N. Liu, R. Dittmer, R. W. Stark, C. Dietz, Visualization of polar nanoregions in lead-free relaxors via piezoresponse force microscopy in torsional dual AC resonance tracking mode. *Nanoscale* **7**, 11787 (2015).
37. A. Bosak, D. Chernyshov, S. Vakhruhev, M. Krisch, Diffuse scattering in relaxor ferroelectrics: true three-dimensional mapping, experimental artefacts and modelling. *Acta Crystallogr A* **68**, 117 (Jan, 2012).
38. J. Hlinka, DO WE NEED THE ETHER OF POLAR NANOREGIONS? *Journal of Advanced Dielectrics* **02**, 1241006 (2012/04/01, 2012).
39. R. Bertram, G. Reck, R. Uecker, Growth and correlation between composition and structure of $(1-x)\text{Pb}(\text{Zn}_{1/3}\text{Nb}_{2/3})\text{O}_3\text{-xPbTiO}_3$ crystals near the morphotropic phase boundary. *J Cryst Growth* **253**, 212 (Jun, 2003).
40. A. E. Renault, H. Dammak, G. Calvarin, M. P. Thi, P. Gaucher, Domain structures in monoclinic $\text{Pb}[(\text{Zn}_{1/3}\text{Nb}_{2/3})(0.91)\text{Ti}-0.09]\text{O}_3$ poled single crystals. *Jpn J Appl Phys I* **41**, 3846 (Jun, 2002).
41. J. S. Forrester, E. H. Kisi, Monoclinic PZN-8%PT $[\text{Pb}(\text{Zn}_{0.3066}\text{Nb}_{0.6133}\text{Ti}_{0.08})\text{O}_3]$ at 4 K. *Acta Crystallogr C* **63**, I115 (Dec, 2007).
42. J. M. Kiat *et al.*, Monoclinic structure of unpoled morphotropic high piezoelectric PMN-PT and PZN-PT compounds. *Phys Rev B* **65**, (Feb 1, 2002).

43. E. H. Kisi, J. S. Forrester, The phase transition sequence in the relaxor ferroelectric PZN-8% PT. *J Phys-Condens Mat* **20**, (Apr 23, 2008).
44. K. Ohwada, K. Hirota, P. W. Rehrig, Y. Fujii, G. Shirane, Neutron diffraction study of field-cooling effects on the relaxor ferroelectric $\text{Pb}[(\text{Zn}_{1/3}\text{Nb}_{2/3})_{0.92}\text{Ti}_{0.08}]\text{O}_3$. *Phys Rev B* **67**, (Mar 1, 2003).
45. K. Ohwada *et al.*, Neutron diffraction study of the irreversible R-M-A-M-C phase transition in single crystal $\text{Pb}[(\text{Zn}_{1/3}\text{Nb}_{2/3})_{1-x}\text{Ti}_x]\text{O}_3$. *J Phys Soc Jpn* **70**, 2778 (Sep, 2001).
46. T. Asada, T. Shibata, Y. Koyama, Ferroelectric domain structures near the MPB in $(1-x)\text{Pb}(\text{Zn}_{1/3}\text{Nb}_{2/3})\text{O}_3$ - $x\text{PbTiO}_3$. *Ferroelectrics* **347**, 17 (2007).
47. K. H. Kim, D. A. Payne, J. M. Zuo, Determination of 60 degrees polarization nanodomains in a relaxor-based ferroelectric single crystal. *Appl Phys Lett* **107**, 162902 (Oct 19, 2015).
48. H. X. Fu, R. E. Cohen, Polarization rotation mechanism for ultrahigh electromechanical response in single-crystal piezoelectrics. *Nature* **403**, 281 (Jan 20, 2000).
49. B. Noheda *et al.*, Polarization rotation via a monoclinic phase in the piezoelectric 92% $\text{PbZn}_{1/3}\text{Nb}_{2/3}\text{O}_3$ -8% PbTiO_3 . *Phys Rev Lett* **86**, 3891 (Apr 23, 2001).
50. K. H. Kim, D. A. Payne, J. M. Zuo, Symmetry of piezoelectric $(1-x)\text{Pb}(\text{Mg}_{1/3}\text{Nb}_{2/3})\text{O}_3$ - $x\text{PbTiO}_3$ ($x=0.31$) single crystal at different length scales in the morphotropic phase boundary region. *Phys Rev B* **86**, 184113 (Nov 29, 2012).
51. K. H. Kim, D. A. Payne, J. M. Zuo, Determination of fluctuations in local symmetry and measurement by convergent beam electron diffraction: applications to a relaxor-based ferroelectric crystal after thermal annealing. *J Appl Crystallogr* **46**, 1331 (Oct, 2013).
52. A. A. Bokov, Z. G. Ye, Domain structure in the monoclinic Pm phase of $\text{Pb}(\text{Mg}_{1/3}\text{Nb}_{2/3})\text{O}_3$ - PbTiO_3 single crystals. *J Appl Phys* **95**, 6347 (Jun 1, 2004).
53. J. W. Yeh *et al.*, Nanostructured high-entropy alloys with multiple principal elements: Novel alloy design concepts and outcomes. *Adv Eng Mater* **6**, 299 (May, 2004).
54. H. P. Chou, Y. S. Chang, S. K. Chen, J. W. Yeh, Microstructure, thermophysical and electrical properties in $\text{Al}_x\text{CoCrFeNi}$ ($0 \leq x \leq 2$) high-entropy alloys. *Mater Sci Eng B-Adv* **163**, 184 (Jul 25, 2009).

55. Y. F. Kao, T. J. Chen, S. K. Chen, J. W. Yeh, Microstructure and mechanical property of as-cast, -homogenized, and -deformed Al_xCoCrFeNi (0 ≤ x ≤ 2) high-entropy alloys. *J Alloy Compd* **488**, 57 (Nov 20, 2009).
56. C. Li, J. C. Li, M. Zhao, Q. Jiang, Effect of aluminum contents on microstructure and properties of Al_xCoCrFeNi alloys. *J Alloy Compd* **504**, S515 (Aug, 2010).
57. T. T. Shun, Y. C. Du, Microstructure and tensile behaviors of FCC Al_{0.3}CoCrFeNi high entropy alloy. *J Alloy Compd* **479**, 157 (Jun 24, 2009).
58. W. R. Wang *et al.*, Effects of Al addition on the microstructure and mechanical property of Al_xCoCrFeNi high-entropy alloys. *Intermetallics* **26**, 44 (Jul, 2012).
59. T. F. Yang *et al.*, Effects of AL addition on microstructure and mechanical properties of Al_xCoCrFeNi High-entropy alloy. *Mat Sci Eng a-Struct* **648**, 15 (Nov 11, 2015).
60. B. Gludovatz *et al.*, Exceptional damage-tolerance of a medium-entropy alloy CrCoNi at cryogenic temperatures. *Nat Commun* **7**, (Feb, 2016).
61. T. F. Yang *et al.*, Effects of temperature on the irradiation responses of Al_{0.1}CoCrFeNi high entropy alloy. *Scripta Mater* **144**, 31 (Feb, 2018).
62. T. F. Yang *et al.*, Precipitation behavior of Al_xCoCrFeNi high entropy alloys under ion irradiation. *Sci Rep-Uk* **6**, (Aug 26, 2016).
63. J. W. Yeh, Recent progress in high-entropy alloys. *Ann Chim-Sci Mat* **31**, 633 (Nov-Dec, 2006).
64. Q. F. He, Y. Yang, On Lattice Distortion in High Entropy Alloys. *Front Mater* **5**, (Jul 24, 2018).
65. M. H. Tsai, J. W. Yeh, High-Entropy Alloys: A Critical Review. *Mater Res Lett* **2**, 107 (2014).
66. Y. Zhang *et al.*, Microstructures and properties of high-entropy alloys. *Prog Mater Sci* **61**, 1 (Apr, 2014).
67. J. W. Yeh, Physical Metallurgy of High-Entropy Alloys. *Jom-Us* **67**, 2254 (Oct, 2015).
68. J. W. Yeh, S. Y. Chang, Y. D. Hong, S. K. Chen, S. J. Lin, Anomalous decrease in X-ray diffraction intensities of Cu-Ni-Al-Co-Cr-Fe-Si alloy systems with multi-principal elements. *Mater Chem Phys* **103**, 41 (May 15, 2007).
69. H. Y. Diao, L. J. Santodonato, Z. Tang, T. Egami, P. K. Liaw, Local Structures of High-Entropy Alloys (HEAs) on Atomic Scales: An Overview. *Jom-Us* **67**, 2321 (Oct, 2015).

70. W. Guo *et al.*, Local Atomic Structure of a High-Entropy Alloy: An X-Ray and Neutron Scattering Study. *Metall Mater Trans A* **44A**, 1994 (May, 2013).
71. M. S. Lucas *et al.*, Absence of long-range chemical ordering in equimolar FeCoCrNi. *Appl Phys Lett* **100**, (Jun 18, 2012).
72. L. R. Owen *et al.*, An assessment of the lattice strain in the CrMnFeCoNi high-entropy alloy. *Acta Mater* **122**, 11 (Jan 1, 2017).
73. G. V. Y. Tong, T. Yang, K. Jin, C. Lu, H. Bei, J. Y. P. Ko, D. C. Pagan, R. Huang, Y. Zhang, L. Wang, and F. X. Zhang, Probing local lattice distortion in medium- and high-entropy alloys. *arXiv:1707.07745*, (2017).
74. F. X. Zhang *et al.*, Local Structure and Short-Range Order in a NiCoCr Solid Solution Alloy. *Phys Rev Lett* **118**, (May 19, 2017).

CHAPTER 2

SCANNING CONVERGENT BEAM ELECTRON DIFFRACTION

This chapter discusses about the experimental acquisition and data analysis methods for the scanning convergent beam electron diffraction (SCBED) technique. We include details about the scanning diffraction system, TEM operation procedures, and the symmetry quantification algorithm. The applications of SCBED and the symmetry quantification algorithm to probe local polarization domains and symmetry breaking in ferroelectric perovskites and multi-principal-element alloys are reported in Chapters 3-5.

2.1 Transmission electron diffraction

In a transmission electron microscope (TEM), the structure of materials can be determined by utilizing the electrons that traveled through a specimen. The electrons interact with the nuclei and the electron cloud in a specimen, and are scattered multiple times due to the strong Coulomb forces. As a result of destructive and constructive interference of scattered electron waves, diffraction may occur because the wavelength of high energy electrons (e.g., 0.0251 Å for 200keV electrons) is much smaller than the crystal lattice parameters. Electron diffraction in a TEM can be obtained from a small region/volume of the specimen (e.g., ranging from a few nm³ to μm³), which is useful for the determination of crystal orientation, local lattice parameter or strain, phase identification, and crystal defect analysis.

2.2 Illumination semi-convergence angle α

The commonly recorded electron diffraction patterns in TEMs are spot patterns using a beam that is approximately parallel. Convergent beam electron diffraction (CBED), on the other hand, is obtained by focusing the electron beam into a probe onto the sample. Because of the convergent beam, the transmitted and diffracted spots in a diffraction pattern broaden into disks. The illumination convergence angle, or the size of the disk, is an important parameter in CBED, because it determines the range of excitation errors (S_g) for each reflection. Along a zone axis, the ideal CBED disk size is twice the Bragg angle ($2\theta_B$) of the lowest order zero-order Laue zone (ZOLZ) reflection, in order to fill the diffraction space as much as possible without disk overlap, as shown in Fig. 2.1 (1).

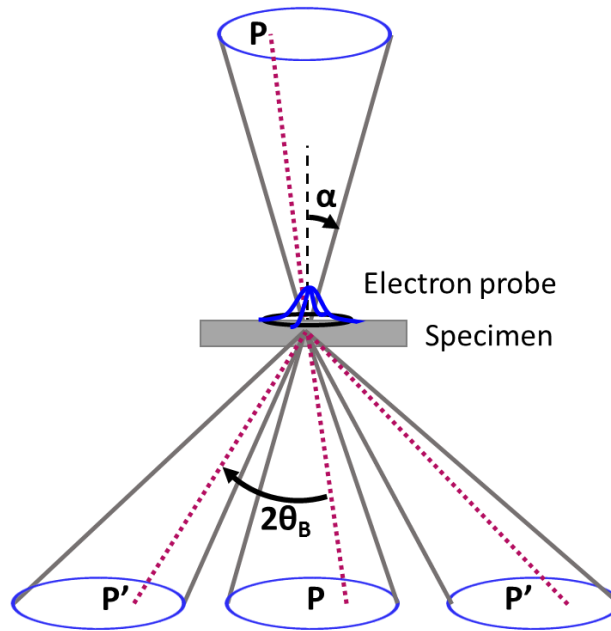


Figure 2.1. Schematic ray diagram for convergent beam electron diffraction. Source point P gives rise to conjugate (diffracted) points P' . Symbols α and θ_B denote semi-convergence angle and Bragg angle, respectively.

The size of the disk is two times the semi-convergence angle α , which is usually defined by the condenser aperture in a TEM. The use of the condenser minilens (CM), placed immediately above the objective prefield lens as shown in Fig. 2.2, allows additional change in convergence angles. The “alpha-selectors knob” in JEOL TEMs is used to adjust the CM lens strength (2). The NBD- and CBD-modes are under similar C2-CM configurations for JEOL microscopes installed in the Center for Microanalysis of Materials (CMM) in the Materials Research Laboratory (MRL). However, CBD-mode offers 9 selections of α , while NBD-mode offered 5.

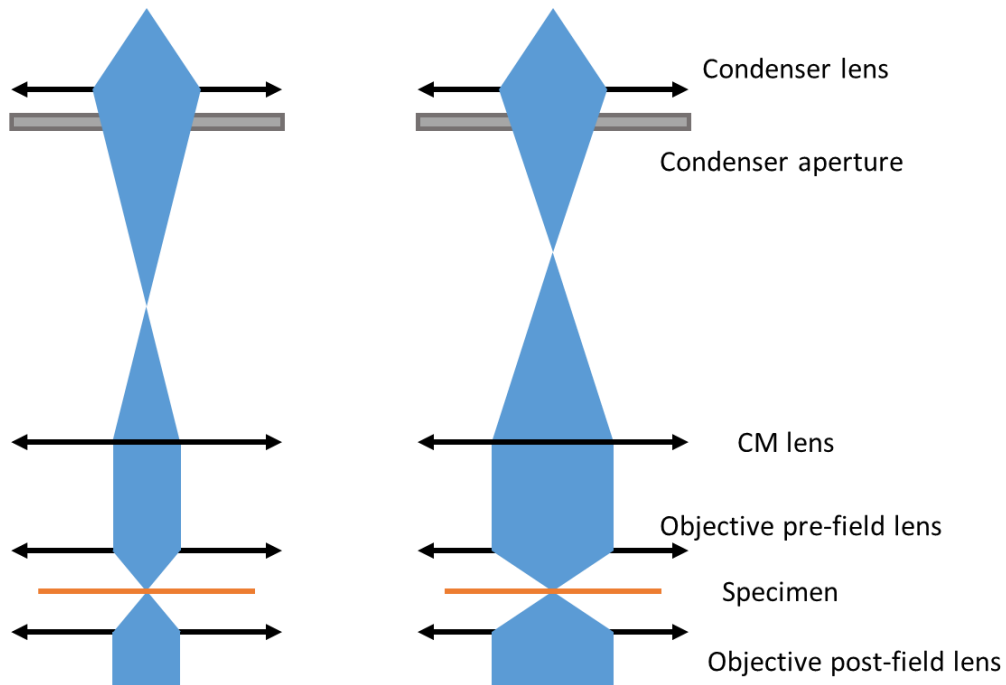


Figure 2.2. Schematic ray diagram for a two condenser lenses system. Focused electron probes with a small and large convergence angle obtained using different settings for the CL and CM lenses (3).

The Thermo Fisher Themis Z STEM installed recently in the CMM, MRL at University of Illinois has the three condenser lenses setup. The C1-C2 zoom controls the spot size, and the C2-C3 zoom controls the beam convergence angle (θ). Using the “MF-Y knob” under “probe mode”, it is possible to adjust the convergence angle continuously, by tuning the ratio of C2 and C3 lenses excitations, i.e., changing the position of the intermediate image between C2 and C3 lenses as shown in Fig. 2.3. Specifically, the switching from “nanoprobe” to “microprobe” mode is associated with the switching on of the condenser minilens, where the beam convergence angles are five times smaller when the CM is switched on. The SCBED experiments can be performed in microprobe-STEM mode, under spectrum-imaging tab. In practice, while varying the convergence angle with MF-Y knob, it is important to check in the imaging mode whether the probe is well-focused or not, since no TEMs are truly hysteresis-free (yet). The probe can be re-focused by changing the objective pre-field excitations, or “intensity list”. However, note that by changing the objective excitations would lead to slight changes in the image magnification, which requires further calibration for careful experiments.

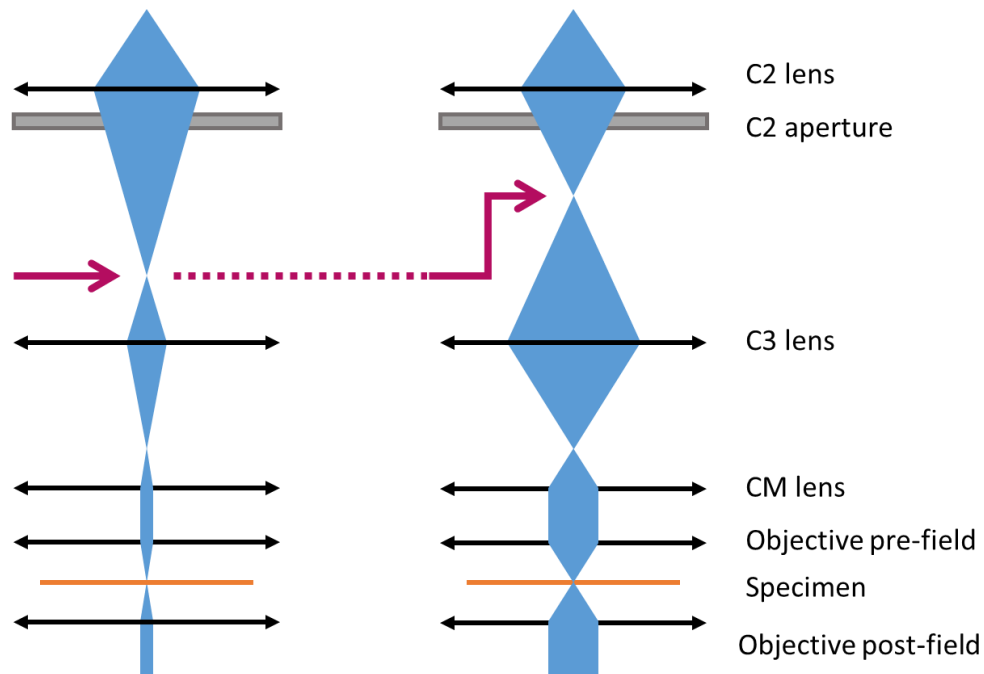


Figure 2.3. Schematic ray diagram for a three condenser lenses system. Focused electron probes with a small and large convergence angle can be varied continuously by changing the position of the intermediate image between C2 and C3 lenses, as indicated by the red arrows.

2.3 Probe size

A small electron probe is essential for studying local structures such as symmetry, strain, and defect characterization. The small probe it allows the diffraction patterns to be taken from local regions in the sample. In scanning CBED or scanning transmission electron microscopy (STEM), the probe size often defines the spatial resolution in the obtained images. To form a focused probe, the crossover from the last condenser lens is imaged by the objective prefield lens onto the specimen, as shown in Figs. 2.2 and 2.3. Under “incoherent” conditions (i.e., lateral coherence $2L$ is less than condenser aperture diameter $2R$), the total probe diameter d_0 is a result of a series of broadening effects from spherical aberration in the probe forming lens d_{sa} , diffraction by aperture

d_d , chromatic aberration of probe forming lens d_c , and focusing error d_f , which can be approximately expressed as:

$$d_o^2 = d_s^2 + d_d^2 + d_{sa}^2 + d_c^2 + d_f^2 = \left(\frac{0.6\lambda}{\theta_c}\right)^2 + (0.5C_s\theta_c^3)^2 + \left(\frac{\Delta E_0}{E_0}C_c\theta_c\right)^2 + (2\theta_c\Delta f)^2 \quad (2.1)$$

, where λ is the electron wave length, θ_c is the beam convergence angle, C_s is the spherical aberration coefficient, C_c is the chromatic aberration coefficient, and Δf is the defocus value (3).

The size of electron probes in a TEM with a LaB₆ thermionic source is largely determined by the size of the demagnified source image. Experimentally the probe size can be measured by the full-width at half-maximum (FWHM) of the electron intensity in the Gaussian distribution. With the JEOL 2100 LaB₆ TEM, the probe can vary from 50nm, 30nm, 20nm at FWHM in TEM-mode, and 10nm, 5nm, 2nm at FWHM in CBD-mode. With the JEOL 2010F or 2200FS having a Schottky field-emission source, the probe can easily be tuned from 5nm to 1nm at FWHM. The advantages of the 2010F and 2200FS microscopes at MRL are not only the smaller probes due to the FEG, but also the energy-filtering capability (GIF and Omega filters, respectively). Energy-filtering is extremely crucial for CBED experiments, especially for thick specimen where the inelastic scattered electron would significantly blur out the fine features within the disks (predominantly plasmon-loss).

While FEG offers a smaller probe size which gives a better spatial resolution for SCBED experiments, LaB₆ works better for beam-sensitive materials due to lower brightness. For example, low-dose SEND has been demonstrated to identify dendritic phases in LiCoO₂ (5). The experiments were done on JEOL 2100 LaB₆ TEM with a small condenser aperture of 20 μ m, under NBD-mode $\alpha 1$, spot 3nm, which gives a probe size of ~ 2.6 nm in FWHM.

2.4 Beam scanning system

Electron nanodiffraction was first demonstrated by Prof. John M. Cowley using STEM and a TV camera for recording diffraction patterns (6). At University of Illinois, Dr. Jing Tao and Prof. Jian-Min Zuo developed the technique of “scanning electron nanodiffraction (SEND)” (7) for imaging nanoscale phase separation of charge ordering phases in $\text{La}_{0.55}\text{Ca}_{0.45}\text{MnO}_3$ (8). The principle of scanning electron diffraction is based on controlling (1) scanning coils which deflects/shifts the electron beam, and (2) pixelated detectors such as CCD/K2 camera for automated acquisition, where a diffraction pattern is recorded at every probe position in a defined region of interest (see Fig. 2.4). A similar technique, scanning precession electron diffraction (SPED) (9, 10), was implemented by NanoMEGAS (11) using an external scanning system, which the electron beam is rocked at each probe position for reducing dynamical effects. The NanoMEGAS system works by using an additional hardware to control the scanning deflectors (beam shift/tilt, and post objective lens de-scan) with electrical signal, while capturing the diffraction patterns on fluorescent screen with a camera for fast acquisition. With the development of fast cameras which can easily acquire more than 1000 frames per second (e.g. K2 (12), EMPAD (13), medipix3 (14), just to name a few), the development of scanning diffraction is getting attention, which serves as a technique providing structural information complementary to STEM-HAADF, EDS, or EELS spectrum imaging (15).

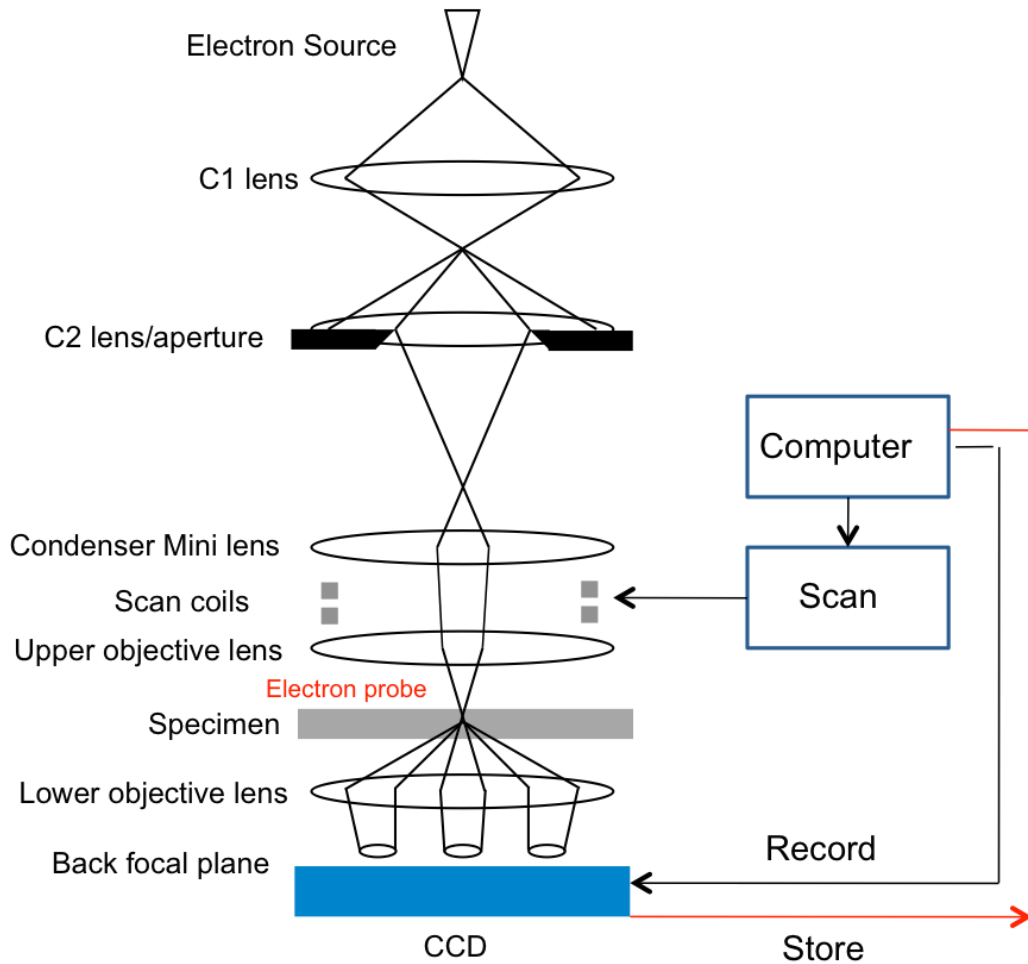


Figure 2.4. Schematic illustration of the SEND system.(16)

The DigitalMicrograph[®] script, *Scanning_ED*, developed at the University of Illinois is used to drive the beam scanning and image recording (17). DM is a common software used for acquisition, process, and analysis for TEM images or data. The software is programmable, known as DM script, which can be used to customize tasks. For example, different parts of TEM can be controlled using DM script, including the beam or image shift/tilt deflectors and the CCD camera. Useful database of DM script can be found online, see <http://www.dmscripting.com/index.html> or <https://www.felmi-zfe.at/dm-script/dm-script-database/>. The script *Scanning_ED* interfaces with

several main function that are used to control the microscope (*EMGetBeamShift*, *EMSetBeamShift*, and *SSCGainNormalizedBinnedAcquire*). The values set in functions *EMGetBeamShift* and *EMSetBeamShift* are digital numbers, and they are calibrated and converted into the values in terms of sample coordinates in nanometers. The calibration is done using a function built in the script, which the user would perform to establish a reliable current-to-nanometer conversion for each experiment. During acquisition, the script will shift the probe in a raster scan, from left to right and top to bottom. A parameter to rotate the raster scanning rectangle was also implemented, which is useful for aligning the scanning coordinates with the x- and y- axis of the region of interest (18).

To make the beam scan into large regions of interest and being able to handle a large dataset, we have implemented a thread-based acquisition. The *thread* object in DM allows the script to be run in ‘background’, not blocking user interaction, as well as the option to stop a long acquisition halfway. To enable SCBED acquisition in STEM mode, we have implemented the DM script using the DigiScan to drive the scanning coils. The main functions used in the STEM mode are *DSSetBeamPosition*, *DSCalcImageCoordFromDS*. The script has been tested on following models: JEOL 2100 LaB6, 2100F, 2010F, 2200FS, ARM 200F, and Thermo Fisher Themis Z. The DM script *Scanning_ED* used for acquiring scanning diffraction data is listed in Appendix A.

2.5 Operation procedures

The microscope alignments to consider when performing SCBED experiments are: (1) tilt-shift purity, (2) beam shift-induced diffraction shift, (3) diffraction focus, (4) probe focus. The tilt-shift purity is of prime importance since a CBED pattern is extremely sensitive to change in diffraction condition ($<0.012^\circ$ in crystal tils or lattice-rotation). Ideally, the beam is not tilted

during the beam scanning for SCBED. Not only does the tilt affect the orientation of the CBED pattern, it also affects the position of CBED pattern. Second, the diffraction pattern also shifts during beam scanning if the diffraction focus and shift alignments are non-ideal. The beam shift-induced diffraction shift alignment is crucial for measuring deflections due to the presence of electric/magnetic fields as well as for successful data processing. Third, incorrect diffraction focus will impose Fresnel fringes to disks in a CBED pattern, which will affect intensity analysis such as quantitative CBED refinements. Fourth, incorrect probe focus will give rise to a mixture of imaging plane information with the CBED pattern, which will complicate the CBED analysis. The full alignment procedure is listed as following:

- 1) Switch to CBD mode and the desired alpha, spot size selection. Press “standard focus”.
- 2) With the largest condenser aperture inserted, perform the standard TEM alignments including gun tilt/shift, bright tilt, and pivot point. It is not uncommon that the alignments in CBD modes are far from ideal condition. One practical trick is to align the stigmators from top to bottom, while checking their HEX values. For example, the optimum HEX values for “Beam shift” on JEOL microscopes are around 8000/8000, so the alternative deflector for shifting the beam would be “spot align”, which the latter is associated with “bright tilt”.
- 3) Switch to the desired condenser aperture. The condenser aperture can be aligned by wobbling back and forth the brightness knob until the circles on the phosphorous screen are concentric.
- 4) Focus the beam in vacuum, and switch to diffraction mode. Align the diffraction focus (IL1) until the edge of the disk is sharp and its line profile has an inflection point near the middle, as shown in Fig. 2.5. In some cases, one would observe the irregular shape

on the disk edges, which results from imperfect circular machining of the condenser diaphragm. This step is crucial for quantitative CBED analysis for measuring low-order structure factors (19).

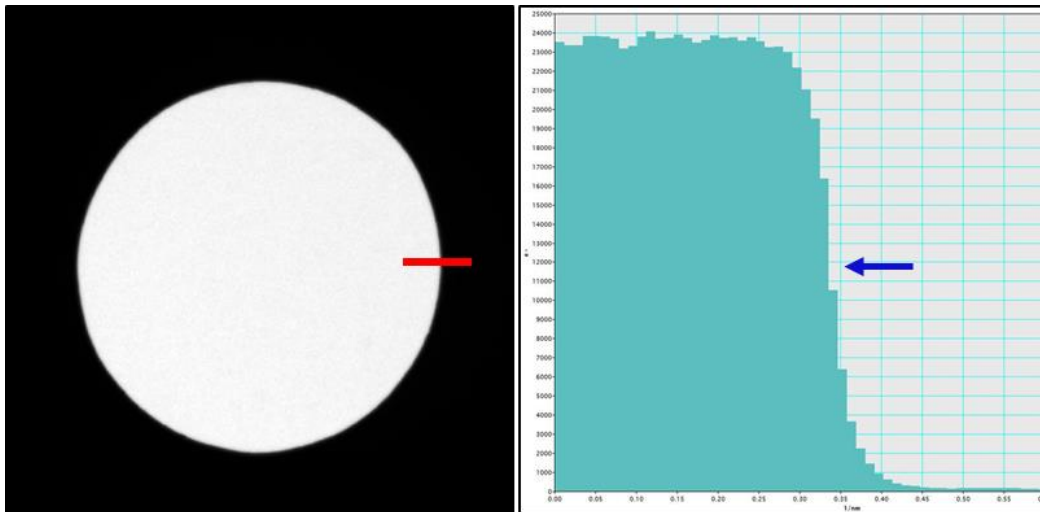


Figure 2.5. Image of the condenser aperture, or CBED disk in vacuum, with the right diffraction focus. The line profile shows an inflection point near the middle.

- 5) Check the alignments of “shift” and “shift x/shift y”. Align the diffracted disk until the movement is minimized. This step reduces the shift in diffraction pattern during beam scanning.
- 6) Check the alignments of “tilt” and “tilt x /tilt y”. The pivot point alignment is subject to the change in bright tilt and focus, hence iterations in this step is needed. For JEOL 2200FS in CBD-mode, the pivot-point may be way off and out of the deflector range. This may be attributed to the different objective lens setting from the “standard focus”. A trick to get around this problem is to strongly defocus/over-focus the objective lens to about 3.28V, which is close to the factory setting of the objective lens. However, note

that by doing so would require an iterative alignment of the stigmators above, such as “CL stigmator” or “bright tilt”.

- 7) Bring the specimen to the correct z-height. This can be checked by either the “image wobbler”, or more precisely, the image of a focused probe on specimen. To check if the specimen is not at the correct z-height, we should expect a well-focused round spot in imaging mode, otherwise there will be “diffracted spots/streaks” in the image mode, as shown in Fig. 2.6. If the CBED pattern is slightly defocused, the disks will contain image information, known as “shadow images”, which will complicate the CBED analysis.

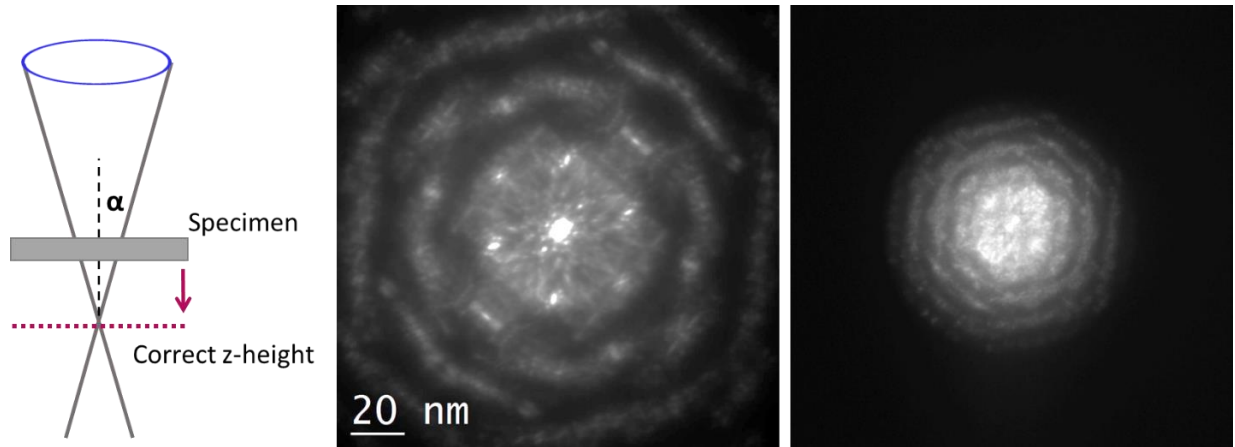


Figure 2.6. Real space images of a focused electron probe at the incorrect z-height on a Si [110] specimen with larger (left) and less (right) defocus. The defocused probe led to the mixture of diffraction information in the imaging plane, or vice versa.

- 8) Energy-filtering is strongly recommended for recording high quality CBED patterns, especially for thick specimens (see Fig. 2.7). A10eV energy selecting window is placed at the center of the zero-loss peak in the electron energy loss spectrum (EELS). For Omega filters on the JEOL 2200FS, two parameters are critical: isochromaticity and slit

position. For post column GIF, be sure to tune the low-order stigmatism (e.g. f_x , f_y , s_x , s_y) to minimize image distortions.

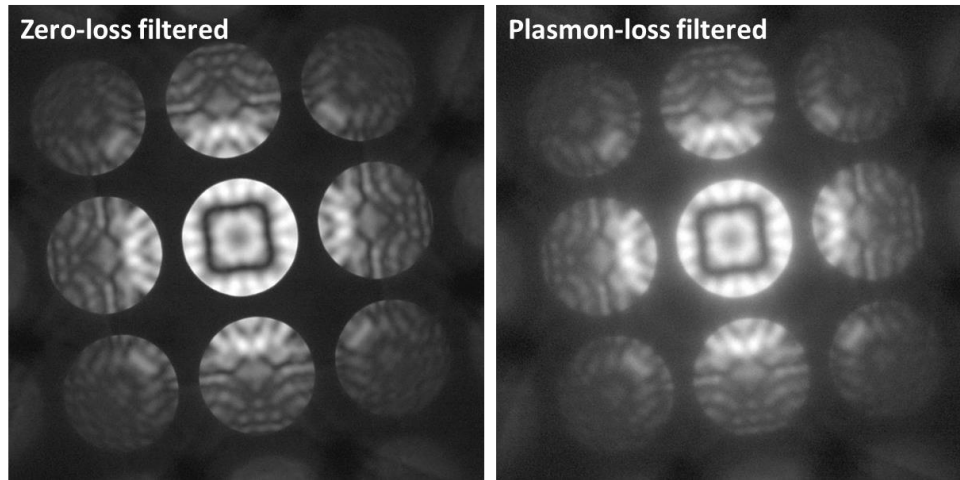


Figure 2.7. Energy-filtered CBED patterns of Al [001] using an in-column Omega filter with 10eV energy selecting window centered around zero-loss peak (left) and plasmon loss (right).

- 9) Perform the SEND calibration mentioned above. This step calibrated the DAC current into unit x- and y-vectors in nm.
- 10) Determine the scanning step size, offset angle, scanning area, and exposure time. In most cases, the step size is about the same order of magnitude as the probe size; the scanning area and exposure time is a trade-off between total acquisition time versus specimen stage stability/drift and CBED intensity/noise level.

The detailed procedures for performing SCBED experiments is described above. However, in some cases one would intentionally defocus the CBED pattern by either changing the z-height or the objective lens focus. This is referred as the large-angle CBED (LACBED) technique. The LACBED technique was shown to be useful for analyzing burgers vectors of dislocations, or

symmetry determination for large unit-cell crystals. Detailed description of the LACBED technique can be found in Refs. (20, 21).

2.6 Symmetry quantification

In real crystals, the local symmetry often breakdown depending on its boundary conditions. The symmetry breaking may be due to crystallographic defects, epitaxial strain, ferroelectric polarization, or magnetic symmetry. The symmetry recorded CBED pattern, to a column approximation, is averaged over the volume being illuminated by the electron probe, as shown in Fig. 2.6. When using SCBED for local symmetry determination, it is helpful to quantify the amount of symmetry breaking recorded in CBED patterns (22, 23). The symmetry quantification algorithm proposed by Dr. Kyou-Hyun Kim and Prof. Jian-Min Zuo (24) is based on the normalized cross correlation coefficient γ (25), which measures the similarities between two images/diffracted disks:

$$\gamma = \frac{\sum_{x,y}\{[I_A(x,y)-\bar{I}_A] \cdot [I_B(x,y)-\bar{I}_B]\}}{\sqrt{\{\sum_{x,y}[I_A(x,y)-\bar{I}_A]^2\} \cdot \{\sum_{x,y}[I_B(x,y)-\bar{I}_B]^2\}}} \quad (2.2)$$

, where \bar{I}_A and \bar{I}_B are the mean values of two diffracted disks that are being compared. From the equation, the correlation coefficient is close to 1 as the two images become identical.

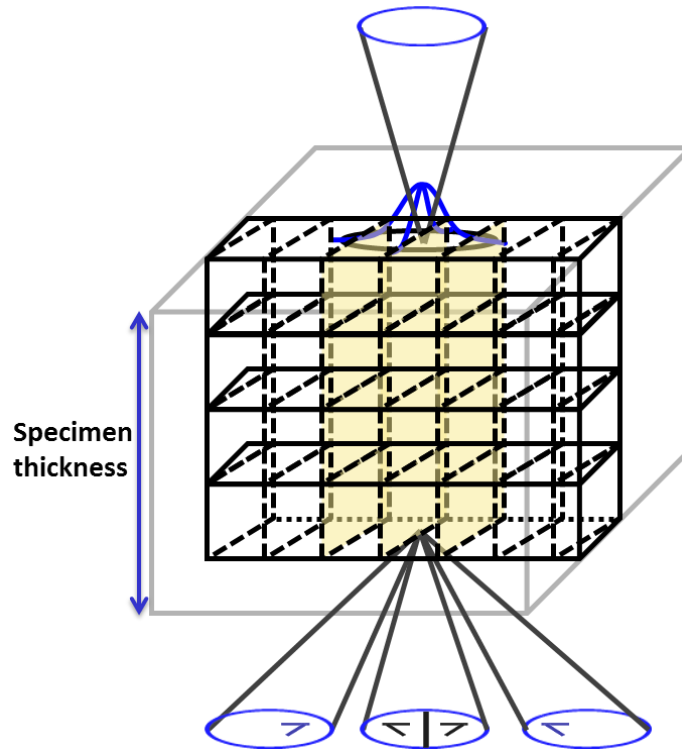


Figure 2.8. Schematic ray diagram for CBED pattern detecting symmetry in real crystals. For column approximation, the highlighted region indicates the volume being illuminated by the electron beam.

While the DM script implemented by Dr. Kyou-Hyun Kim works efficiently for quantifying a pair of disks in a CBED pattern, the algorithm itself has some drawbacks. First, it requires manual placing circular annotations onto the experimental CBED pattern, which introduces uncertainties to the pixel-to-pixel operation such as cross correlation. Second, in experimental CBED patterns, it is possible to have different cross correlation values γ_g for different pairs of reflections.

To further improve the robustness of symmetry quantification using SCBED, we have implemented a modified algorithm in DM script to quantify the CBED whole pattern. An array of circular annotations will be generated based on the two basis vectors. To provide one normalized cross-correlation value for each CBED pattern, our new algorithm weights each γ_g value with

respect to the disk intensities, namely $\gamma_{representative} = \frac{\sum_g I_g \gamma_g}{\sum_g I_g}$. For example, Fig. 2.5 shows the procedure for quantifying the symmetry of a Si [110] CBED pattern. Pairs of diffraction discs related by mirror are selected and marked by the orange circles from (A, A') to (G, G'). The diffraction discs on the mirror plane are marked by blue circles from m1 to m4. The table list out the γ values and the corresponding summed intensities, which gives the weighted cross-correlation value of this pattern $\gamma = 98.1\%$. The script also quantifies the symmetry in the bright-field, or the transmitted (000) disk. The DM script *QSymm* for symmetry quantification of CBED whole pattern is listed in Appendix A.

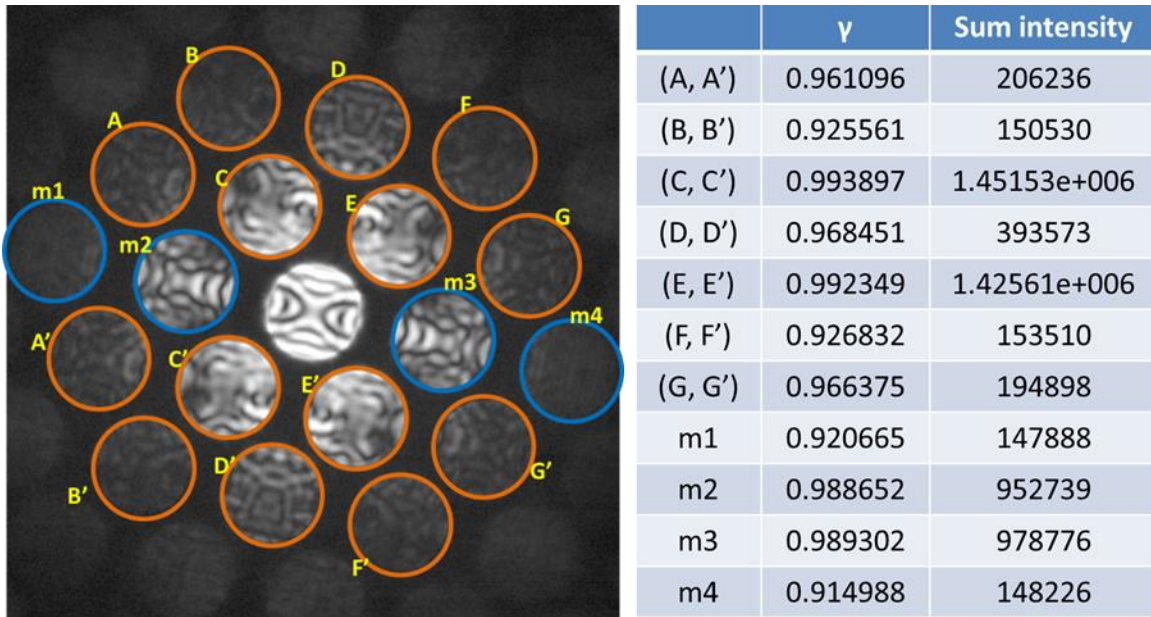


Figure 2.9. Procedure used for quantifying mirror symmetry of a Si [110] CBED pattern. Disks m1-m4 indicate the reflections on the mirror plane.

The procedures for symmetry quantification in the DigitalMicrograph[®] software using the DM script are listed as follows:

- 1) Open the results window and make sure it is visible. The cross correlation coefficients will be output into this panel.
- 2) Use the ROI tool to draw a rectangle. This limits the region for symmetry quantification, since the reflections outside the ZOLZ are usually weak.
- 3) Draw two line annotations on the CBED pattern. This defines its two basis vectors, \vec{g} and \vec{h} .
- 4) Use keyboard “0” and arrow keys for adjusting the center coordinate; “g”, “h”, and arrow keys for adjusting the two vectors.
- 5) Use keyboard “T” for switching on/off indexing for each reflection.
- 6) Use keyboard “r/R” for adjusting size of the circle. Use “-/+” for adjusting increments.
- 7) Press “m” for mirror symmetry quantification. Press “M” for changing the mirror plane. The mirror plane has the index (m, n), which came from $\vec{M} = m\vec{g} + n\vec{h}$.
- 8) Press “2”, “3”, “4”, “6” for quantifying 2-, 3-, 4-, 6-fold rotational symmetry.
- 9) Repeat steps 3-6 as if playing video games -- until you’ve got the highest score!
- 10) Save the templates for each symmetry element containing annotations. This is useful for quantifying the whole SCBED image stack.

A possible improvement of the current symmetry quantification algorithm is to include image processing procedures such as circular Hough transform (CHT) for disk detection. This will automate the step of finding disk positions in replacement of interactive trial and error using keyboard. However, implementing CHT in DM scripts would be more troublesome than in high level languages such as Matlab or Python.

We now give a few examples using the quantification algorithm for CBED patterns obtained from two sets of centrosymmetric and noncentrosymmetric crystals, Si, GaSb, SrTiO₃, and BaTiO₃. For clarity, regions outside the disks being quantified in the CBED pattern are being masked. For

example, the Si [110] possess $2mm$ symmetry, as shown in real space. The corresponding CBED pattern has two mirror planes of $\gamma_m=98.2\%$ and $\gamma_m=97.4\%$, and two-fold rotation symmetry of $\gamma_2=94.6\%$. On the other hand, noncentrosymmetric GaSb [110] possess m symmetry, with a mirror plane of $\gamma_m=97.4\%$. Similarly, SrTiO₃ is a centrosymmetric perovskite at room temperature, and possess $4mm$ symmetry along [001] incident direction, which the corresponding CBED pattern shows 4 mirror planes and four-fold rotation symmetry of $\gamma_4=97.4\%$. A polar perovskite, for example tetragonal BaTiO₃ shows a mirror plane of $\gamma_m=97.2\%$. As shown in Fig. 2.10, the polarization lies in the mirror plane of CBED patterns along certain orientations.

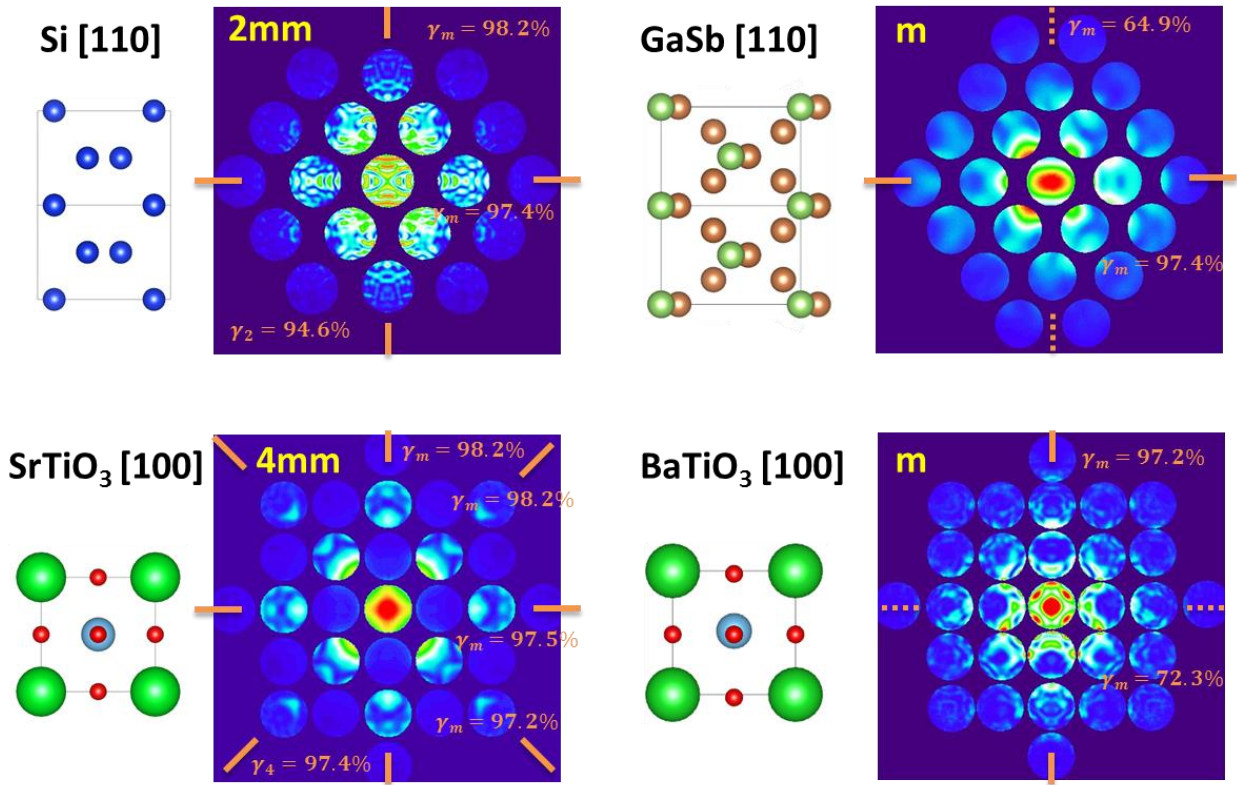


Figure 2.10. Symmetry quantification of CBED patterns obtained from centrosymmetric (left column) and noncentrosymmetric (right column) crystals.

2.7 CBED simulation

One of the benefits of SCBED and symmetry quantification is to obtain the experimental CBED pattern (best if energy-filtered) with the highest symmetry. This allows one to compare the best experimental CBED patterns with simulated patterns, and thus determine the structural parameters in the specimen such as thickness, orientation, polarization, or lattice parameters. The intensity versus S_g , or rocking curve information, recorded in CBED patterns can be used for quantitative structure factor refinement using pattern matching (26). There are three algorithms used in this thesis for dynamical diffraction simulation: Bloch-wave, multislice, and scattering-matrix method, and all of the simulation software packages were written by Prof. Jian-Min Zuo in Fortran and C (1, 27).

The Bloch wave method is often used for CBED simulation, which assumes the translational symmetry. Bloch-wave method is used for its accuracy, flexibility and the ability to calculate diffraction pattern in any orientation including high order Laue zone (HOLZ) reflections. The problem of electron diffraction is based on solving the time-independent Schrödinger equation by expanding the electron wave function inside the crystal using a set of Bloch waves. Important reviews of the Bloch wave method include (1, 28-30).

The multislice method was first proposed by Cowley and Moodie and others (31, 32), which has the advantage for calculating diffraction patterns or exit-wave functions from both crystals and non-periodic structures. The multislice method solves the time-dependent Schrödinger equation by forward-scattering approximation, with the specimen potential divided into a sequence of thin rectangular slices. The slice thickness must be thin enough to be a phase object, and be perpendicular to the optical axis of the electron microscope. Appendix B has listed the example

python script for 1) generating a BaTiO₃ supercell with random polarization clusters and 2) simulating SCBED of the supercell using multislice method (zmult.exe).

The scattering matrix method is used for simulating CBED patterns or images of crystals with defects (3, 33). The crystal potential with defects is constructed using the deformable ion approximation

$$U(\vec{r}) = \sum_g U_g \exp\left(-2\pi i \vec{g} \cdot \vec{R}(\vec{r})\right) \exp(-2\pi i \vec{g} \cdot \vec{r}) \quad (2.3)$$

where U_g is the Fourier coefficient of the perfect crystal potential and $\vec{R}(\vec{r})$ the atomic displacement. The constructed potential takes account of the modifications in the structure factors by strain, not composition. An example using the scattering-matrix method for simulating the HOLZ line splitting due to strain in GaAs/In_xGa_{1-x}As quantum wells can be found in Ref. (34). Appendix B contains the python script for 1) generating an fcc high entropy alloy supercell being divided into small blocks, each block having displacements follows the Gaussian distribution with specified mean and standard deviation of displacements; 2) simulating SCBED of the supercell using scattering-matrix method (blochz.exe and scbed.exe); and 3) output a binary file which can be imported into DigitalMicrograph[®] as an image stack for SCBED analysis.

2.8 References

1. J. C. H. Spence, J. M. Zuo, *Electron microdiffraction*. (Plenum Press, 1992).
2. JEOL.
3. J. M. Zuo, J. C. H. Spence, *Advanced Transmission Electron Microscopy*. Imaging and Diffraction in Nanoscience (New York: Springer, ed. 1, 2017), pp. XXVI, 729.
4. T. F. T. Z.
5. H. G. Zhang *et al.*, Electroplating lithium transition metal oxides. *Sci Adv* **3**, (May, 2017).
6. J. M. Cowley, Electron nanodiffraction. *Microsc Res Techniq* **46**, 75 (Jul 15, 1999).
7. J. M. Zuo, J. Tao, in *Scanning Transmission Electron Microscopy: Imaging and Analysis*, S. J. Pennycook, P. D. Nellist, Eds. (Springer New York, New York, NY, 2011), pp. 393-427.
8. J. Tao *et al.*, Direct Imaging of Nanoscale Phase Separation in La_{0.55}Ca_{0.45}MnO₃: Relationship to Colossal Magnetoresistance. *Phys Rev Lett* **103**, (Aug 28, 2009).
9. R. Vincent, P. A. Midgley, Double Conical Beam-Rocking System for Measurement of Integrated Electron-Diffraction Intensities. *Ultramicroscopy* **53**, 271 (Mar, 1994).
10. J. S. Barnard, D. N. Johnstone, P. A. Midgley, High-resolution scanning precession electron diffraction: Alignment and spatial resolution. *Ultramicroscopy* **174**, 79 (Mar, 2017).
11. NanoMEGAS.
12. Gatan.
13. M. W. Tate *et al.*, High Dynamic Range Pixel Array Detector for Scanning Transmission Electron Microscopy. *Microscopy and Microanalysis* **22**, 237 (Feb, 2016).
14. M. Krajnak, D. McGrouther, D. Maneuski, V. O'Shea, S. McVitie, Pixelated detectors and improved efficiency for magnetic imaging in STEM differential phase contrast. *Ultramicroscopy* **165**, 42 (Jun, 2016).
15. J.-M. Zuo, Y.-T. Shao, Scanning Convergent Beam Electron Diffraction (CBED), the Essential Questions of Why, What and How? *Microscopy and Microanalysis* **24**, 172 (2018).
16. Y. Meng, J.-M. Zuo, Three-dimensional nanostructure determination from a large diffraction data set recorded using scanning electron nanodiffraction. *IUCrJ* **3**, (2016).
17. K.-H. Kim, Dissertations & Theses, University of Illinois at Urbana-Champaign (2013).
18. Y. Meng, Dissertations & Theses, University of Illinois at Urbana-Champaign (2016).
19. P. N. H. Nakashima, A. W. S. Johnson, Measuring the PSF from aperture images of arbitrary shape - an algorithm. *Ultramicroscopy* **94**, 135 (Feb-Mar, 2003).
20. M. Tanaka, R. Saito, K. Ueno, Y. Harada, Large-Angle Convergent-Beam Electron-Diffraction. *J Electron Microsc* **29**, 408 (1980).
21. J. A. Eades, Zone-Axis Diffraction Patterns by the Tanaka Method. *J Electron Micr Tech* **1**, 279 (1984).
22. G. B. Hu, L. M. Peng, Q. F. Yu, H. Q. Lu, Automated identification of symmetry in CBED patterns: a genetic approach. *Ultramicroscopy* **84**, 47 (Jul, 2000).
23. J. F. Mansfield, Error Bars in Cbed Symmetry. *Ultramicroscopy* **18**, 91 (1985).
24. K. H. Kim, J. M. Zuo, Symmetry quantification and mapping using convergent beam electron diffraction. *Ultramicroscopy* **124**, 71 (Jan, 2013).
25. J. P. Lewis, Fast Template Matching. *Vision Interface* **95**, 120 (2009).
26. J. M. Zuo, M. Kim, M. O'Keeffe, J. C. H. Spence, Direct observation of d-orbital holes and Cu-Cu bonding in Cu₂O. *Nature* **401**, 49 (Sep 2, 1999).

27. J. M. Zuo, J. C. Mabon, Web-Based Electron Microscopy Application Software: Web-EMAPS. *Microscopy and Microanalysis* **10**, 1000 (2004).
28. A. J. F. Metherell, Diffraction of Electrons by Perfect Crystals. *Electron Microscopy in Materials Science, Third Course of the International School of Electron Microscopy, Commission of Euro Communities, Directorate General, "Scientific and Technical Information", Luxembourg*, (1975).
29. P. B. Hirsch, Howie, A., Nicholson, R., Pashley, D. W., Whelan, M. J., *Electron microscopy of thin crystals*. (R.E. Krieger Pub. Co., Huntington, N.Y., 1977).
30. C. J. Humphreys, The scattering of fast electrons by crystals. *Reports on Progress in Physics* **42**, 1825 (1979).
31. J. M. Cowley, A. F. Moodie, The Scattering of Electrons by Atoms and Crystals .1. A New Theoretical Approach. *Acta Crystallogr* **10**, 609 (1957).
32. K. Ishizuka, Multislice Formula for Inclined Illumination. *Acta Crystallographica Section A* **38**, 773 (1982).
33. L. Sturkey, Calculation of Electron Diffraction Intensities. *P Phys Soc Lond* **80**, 321 (1962).
34. D. Jacob, J. M. Zuo, A. Lefebvre, Y. Cordier, Composition analysis of semiconductor quantum wells by energy filtered convergent-beam electron diffraction. *Ultramicroscopy* **108**, 358 (Mar, 2008).

CHAPTER 3

NANOSCALE SYMMETRY FLUCTUATIONS IN FERROELECTRIC BARIUM TITANATE, BaTiO_3 ¹

Crystal charge density is a ground state electronic property. In ferroelectrics, charge is strongly influenced by lattice, or conversely, leading to a range of interesting temperature dependent physical properties. However, experimental determination of charge in ferroelectrics is challenging because of the formation of ferroelectric domains. Here, we demonstrate the scanning convergent beam electron diffraction (SCBED) technique that can be simultaneously used for imaging ferroelectric domains and identifying crystal symmetry and its fluctuations. Results from SCBED confirm the acentric tetragonal, orthorhombic, and rhombohedral symmetry for the ferroelectric phases of BaTiO_3 . However, the symmetry is not homogeneous; regions of few tens nm retaining almost perfect symmetry are interspersed in regions of lower symmetry. While the observed highest symmetry is consistent with the displacive model of ferroelectric phase transitions in BaTiO_3 , the observed nanoscale symmetry fluctuations are consistent with the predictions of the order-disorder phase transition mechanism.

¹ Y.-T. Shao and J.-M. Zuo, Nanoscale symmetry fluctuations in ferroelectric barium titanate, BaTiO_3 , (2017) Acta Cryst. B73, 708. Copyright 2017 International Union of Crystallography.

3.1. Introduction

Charge density varies spatially across ferroelectric domains. The domain sizes vary from tens of nanometers (nm) in relaxor-ferroelectrics to hundreds of nm or microns in ferroelectric crystals, such as BaTiO₃. The transition from paraelectric to ferroelectric phases in perovskite ferroelectrics (including BaTiO₃) can be described by a second-order Jahn-Teller distortion, which involves a delicate balance between short-range forces and long-range Coulomb interactions. The long-range Coulomb interactions favor ferroelectric distortion, while on the other hand, short-range repulsions between charged ions are minimized for centrosymmetric structures, which are preferred in the high temperature, paraelectric phase (1). The second-order Jahn-Teller effects give rise to the off-centre displacement of the small cation in the perovskite ferroelectrics such as BaTiO₃ and Pb(Zr,Ti)O₃, for example, BaTiO₃ successively transforms from the high-temperature paraelectric cubic (C) phase to three low-temperature ferroelectric phases with tetragonal (T), orthorhombic (O), and rhombohedral (R) symmetries (2). Phase transitions in BaTiO₃ are generally considered as a classic example of displacive soft-mode-type transitions, which results from the instability of the lattice against a soft polar phonon at the center of the Brillouin zone (3-5). Upon cooling below the Curie temperature, the ions are displaced from high-symmetry sites, which in turn generate a spontaneous dipole moment accompanied by a breaking of crystal symmetry (6). In the displacive model, the equilibrium position of each Ti atom is at the center of an oxygen octahedron for C, and displaced along $\langle 111 \rangle$, $\langle 011 \rangle$, $\langle 001 \rangle$ polarization directions for R, O, and T phases,

respectively. For the ferroelectric phases, the displacements are identical for all unit cells. However, this model fails to explain the heavily damped soft phonons, and contradicts experimental results obtained by x-ray fine structure (XAFS) (7), x-ray diffuse scattering (8, 9), and infrared reflectivity (IR) (10).

The spontaneous symmetry breaking, order-disorder, eight-site model was thus proposed to explain the failures of the displacive model (8, 11, 12). In this model, all Ti atoms in each unit cell are located in one of the eight $\langle 111 \rangle$ directions for all crystal phases. In the R-phase, this model assumes all the Ti atoms are displaced in the same direction. As temperature increases, the polarization can have one or more crystal orientations, which results in the breaking of local crystal symmetry in O-, T-, and C-phases (13-18). Nevertheless, this model fails to predict the heavily damped soft phonon modes near the paraelectric-ferroelectric phase transitions observed by inelastic neutron scattering (19, 20), IR (10), and hyperRaman scattering experiments (21).

A model combining the displacive and order-disorder models proposed by Girshberg and Yacoby successfully explained the soft mode overdamping near paraelectric-ferroelectric phase transitions (22). To explain the atomic origins of this model, Zhang *et al.* suggest there exists antiferroelectric coupling based on first-principles calculations (23). Their calculations successfully reproduced the x-ray diffuse scattering results, as well as providing an explanation of the overdamping of soft modes. However, the observed entropy changes (≤ 0.52 J/mol) for each transition in BaTiO₃ is far smaller than the entropy change in an order-disorder transition (5.76

J/mol, see (8) and (11)). To explain this, a short correlation length between 5 to 10 nm has been postulated (23).

Experimental clarification of the phase transition character in the model ferroelectric, BaTiO₃, requires 1) the identification of polarization domains, 2) a determination of the local crystal symmetry within a single domain, and 3) identification of the nature of polarization, structural distortions and chemical bonding. All three tasks are experimentally challenging.

Here, we describe an energy-filtered scanning convergent beam electron diffraction (EF-SCBED) study of the ferroelectric structures in single crystal BaTiO₃. In what follows, we first demonstrate the determination of 90° tetragonal domains and their polarizations. We then identify nanometer-sized regions of BaTiO₃ exhibiting mirror symmetry in accordance with the T-, O-, and R-symmetry in each of the corresponding phases at three different temperatures. The regions exhibiting high symmetry are surrounded by regions with broken symmetries, with the latter in agreement with the findings by Tsuda *et al.* (18) and Tsuda & Tanaka (17). The inhomogeneity in symmetry is explained by the anharmonicity in soft phonon modes and the population fluctuation of <111> nanopolar regions, with large implications for the origin of phase transitions in ferroelectric perovskites. Further, the identification of high symmetry regions in BaTiO₃ paves a way for future study of charge density in BaTiO₃.

3.2. Experimental methods

Top-seeded solution grown single crystal BaTiO₃ (substrate-grade, MaTeck Material-Technologie & Kristalle GmbH) was selected for this study. Thin TEM specimens were prepared along pseudocubic axes of [100]_C, [110]_C, and [111]_C using a focused ion beam (FIB) following the method described previously (24).

The principle of domain identification is based on determining the crystal symmetry using convergent beam electron diffraction (CBED). CBED is a well-established and powerful technique for determining crystal point and space group symmetry at the nanoscale (25-30). With the flexibility of illumination optics in a modern transmission electron microscope (TEM), local symmetry can be determined using a convergent electron probe of sizes ranging from sub-nanometer to several micrometers. Since the electron probe is convergent, the diffracted beams appear as disks instead of sharp spots in the recorded diffraction patterns. The crystal point group can thus be determined by a careful analysis of intensity patterns, also known as rocking curves, in the transmitted and diffracted disks.

Ferroelectric crystals can be characterized by an order parameter, the spontaneous polarization P_s vector, whose direction can be switched under the constraints of the crystal space group. The charge redistribution associated with polarization in ferroelectric crystals leads to the breakdown of Friedel's law when electron multiple scattering is involved. Thus, from CBED patterns taken along certain incident beam directions, we can determine the projected polarization direction,

which lies in a mirror plane. Furthermore, by matching with dynamic diffraction simulations using the Bloch wave method (31), we can retrieve the directions of the polarizations, and map the domain configurations and local symmetry variations in real space (32, 33).

Recent studies have demonstrated that the local crystal symmetry and polarization nanodomains can be determined using SCBED (29, 32, 33). By rastering the convergent electron probe over a region of the crystal, symmetry fluctuations and ferroelectric domains can be identified by the change in CBED patterns. A similar technique called STEM-CBED was used by Tsuda et al. for the same purpose (18). To quantify the symmetries of the CBED patterns, normalized cross-correlation values (γ) of a pair of diffraction discs expected to have symmetry relations were computed using the algorithm previously proposed by Kim *et al.* (34). For the convenience of having just one $\gamma_{\text{representative}}$ value for one CBED pattern, the γ values of each pair of discs were weighted with respect to intensity of the discs, or $\gamma_{\text{representative}} = \frac{\sum_g I_g \gamma_g}{\sum_g I_g}$ (35). To deal with intensity redistribution due to a small amount of lattice-rotations or a slight tilt of the incident electron probe, a DM (DigitalMicrograph[®]) script was developed to interactively adjust the radius and positions of the disks being used for symmetry quantification.

The electron diffraction experiments reported here were carried out using two TEMs. A JEOL 2200FS FEG TEM was operated at 200kV and 80kV with a convergent beam having a probe size at the crossover of 1.1nm in FWHM (full-width at half-maximum) along pseudocubic axes $[100]_c$ and $[110]_c$ through an in-column Omega energy filter with a window of 10eV centered on the zero-

loss peak (ZLP) in the electron energy-loss spectrum (EELS). The second TEM was a JEOL 2010F FEG TEM operated at 200kV with a beam of 1.6nm in FWHM along $[111]_c$ through a post-column GIF energy filter with a window of 10eV centered on the EELS ZLP. EF-SCBED was performed by positioning the focused electron probe on a selected area of a 25 x 25 grid, with step size of 1nm. A double-tilt Gatan liquid-nitrogen-cooling specimen holder was used for low temperature studies. Various SCBED experimental conditions in this text and the corresponding figures are summarized in Table 1 below.

Acceleration voltage (kV)	Zone axis	Temperature (K)	Corresponding figures
80	$[100]_c$	293	3(c)
80	$[110]_c$	293	3(d)
200	$[100]_c$	293	1(b); 2(a); 3(a); 3(b)
200	$[100]_c$	263	2(b)
200	$[100]_c$	95	2(c)
200	$[111]_c$	293	4(a)

Table 3.1. Summary of experimental conditions and corresponding CBED figures. The subscript *C* indicates the incident beam direction in the pseudocubic coordinate.

The CBED simulation is based on the Bloch-wave method (Zuo 1992), using the neutral atomic scattering factors of Doyle and Turner (36), absorption parameters of Bird and King (37), a total of 120 beams and 3209 incident beam directions within the CBED disk.

3.3. Results

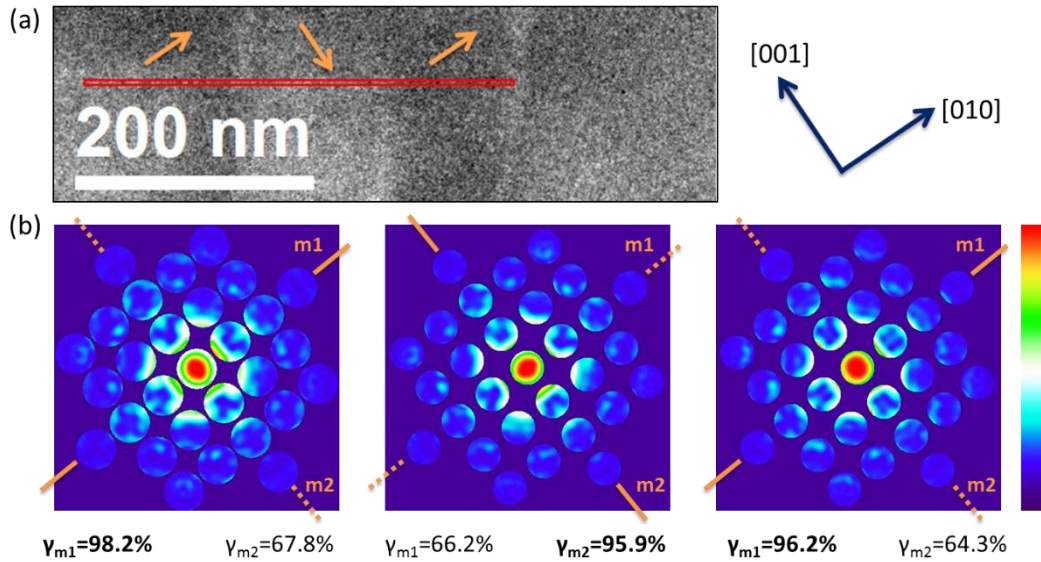


Figure 3.1. Identification of 90° ferroelectric domains using scanning CBED. (a) Bright-field image of the sample viewed along $[100]_c$. The red box indicates the scanned region of $360\text{nm} \times 6\text{nm}$, whereas the orange arrows indicate polarization directions. The symmetry of CBED patterns were quantified along two different mirror plane directions, $m1$ and $m2$. (b) Representative experimental CBED patterns of three 90° domains, from left to right, with high cross-correlation coefficient (γ) values of $\gamma_{m1} = 98.2\%$, $\gamma_{m2} = 95.9\%$, $\gamma_{m1} = 96.2\%$, respectively.

Three adjacent head-to-tail 90° domains in BaTiO_3 are identified at room temperature in Fig. 1(a), which are distinguished by the CBED patterns in Fig. 1(b). The CBED patterns were recorded along the $[100]_C$ (c for the pseudo-cubic direction) incident direction [Fig. 1(b)]. The SCBED was performed in the scanned region marked as the red rectangular box in Fig. 1(a), which was sampled by 180×3 points, with a step size of 2nm . We observed the tetragonal 90° domains, where the

alternating mirror plane directions rotated by 90 degrees, as shown in Fig. 1(b). Symmetry in the CBED patterns are quantified along two mirror plane directions, m_1 and m_2 . The highest γ_m values in each domain, from left to right, are $\gamma_{m1}=98.2\%$, $\gamma_{m2}=95.9\%$, and $\gamma_{m1}=96.2\%$, respectively. From the change in γ_{m1} and γ_{m2} values, we found the domain wall width is about 2-4nm, which is consistent with previous studies using x-ray powder diffraction (38) or high-resolution electron microscopy (39, 40).

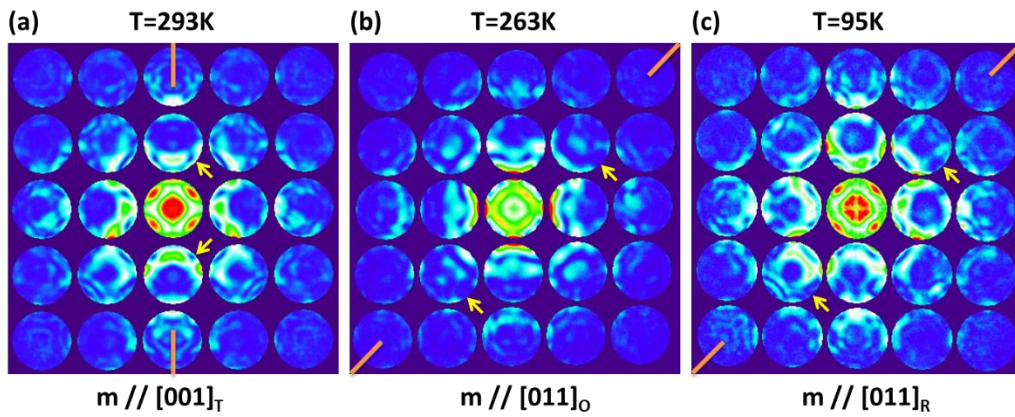


Figure 3.2. CBED patterns of $BaTiO_3$ single crystal having highest symmetry along $[100]_C$ at various temperatures. Mirror planes are marked by lines, with quantified mirror symmetry of (a) $\gamma_m = 98.5\%$ in the T-phase (b) $\gamma_m = 98.7\%$ in the O-phase and (c) $\gamma_m = 97.5\%$ in the R-phase. The reflections on the mirror plane marked by yellow arrows show the breaking of Friedel's law due to dynamic diffraction effects.

Figure 2 shows the representative CBED patterns of $BaTiO_3$ for the tetragonal, orthorhombic, and rhombohedral phases, upon cooling from room temperature to approximately 95 K. The EF-SCBED scans were acquired near the same sample regions along the $[100]_C$ zone-axis incidence.

The mirror planes are indicated by the lines marked in the CBED patterns. The arrows mark the reflections on the mirror plane showing the breakdown of Friedel's law due to dynamic diffraction effects. The quantified mirror symmetry for the three representative CBED patterns are $\gamma_{m,Tetragonal}=98.5\%$, $\gamma_{m,Orthorhombic}=98.7\%$, and $\gamma_{m,Rhombohedral}=97.5\%$, with mirror directions parallel to $[001]_T$, $[011]_O$, and $[011]_R$, respectively. The mirror plane directions for CBED patterns taken at 298, 263, and 95 K are consistent with the space groups of $P4mm$, $Amm2$, $R3m$, respectively.

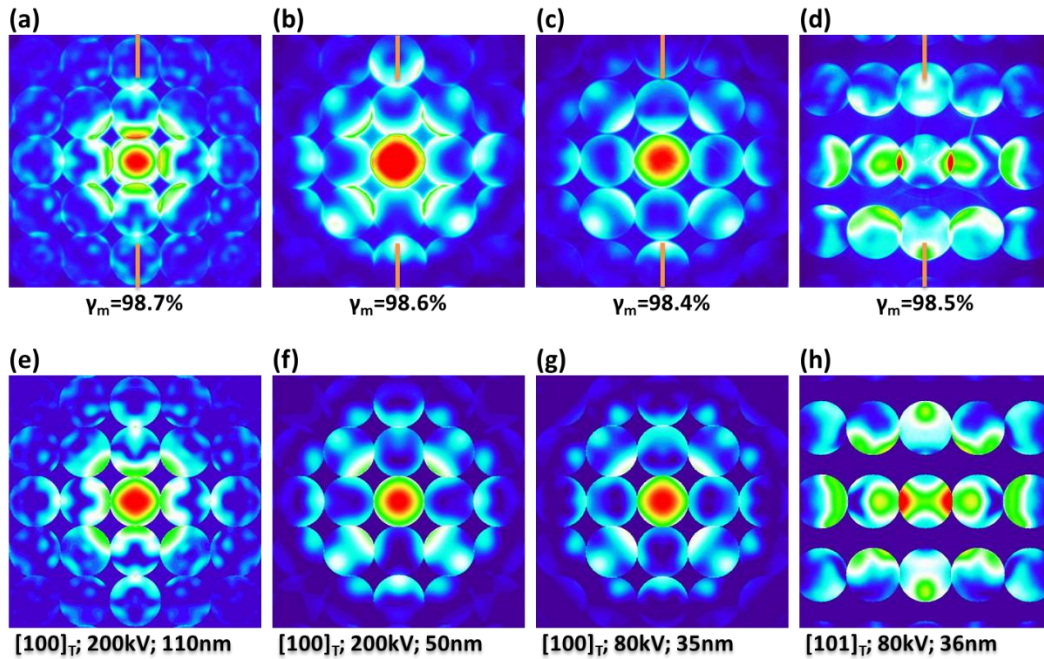


Figure 3.3. Experimental and simulated CBED patterns of the tetragonal-phase at various thicknesses. Representative experimental CBED patterns possessing the highest mirror symmetry obtained along $[100]_C$ with cross-correlation coefficients of (a) $\gamma_m = 98.7\%$ (b) $\gamma_m = 98.6\%$ (c) $\gamma_m = 98.6\%$, and (d) along $[110]_C$ with $\gamma_m = 98.7\%$. The simulated patterns of tetragonal phase $BaTiO_3$ ($P4mm$) using the Bloch-wave method with thicknesses of (e) 110nm (200kV), (f) 50nm (200kV), (g) 35nm (80kV), and (h) 36nm (80kV) correspond to the experimental (a), (b), (c), and (d) patterns, respectively.

To investigate the specimen thickness effects on local symmetry, CBED patterns were recorded from regions of different specimen thickness, zone-axis incidence, and accelerating voltage [Figs. 3(a-d)]. For the thinner TEM specimen, we operated the 2200FS FEG TEM at 80kV for a longer wavelength and stronger multiple scattering effects in order to enhance the contrast in the recorded CBED patterns. The simulated CBED patterns [Figs. 3(e), 3(f), 3(g), and 3(h)] correspond to the experimental CBED patterns [Figs. 3(a), 3(b), 3(c), and 3(d)], respectively. Lattice parameters were set to the tetragonal phase (4I), and neutral atomic scattering factors were used as inputs for CBED simulations. Figures 3(a) and 3(b) show experimental patterns recorded with the 200kV electrons, with the mirror symmetry measured at $\gamma_m=98.7\%$ and $\gamma_m=98.6\%$, respectively. The corresponding simulated CBED patterns are along $[100]_T$ incidence, shown in Figs. 3(e) and 3(f), with the best matching specimen thicknesses of 110 nm and 50 nm, respectively. Figures 3(c) and 3(d) show experimental patterns recorded with the 80kV electrons along $[100]_C$ and $[110]_C$ incidences, with mirror symmetry measured at $\gamma_m=98.4\%$ and $\gamma_m=98.5\%$, respectively. The corresponding simulated CBED patterns are along $[100]_T$ and $[101]_T$ incidence, as shown in Figs. 3(g) and 3(h) with the best matching specimen thickness at 35 nm and 36 nm, respectively. For a probe of about 1nm at FWHM, Figure 3 shows that the BaTiO₃ crystal still preserves tetragonal symmetry with the probed crystal volumes from $\sim 110 \text{ nm}^3$ down to $\sim 35 \text{ nm}^3$ at room temperature.

Figure 4 shows the representative CBED patterns and the symmetry maps obtained by EF-SCBED taken along the $[111]_C$ zone-axis. The scanned region consists of 12 by 25 points, with a step size of 2 nm. Figure 4(a) shows the experimental CBED pattern with highest symmetry with $\gamma_{m(1,1)}=95.4\%$ compared to the average value of $\gamma_{m(1,1)}=83.1\%$ over the entire scanned area. Six possible projected 2D mirror plane directions can be expressed by (m, n) as the linear combination of two basis vectors \vec{g} & \vec{h} , namely $\vec{M} = m\vec{g} + n\vec{h}$. Possible mirror plane directions along $[111]_C$ incidence for tetragonal and rhombohedral symmetries are labeled in with orange solid lines. The corresponding simulated CBED pattern is shown in Fig. 4(d), with incident beam along the $[1\bar{1}1]_T$, with a mirror plane parallel to $[\bar{1}12]_T$, and specimen thickness of 135nm. The maps of spatial variations in mirror symmetry quantified along $(1,1)$, $(1,\bar{1})$, $(1,0)$, and $(0,1)$ are shown in Figs. 4(b), 4(c), 4(e), and 4(f), respectively. Figure 4(b) shows the tetragonal symmetry is preserved in regions of $\sim 15\text{nm}$ in the lateral direction.

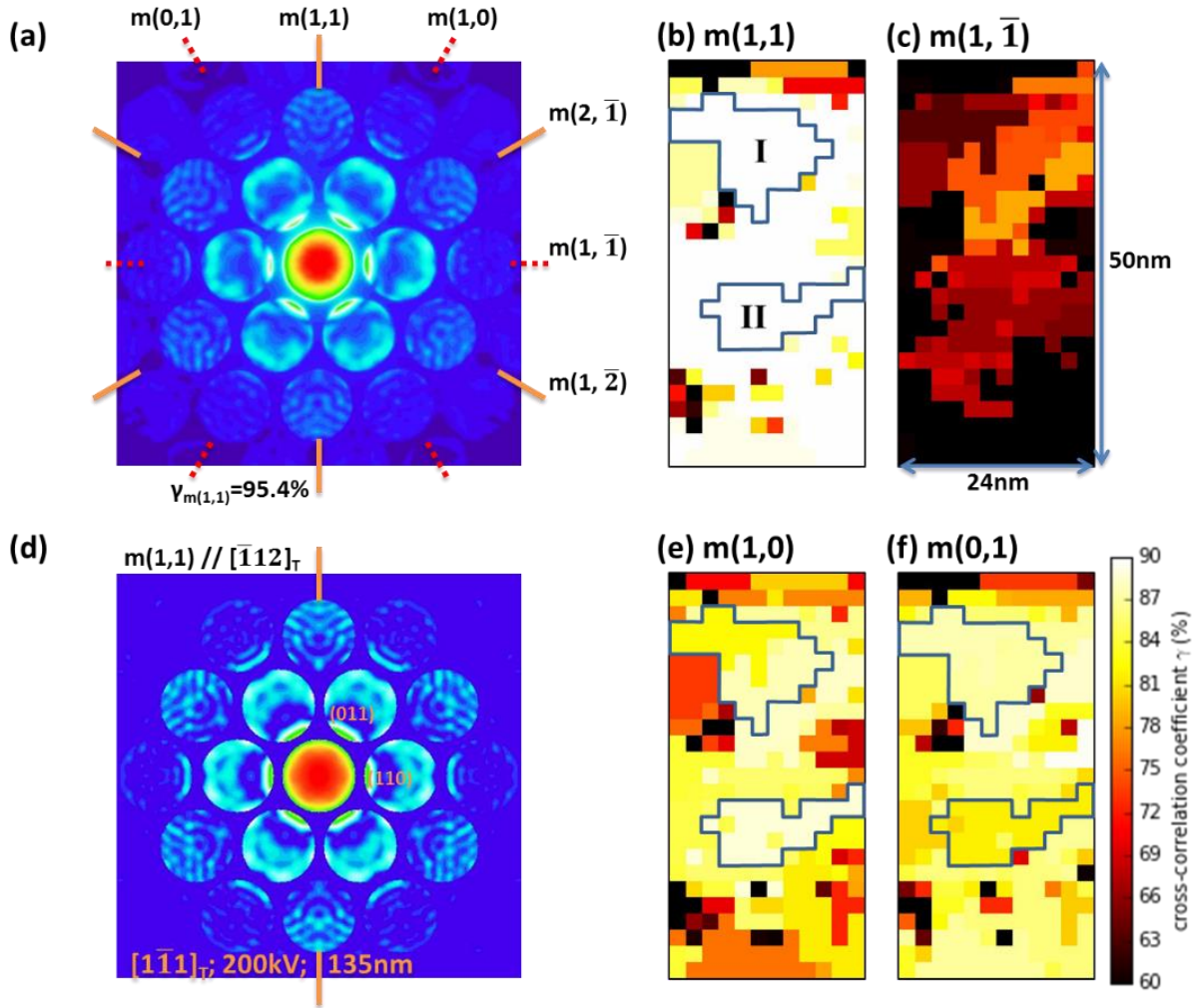


Figure 3.4. Symmetry maps of tetragonal-phase BaTiO_3 along $[111]_c$ zone axis. The scanned region is $24\text{nm} \times 50\text{nm}$. (a) The six possible mirror plane directions can be expressed by (m,n) , where $\vec{M} = m\vec{g} + n\vec{h}$ and \vec{g} & \vec{h} being the two basis vectors. Mirror planes corresponding to tetragonal and rhombohedral phases are labeled with orange solid lines. Representative experimental CBED pattern possessing highest mirror symmetry with cross-correlation coefficients of $\gamma_{m(1,1)} = 95.4\%$, which corresponds to region-I in (b). Figure (d) shows the corresponding simulated tetragonal phase CBED pattern along $[1\bar{1}1]_c$ zone axis, with the thicknesses of 135nm , and mirror plane $m//[\bar{1}12]_T$. Figures (c), (d), (e), and (f) show the symmetry maps quantified along mirror planes parallel to $(1,1)$, $(1,\bar{1})$, $(1,0)$, and $(0,1)$, respectively.

3.4. Discussion

The symmetry information obtained from the experimental CBED patterns reflects the ferroelectric polarizations, averaged over all unit cells illuminated by the electron beam. In the column approximation (31), the illuminated volume of crystal is roughly the product of probe diameter squared and specimen thickness. The above results using BaTiO₃ as a model ferroelectric demonstrate that SCBED can be used to identify the ferroelectric domains and determine polarization direction at various temperatures. The highest symmetry identified by SCBED is consistent with the T-, O-, and R-symmetry previously reported. Further, we observed that the tetragonal symmetry is well preserved within a crystal volume ranging from 35nm³ to 110nm³, as shown Figs. 3(a-d). However, the regions with the high tetragonal symmetry of ~15nm in diameter are surrounded by regions with symmetry breaking, as shown in Fig. 4(b).

Ferroelectric phase transition is traditionally explained by the displacive phase transition model (42). Within this model, local symmetry breaking can be explained by the anharmonicity of soft phonons (43-46). The interference of different phonon frequencies leads to a vibrating lattice wave packet, which causes structural distortions via strong electron-phonon coupling (47, 48).

An alternative explanation is the order-disorder model. Previously, Tsuda *et al.* suggested that the tetragonal structure consists of rhombohedral nanoclusters using the STEM-CBED technique (16, 18). Within the order-disorder interpretation, the observed tetragonal symmetry can possibly be a result of <111> polarizations averaged over 35nm³, or ~540 unit cells, assuming a column of

1nm in diameter and 35nm thick. For example, Figs. 5(b) and 5(c) show the polarization directions projected along the $[100]_c$ viewing direction for the order-disorder model and anti-ferroelectric coupling model, respectively. The polarization components along $[100]_c$ and $[010]_c$ cancel each other, which effectively results in an averaged polarization along $[001]_c$.

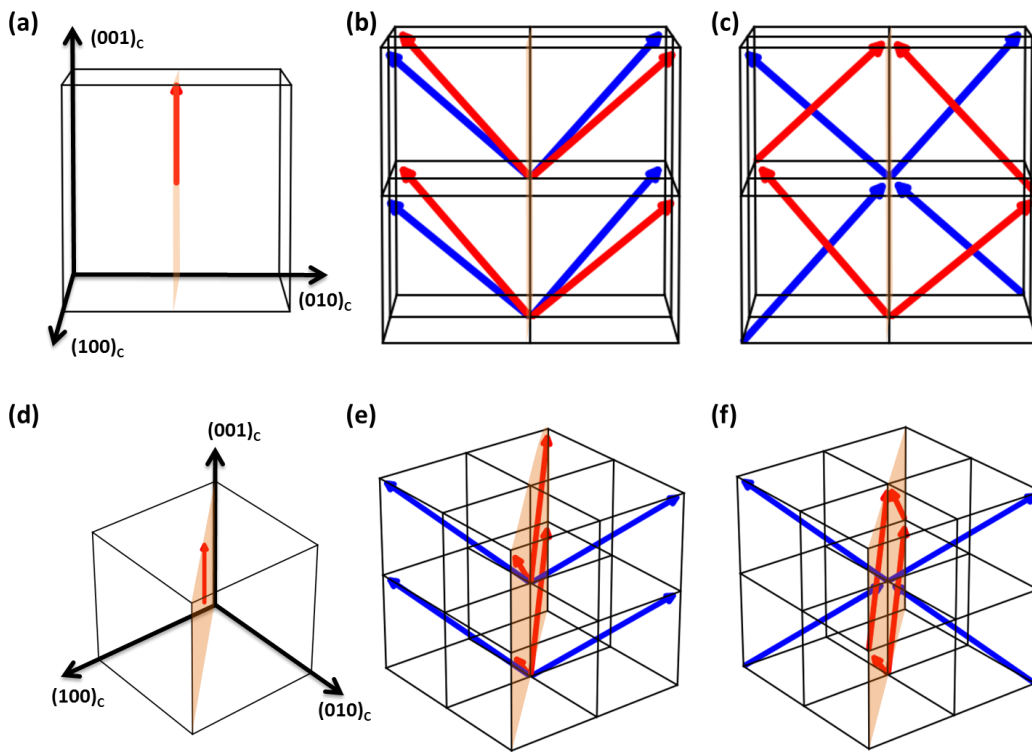


Figure 3.5. Structural models of the tetragonal phase corresponding to various ferroelectric phase transition mechanisms. The structure models in the first row are viewed along the $[100]_c$ direction, and the second row is viewed along $[111]_c$. Figures (a, d), (b, e), and (c, f) correspond to displacive, order-disorder, and anti-ferroelectric type ferroelectric phase transition mechanisms, respectively. The arrows indicate the polarization directions in a unit cell. Different colors of arrows indicate the polarizations lying in different diagonal planes.

A hint of $\langle 111 \rangle$ polarizations averaging is provided by the symmetry maps obtained from SCBED along the $[111]_C$ zone axis, as shown in Figs. 4(e) and 4(f). In both order-disorder (Fig. 5(e)) and anti-ferroelectric coupling models (Fig. 5(f)), the four red $\langle 111 \rangle$ polarizations lie in the $[110]_C$ plane, which results in the observed highest mirror symmetry along $m(1,1)$ (Fig. 4(b)). The orange lines ($m(1,1)$, $m(2, \bar{1})$, and $m(1, \bar{2})$) in Figure 4 represent the 3D projected mirror planes, while the red dashed lines ($m(0,1)$, $m(1,0)$, and $m(1, \bar{1})$) do not have corresponding 3D mirror planes. We noticed that region-I possesses a higher mirror symmetry along $m(0,1)$ than $m(1,0)$, while it is the opposite case for region-II (Figs. 4(e) and 4(f)). Since $m(0,1)$ and $m(1,0)$ have no corresponding 3D mirror planes, the observed “pseudo-mirror” of $m(0,1)$ and $m(1,0)$ can be a result of superimposed $m(1,1)$ with $m(1, \bar{2})$ and $m(2, \bar{1})$, respectively. The projected symmetry fluctuation thus may be explained by the population difference of $\langle 111 \rangle$ polarizations within the volume illuminated by the electron beam. A knowledge of population fluctuations along the electron beam direction is then required to understand the observed 2D symmetry. Unfortunately, symmetry analysis alone does not provide such information.

It has been suggested that the simultaneous presence of soft phonon modes and Ti ion off-center displacements leads to a coexisting displacive and order-disorder character (49). The temperature-dependent structural distortion and bonding of BaTiO_3 was recently investigated using electron energy-loss spectroscopy (EELS) by studying the fine structure in the O-K edge and Ti-L₂₃ edge (50). The study of Bugnet et al. suggested that the paraelectric phase is not cubic

but tetragonal-like, which is in good agreement with the work of Zalar *et al.* (43, 44). However, first principles calculations do not reproduce the overall shape of O-K edge, hence hinders the quantitative interpretation of the FSs.

We noticed the difference in experimental and simulated CBED patterns using neutral atomic scattering factors, as shown in Fig. 3. The difference is most obvious in diffracted disks nearest to the transmitted disk, which is most sensitive to chemical bonding. The simulated CBED patterns using ionic scattering factors did not resemble the experimental patterns, which implies the bonding to be more covalent. To further understand the microscopic origin of ferroelectric phase transitions, there is a need to investigate the local crystal bonding in BaTiO₃, with even smaller illuminated volumes than the present study. The SCBED study reported here paves the way for a future investigation of the local chemical bonding and charge density distributions by measuring low-order structure factors using quantitative CBED (51-53) and using the multipole-model that Prof. Coppens and his collaborators have pioneered (54, 55).

3.5. Conclusions

In conclusion, we have identified regions of ~15nm of BaTiO₃ possessing high symmetry surrounded by symmetry breaking regions using the EF-SCBED technique. The crystal still preserves tetragonal symmetry within a local volume of 35nm³. The symmetry breaking can be

explained by both anharmonicity in soft phonon modes or Ti ion off-centering averaged over the crystal volume probed by the electron beam.

3.6. References

1. R. E. Cohen, Origin of Ferroelectricity in Perovskite Oxides. *Nature* **358**, 136 (Jul 9, 1992).
2. G. H. Kwei, A. C. Lawson, S. J. L. Billinge, S. W. Cheong, Structures of the Ferroelectric Phases of Barium-Titanate. *Journal of Physical Chemistry* **97**, 2368 (Mar 11, 1993).
3. W. Cochran, Crystal Stability and the Theory of Ferroelectricity. *Advances in Physics* **9**, 387 (1960).
4. J. Harada, J. D. Axe, G. Shirane, Neutron Scattering Study of Soft Phonon Modes in Cubic Batio₃. *B Am Phys Soc* **16**, 51 (1971).
5. G. Shirane, B. C. Frazer, V. J. Minkiewicz, J. A. Leake, A. Linz, Soft Optic Modes in Barium Titanate. *Phys Rev Lett* **19**, 234 (1967).
6. M. E. Lines, A. M. Glass, *Principles and applications of ferroelectrics and related materials*. Oxford classic texts in the physical sciences (Clarendon Press; Oxford University Press, Oxford New York, 2001), pp. xiii, 680 p.
7. B. Ravel, E. A. Stern, R. I. Vedral, V. Kraizman, Local structure and the phase transitions of BaTiO₃. *Ferroelectrics* **206**, 407 (1998).
8. R. Comes, M. Lambert, A. Guinier, Chain Structure of Batio₃ and Knbo₃. *Solid State Communications* **6**, 715 (1968).
9. R. Comes, M. Lambert, A. Guinier, Linear Disorder in Crystals (Silicon, Quartz and Ferroelectric Perovskites). *Acta Crystallographica Section a-Crystal Physics Diffraction Theoretical and General Crystallography A* **26**, 244 (1970).
10. Y. Luspain, J. L. Servoin, F. Gervais, Soft Mode Spectroscopy in Barium-Titanate. *Journal of Physics C-Solid State Physics* **13**, 3761 (1980).
11. A. S. Chaves, F. C. S. Barreto, R. A. Nogueira, B. Zeks, Thermodynamics of an 8-Site Order-Disorder Model for Ferroelectrics. *Phys Rev B* **13**, 207 (1976).
12. H. Takahasi, A Note on Theory of Barium Titanate. *J Phys Soc Jpn* **16**, 1685 (1961).
13. J. Harada, M. Watanabe, S. Kodera, G. Honjo, Diffuse Streak Diffraction Pattern of Electron and X-Rays Due to Low Frequency Optical Mode in Tetragonal Batio₃. *J Phys Soc Jpn* **20**, 630 (1965).
14. J. Harada, M. Tanaka, G. Honjo, Thermal Diffuse Streak in Electron Diffraction and Low Frequency Transverse Optic Lattice Waves of Barium Titanate. *J Phys Soc Jpn* **21**, 968 (1966).

15. G. Honjo, S. Kodera, N. Kitamura, Diffuse Streak Diffraction Patterns from Single Crystals .I. General Discussion + Aspects of Electron Diffraction Diffuse Streak Patterns. *J Phys Soc Jpn* **19**, 351 (1964).
16. K. Tsuda, R. Sano, M. Tanaka, Nanoscale local structures of rhombohedral symmetry in the orthorhombic and tetragonal phases of BaTiO₃ studied by convergent-beam electron diffraction. *Phys Rev B* **86**, 214106 (Dec 17, 2012).
17. K. Tsuda, M. Tanaka, Direct observation of the symmetry breaking of the nanometer-scale local structure in the paraelectric cubic phase of BaTiO₃ using convergent-beam electron diffraction. *Applied Physics Express* **9**, 071501 (Jul, 2016).
18. K. Tsuda, A. Yasuhara, M. Tanaka, Two-dimensional mapping of polarizations of rhombohedral nanostructures in the tetragonal phase of BaTiO₃ by the combined use of the scanning transmission electron microscopy and convergent-beam electron diffraction methods. *Appl Phys Lett* **103**, 082908 (Aug 19, 2013).
19. J. Harada, J. D. Axe, G. Shirane, Neutron-Scattering Study of Soft Modes in Cubic Batio₃. *Phys Rev B* **4**, 155 (1971).
20. Y. Yamada, G. Shirane, A. Linz, Study of Critical Fluctuations in Batio₃ by Neutron Scattering. *Physical Review* **177**, 848 (1969).
21. H. Vogt, J. A. Sanjurjo, G. Rossbroich, Soft-Mode Spectroscopy in Cubic Batio₃ by Hyper-Raman Scattering. *Phys Rev B* **26**, 5904 (1982).
22. Y. Girshberg, Y. Yacoby, Ferroelectric phase transitions in perovskites with off-center ion displacements. *Solid State Communications* **103**, 425 (Aug, 1997).
23. Q. S. Zhang, T. Cagin, W. A. Goddard, The ferroelectric and cubic phases in BaTiO(3) ferroelectrics are also antiferroelectric. *Proceedings of the National Academy of Sciences of the United States of America* **103**, 14695 (Oct 3, 2006).
24. M. Schaffer, B. Schaffer, Q. Ramasse, Sample preparation for atomic-resolution STEM at low voltages by FIB. *Ultramicroscopy* **114**, 62 (Mar, 2012).
25. B. F. Buxton, J. A. Eades, J. W. Steeds, G. M. Rackham, The Symmetry of Electron Diffraction Zone Axis Patterns. *Philosophical Transactions of the Royal Society of London. Series A, Mathematical and Physical Sciences* **281**, 171 (1976).
26. J. M. Cowley, P. Goodman, B. K. Vainshtein, B. B. Zvyagin, D. L. Dorset, in *International Tables for Crystallography Volume B: Reciprocal space*, U. Shmueli, Ed. (Springer Netherlands, Dordrecht, 2006), pp. 276-345.
27. J. P. Morniroli, J. W. Steeds, Microdiffraction as a Tool for Crystal-Structure Identification and Determination. *Ultramicroscopy* **45**, 219 (Sep, 1992).
28. M. Tanaka, K. Tsuda, Convergent-beam electron diffraction. *J Electron Microsc* **60**, S245 (Aug, 2011).
29. K. H. Kim, D. A. Payne, J. M. Zuo, Determination of fluctuations in local symmetry and measurement by convergent beam electron diffraction: applications to a relaxor-based ferroelectric crystal after thermal annealing. *J Appl Crystallogr* **46**, 1331 (Oct, 2013).

30. J. M. LeBeau, S. D. Findlay, L. J. Allen, S. Stemmer, Position averaged convergent beam electron diffraction: Theory and applications. *Ultramicroscopy* **110**, 118 (Jan, 2010).
31. J. M. Zuo, J. C. H. Spence, *Advanced Transmission Electron Microscopy*. Imaging and Diffraction in Nanoscience (New York: Springer, ed. 1, 2017), pp. XXVI, 729.
32. K. H. Kim, D. A. Payne, J. M. Zuo, Determination of 60 degrees polarization nanodomains in a relaxor-based ferroelectric single crystal. *Appl Phys Lett* **107**, 162902 (Oct 19, 2015).
33. Y.-T. Shao, J.-M. Zuo, Lattice-rotation vortex at the charged monoclinic domain boundary in a relaxor ferroelectric crystal. *Phys Rev Lett*, accepted (2017).
34. K. H. Kim, J. M. Zuo, Symmetry quantification and mapping using convergent beam electron diffraction. *Ultramicroscopy* **124**, 71 (Jan, 2013).
35. Y.-T. Shao, J.-M. Zuo, Fundamental Symmetry of Barium Titanate Single Crystal Determined Using Energy-Filtered Scanning Convergent Beam Electron Diffraction. *Microscopy and Microanalysis* **22**, 516 (2016/007/001, 2016).
36. P. A. Doyle, P. S. Turner, Relativistic Hartree-Fock X-Ray and Electron Scattering Factors. *Acta Crystallographica Section a-Crystal Physics Diffraction Theoretical and General Crystallography* **A 24**, 390 (1968).
37. D. M. Bird, Q. A. King, Absorptive Form-Factors for High-Energy Electron-Diffraction. *Acta Crystallographica Section A* **46**, 202 (Mar 1, 1990).
38. N. Floquet, C. Valot, Ferroelectric domain walls in BaTiO₃: Structural wall model interpreting fingerprints in XRPD diagrams. *Ferroelectrics* **234**, 107 (1999).
39. F. Tsai, V. Khiznichenko, J. M. Cowley, High-Resolution Electron-Microscopy of 90-Degrees Ferroelectric Domain Boundaries in BaTiO₃ and Pb(Zr_{0.52}Ti_{0.48})O₃. *Ultramicroscopy* **45**, 55 (Aug, 1992).
40. M. Tanaka, G. Honjo, Electron Optical Studies of Barium Titanate Single Crystal Films. *J Phys Soc Jpn* **19**, 954 (1964).
41. A. Rother *et al.*, X-ray investigation, high-resolution electron holography, and density functional calculations of single-crystalline BaTiO₃. *Phys Rev B* **74**, 134116 (Oct, 2006).
42. L. E. Orgel, Ferroelectricity and the Structure of Transition-Metal Oxides. *Discussions of the Faraday Society*, 138 (1958).
43. B. Zalar, V. V. Laguta, R. Blinc, NMR evidence for the coexistence of order-disorder and displacive components in barium titanate. *Phys Rev Lett* **90**, 037601 (Jan 24, 2003).
44. B. Zalar *et al.*, NMR study of disorder in BaTiO₃ and SrTiO₃. *Phys Rev B* **71**, 064107 (Feb, 2005).
45. G. Volkel, K. A. Muller, Order-disorder phenomena in the low-temperature phase of BaTiO₃. *Phys Rev B* **76**, 094105 (Sep, 2007).
46. K. A. Muller, W. Berlinger, Microscopic Probing of Order-Disorder Versus Displacive Behavior in BaTiO₃ by Fe-3+ Electron-Paramagnetic-Res. *Phys Rev B* **34**, 6130 (Nov 1, 1986).

47. Y. Girshberg, Y. Yacoby, Ferroelectric phase transitions and off-centre displacements in systems with strong electron-phonon interaction. *J Phys-Condens Mat* **11**, 9807 (Dec 6, 1999).
48. W. Zhong, R. D. Kingsmith, D. Vanderbilt, Giant Lo-to Splitting Sin Perovskite Ferroelectrics. *Phys Rev Lett* **72**, 3618 (May 30, 1994).
49. E. A. Stern, Character of order-disorder and displacive components in barium titanate. *Phys Rev Lett* **93**, 037601 (Jul 16, 2004).
50. M. Bugnet, G. Radtke, S. Y. Woo, G. Z. Zhu, G. A. Botton, Temperature-dependent high energy-resolution EELS of ferroelectric and paraelectric BaTiO₃ phases. *Phys Rev B* **93**, 020102 (Jan 7, 2016).
51. J. M. Zuo, M. Kim, M. O'Keeffe, J. C. H. Spence, Direct observation of d-orbital holes and Cu-Cu bonding in Cu₂O. *Nature* **401**, 49 (Sep 2, 1999).
52. B. Jiang, J. M. Zuo, J. Friis, J. C. H. Spence, On the consistency of QCBED structure factor measurements for TiO₂ (rutile). *Microscopy and Microanalysis* **9**, 457 (Oct, 2003).
53. J. C. H. Spence, J. M. Zuo, *Electron microdiffraction*. (Plenum Press, 1992).
54. P. Coppens, *X-ray charge densities and chemical bonding*., (International Union of Crystallography, 1997).
55. P. Coppens, Charge-density analysis at the turn of the century. *Acta Crystallographica Section A* **54**, 779 (Nov 1, 1998).

CHAPTER 4

LATTICE ROTATION VORTEX AT THE MONOCLINIC DOMAIN BOUNDARY IN RELAXOR FERROELECTRIC CRYSTAL¹

We present evidences of lattice rotation vortices having an average radius of ~ 7 nm at the ferroelectric domain boundary of $(1-x)\text{Pb}(\text{Zn}_{1/3}\text{Nb}_{2/3})\text{O}_3-x\text{PbTiO}_3$ ($x=0.08$). Maps of crystal orientations and domain symmetry breaking are obtained using scanning convergent beam electron diffraction (SCBED), which show fractional rotation vortices near the 50° monoclinic domain walls. The merging of 2D and 1D topological defects is consistent with inhomogeneous boundary charge and expected to have a large impact on the domain-switching mechanisms in relaxor ferroelectric crystals and ferroelectric devices.

4.1. Introduction

Topological defects, such as ferroelectric domain walls (DWs), exhibit emergent physical properties with potential applications in electronic devices. For example, charged DWs of BiFeO_3 (1) and $\text{Pb}(\text{Zr}, \text{Ti})\text{O}_3$ (2) exhibit a significant conductivity increase compared to bulk materials, which is movable and can be advantageous for device applications (3). DWs involve a change in the polarization direction and small lattice distortions. Having a large density of mobile DWs also

¹ Y.-T. Shao and J.-M. Zuo, Lattice-rotation vortex at the charged monoclinic domain boundary in a relaxor ferroelectric crystal, (2017) Phys. Rev. Lett., 118, 157601. Copyright 2017 American Physical Society.

facilitates domain switching and therefore dramatically enhances the susceptibility of ferroelectrics and piezoelectric coupling coefficients (4).

Extensive studies of ferroelectric domains by microscopy (5, 6) and diffraction (7-18) have demonstrated that ferroelectric DWs can be categorized by the dipole transition behaviors across the boundary, which are non-chiral DWs (Ising-like), chiral DWs (Bloch- or Neel-like), or mixtures of both (19). However, recent atomic resolution electron imaging revealed polarization rotation vortex in tetragonal $\text{Pb}(\text{Zr,Ti})\text{O}_3$ (20, 21), rhombohedral BiFeO_3 (22) crystals and the superlattices of SrTiO_3 and PbTiO_3 (23, 24). Furthermore, in lead-based complex perovskite oxides having the chemical formula $(1-x)\text{Pb}(\text{B}'_{1/3}\text{B}''_{2/3})\text{O}_{3-x}\text{Pb}(\text{B}'''+4)\text{O}_3$ ($\text{B}', \text{B}'', \text{B}''' = \text{Zn, Nb, Ti}$ for PZN-PT, and Mg, Nb, Ti for PMN-PT), exceptional piezoelectric properties (25) are obtained at the morphotropic phase boundary (MPB), where nanometer-sized monoclinic domains have been reported by X-ray diffraction (5, 26), neutron diffraction (9, 10, 12, 17, 18), and electron microscopy (7, 11, 14). On the other hand, we know little about the structure and properties of DWs in monoclinic crystals. Theory predicts mechanically permissible but slightly charged DWs parallel to 100 or 110 planes in addition to 180° DWs (27, 28). The structural determination of DWs in general requires 1) identifying two neighboring polarization domains, 2) determining the transition structure between the domains, and 3) identifying the nature of the polarization in the transition region. All three tasks are experimentally difficult for determining monoclinic, and nanometer-sized, domains, and consequently there was no good experimental means to study in

relaxor ferroelectrics the coupling between electric dipoles and strain, which can induce chirality at the DWs (29).

Here, we describe a scanning convergent beam electron diffraction (SCBED) study of the DWs in the relaxor-based ferroelectric crystal of PZN-8%PT. Using energy-filtered (EF) SCBED, we have identified nm-sized domains having monoclinic (M) Pm symmetry in single crystal PZN-8%PT. A careful examination of the DWs revealed the presence of lattice rotation vortices near DWs. These vortices involve continuous lattice rotation across length scales of ~ 15 nm in diameter.

4.2. Experimental methods

Single crystal PZN-8%PT (unpoled flux-grown single crystal, Microfine Materials Technologies Pte. Ltd., Singapore) was selected for study. Thin crystals were prepared along pseudocubic axes of $[100]_C$, $[001]_C$, and $[111]_C$ (C for pseudo-cubic axes) using the method described previously (30). The same sample preparation procedure was applied successfully for the determination of symmetry in single crystal $BaTiO_3$ (31).

The principle of domain identification is based on CBED determination of crystal symmetry. A focused electron probe is rastered across a region of the sample and used to record diffraction patterns. Because of the convergent beam, the diffracted beam appears as a disk instead of a sharp diffraction spot and CBED has the spatial resolution ranging from few to hundreds of nanometer

(32-34). The crystal point group can be obtained at different sample points by careful study of 2D features in transmitted disk and diffracted disks. Specifically, the ferroelectric polarization direction which lies in the mirror plane can be determined from multiple scattering effects for certain incident beam directions. Thus, ferroelectric domains can be identified by the change of CBED pattern symmetry (Fig. 1). For example, the mirror direction can be used to determine the 60° domains in PMN-31%PT with the aid of dynamic diffraction simulation using the Bloch wave method (35, 36). The change in CBED pattern symmetry is quantified using the normalized cross-correlation (γ_m) value of a pair of diffraction discs related by mirror symmetry using the algorithm previously proposed by Kim et al. (37). For convenience of having just one γ_m value for one CBED pattern, the γ_m values of three pairs of discs with the highest intensity were averaged, noted as $\gamma_{m,average}$ shown in Fig. 1(a). By scanning the electron probe over a region of crystals and recording and quantifying CBED patterns for scanning CBED, the crystal symmetry can be mapped. Figure 1(d) shows an example. CBED patterns of different $\gamma_{m,average}$ values are indicated by different colors in Fig. 1(d).

For determining the crystal rotation, we use the BF disk (transmitted beam) of CBED, which possesses the center of symmetry belonging to the Laue diffraction group according to Buxton et al. (32). The location of the center of symmetry changes when crystal rotates as illustrated in Fig. 1(b) and (c).

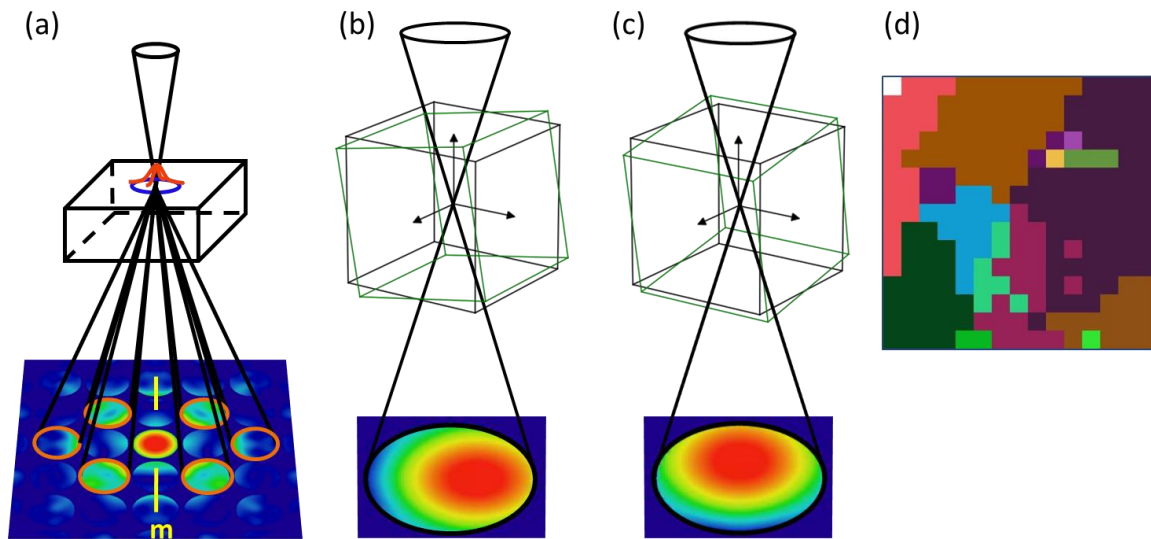


Figure 4.1. Principles of using CBED for determining mirror symmetry and crystal rotation. Figure (a) shows an example for the mirror symmetry quantification, while crystal rotation along the x - and y -axes leads to a shift in the center of the CBED (000) pattern as shown in (b) and (c). The average of the cross-correlation coefficients of three pairs of discs labeled in orange in (a) is taken as $\gamma_{m,average}$, whose values are shown in (d) for a scan of 15×15 points or 225 CBED patterns. Here each color represents a different CBED pattern, whereas similar CBED patterns are shown in the same color.

The SCBED experiments were carried out using a JEOL 2010F FEG TEM operated at 200kV with a convergent beam of 2.6nm in FWHM (full-width half-maximum). Energy-filtering (EF), which improves the contrast of CBED patterns, was performed using a Gatan imaging filter (GIF). EF-SCBED was performed by scanning the focused electron probe over a selected area on a $15 \times$

15 grid, step size of 2nm, and through a post-column GIF energy window of 10eV. The shift and tilt of diffraction patterns during beam scanning were minimized and calibrated using a silicon single crystal (38). Following the procedures described in (35), the symmetry of PZN-8%PT was determined as monoclinic Pm, which agrees with the X-ray diffraction result (10).

4.3. Results

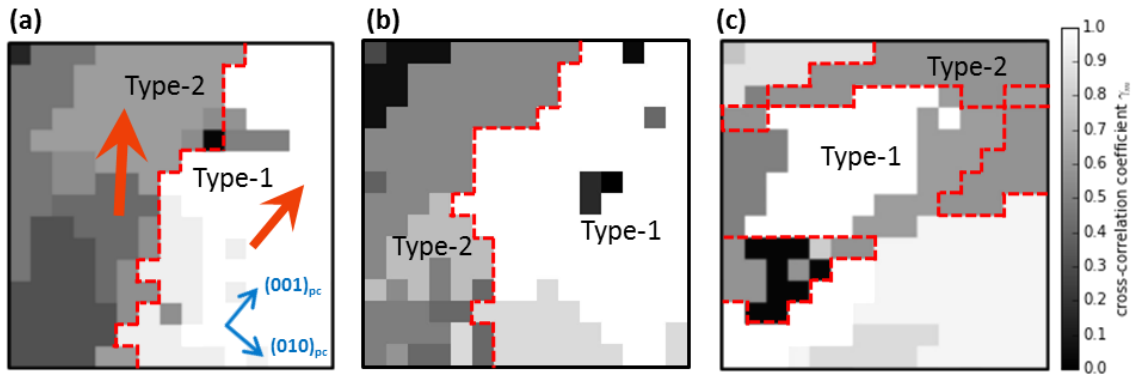


Figure 4.2. Distribution of two nanodomains using SCBED. (a), (b) and (c) map out the $\gamma_{m,average}$ variations across two types of domains. The red dashed line indicates the domain boundary. The orange arrows indicate the projected polarization directions for each type of domain.

Nanodomains are observed using EF-SCBED. Symmetry variations across these domains in three EF-SCBED datasets from three different sample areas are shown in Figs. 2(a), (b), and (c).

The scan consists of 15 by 15 points, with a step size of 2 nm. The $\gamma_{m,average}$ of the representative CBED patterns in each region are shown in greyscale. We identified type-1 and type-2 nanodomains with different mirror symmetry. The boundaries between these two domains are indicated as dashed lines in the figures.

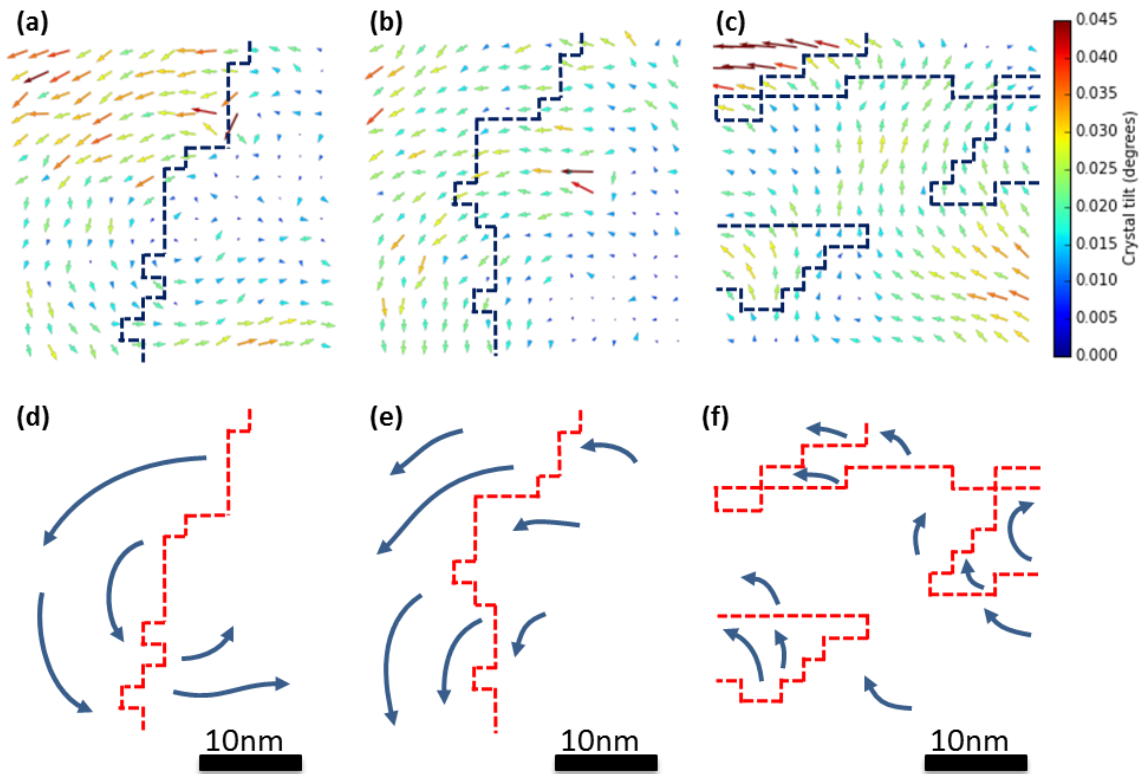


Figure 4.3. Maps of distribution of two nanodomains and lattice rotation vortices. Figs. (a), (b), and (c) show the crystal rotation at each pixel, superimposed with the domain walls indicated by the blue dashed lines. Figs. (d), (e), and (f) illustrates how the crystal rotates across the domain boundaries schematically.

We noticed that the center-of-mass of the intensity distribution within the BF disc of each pattern in the EF-SCBED dataset is not always located at the exact center. This observation could have two possible explanations: microscope optics and local crystal tilting. First, the hysteresis in the scanning coils or the lens in the microscope could lead to imperfect optical alignment while scanning the beam, which results in an effective beam-tilt and a consequent intensity redistribution in the BF disc. Second, if the crystal is not oriented on the exact zone axis, this small angular deviation could also lead to an intensity redistribution in the BF disc. This is shown schematically in Figs. 1(b) and 1(c). If small bending or buckling exists during specimen preparation, the intensity redistribution in the BF disc would mainly be shifting in a way consistent with bending. We excluded the effects of microscope optics by performing EF-SCBED on a Si single crystal. This measurement defines the maximum electron beam tilt and the lattice rotation measurement precision at ± 0.012 degrees. In an effort to quantify how much the crystal is deviated from the exact zone axis, we calculated the displacements (in pixels) of the center-of-mass of each BF disc and converted these displacements into crystal rotations (in degrees).

By measuring the shift in the BF disc of a CBED pattern using this method, we determined the rotation of the crystal and represented this rotation as a vector over nanometer-sized sample regions. The vector at each data point indicates the crystal rotation averaged over a volume of $\sim 280\text{nm}^3$. Figs. 3(a), (b), and (c) show the crystal rotation map derived from the same EF-SCBED datasets as Figs. 2(a), (b), and (c), respectively. Figure 3(a) shows a vortex-like pattern with the

vortex center near the domain boundary, and a radius of curvature of $\sim 7\text{nm}$ calculated from the discrete points. On the other hand, the vortex feature is not as distinct in Figs. 3(b) and (c). The continuous crystal rotation is shown schematically in Figs. 3(d), (e), and (f).

The type-1 and type-2 domains identified in Fig. 2 are associated with two distinguishable CBED patterns that were observed along the $[100]_C$ incident direction (Figs. 4(a) and 4(b)). Figs. 2(a), (b), and (c) show the symmetry maps where these two patterns were detected. The highest γ_m values of type-1 and type-2 patterns are detected along two different directions (A and B) as shown in Figs. 4(a) and 4(b). The A and B directions are rotated by 45° along the $[100]_C$ zone axis. The corresponding simulated patterns for type-1 and type-2 domains are along monoclinic Pm zone axis $[100]_{Pm}$ and $[010]_{Pm}$, as shown in Figs. 4(c) and 4(d), respectively. In the Pm structure model, the polarization direction is $\vec{P}_S = [u, 0, v]_{Pm} = [3, 0, 4]_{Pm}$, which lies in the mirror plane of Pm symmetry [12]. Along the $[100]_{Pm}$ incident direction, the mirror plane is superimposed on $(001)/(00\bar{1})$ reflections, which is parallel to the A direction in Fig. 4(a). This mirror is not observed along the $[010]_{Pm}$ incident direction. The projection of the polarization lies approximately on the $(101)/(\bar{1}0\bar{1})$ reflections, which is parallel to the B direction in Fig. 4(b). The highest mirror symmetry in this case is detected along direction B in the simulated pattern (Fig. 4(d)) with $\gamma_{m, simulated} = 60\%$.

Quantification of mirror symmetry for Fig. 4(a) and (b) gives $\gamma_{m,A}^1 = 95\%$ and $\gamma_{m,A}^2 = 34\%$, respectively (The superscript indicates the domain type, and the subscript denotes the mirror

plane direction). This shows that the mirror plane of type-1 domains is along the A direction. For the type-2 domains, a good match is obtained with $[010]_{Pm}$. The γ_m value along the B direction of the recorded patterns roughly agrees with the simulated value, with $\gamma_{m,experimental} = 54\%$.

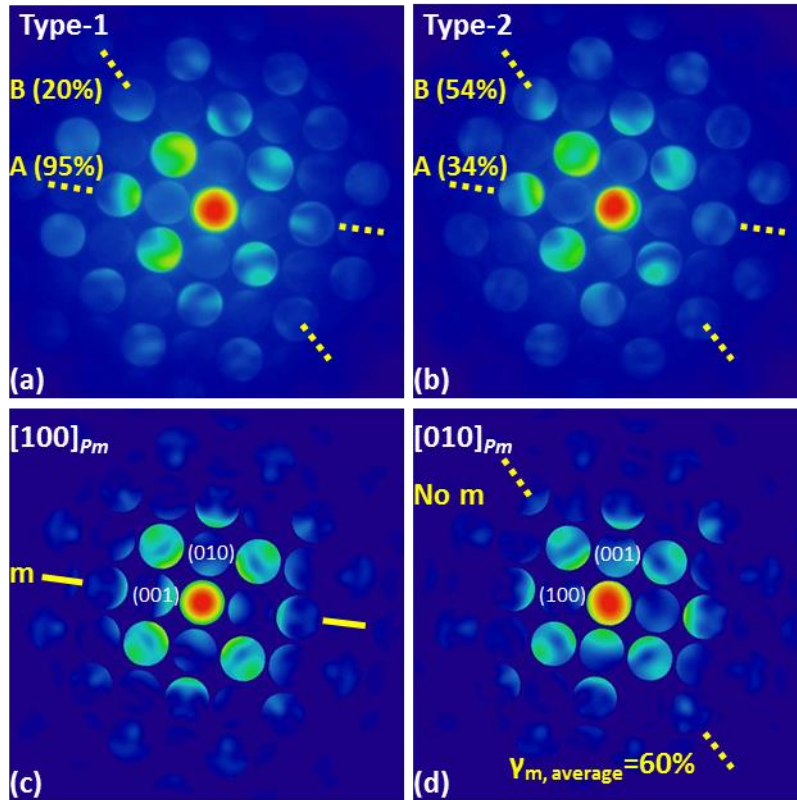


Figure 4.4. Experimental and simulated CBED patterns along various zone axes. The mirror plane in the (a) type-1 and (b) type-2 domains is rotated by 45° . Figs. (c) & (d) show simulated patterns of $M_c(Pm)$ using the Bloch wave method and corresponding to the experimental (a) & (b) patterns, respectively. The indexing is based on simulated diffraction patterns.

Based on the best matching structural model of Pm , the orientation relationship between the type-1 and 2 nanodomains with respect to the pseudocubic axes is shown schematically in Figure 5. For type-1 domains, which belong to the $[100]_{Pm}$ zone axis, the monoclinic axes of a_{Pm} and b_{Pm} are along $[100]_{PC}$ and $[010]_{PC}$, respectively. The c_{Pm} is slightly deviated away from the $[001]_{PC}$ direction with an angle $(90^\circ - \beta)$ in the $a_{Pm} - c_{Pm}$ plane. Type-2 domains belong to the $[010]_{Pm}$ zone axis, for which the monoclinic axes of a_{Pm} and b_{Pm} are rotated by 90° with respect to the cubic c-axis. If converting the two polarization directions $[3,0,4]_{Pm}$ and $[0,3,4]_{Pm}$ from fractional coordinates into Cartesian coordinates, the polarization directions in Cartesian coordinates would be $[3.03, 0.02, 4.05]$ and $[0.02, 3.01, 4.05]$, respectively. The angle between the two vectors is 50° . The presence of 50° polarization domains is also evidence which excludes the tetragonal (T)- or rhombohedral (R)-symmetries, since this type of domain is only permitted in crystals with orthorhombic or lower symmetries (27, 28). Bokov & Ye considered mechanically permissible domain configurations with monoclinic Pm symmetry. We observed regions with high symmetry, which implies no overlapping of 1/2 type domains in the thickness direction. However, we cannot exclude the overlapping of 2/4 domains in high symmetry region (27).

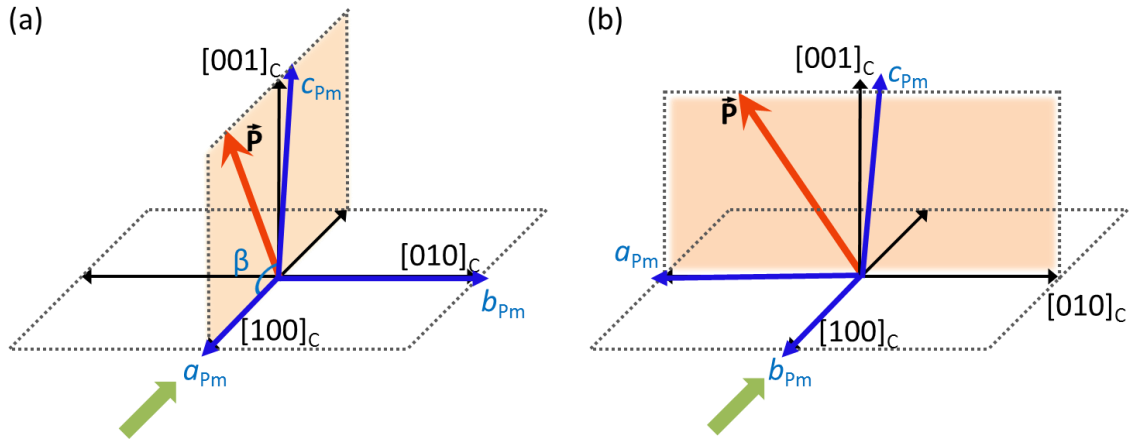


Figure 4.5. Orientation relationship between two nanodomains with respect to the pseudocubic axes. Figs. (a) and (b) correspond to type-1 and type-2 domains, respectively.

4.4. Discussion

Vortices form in ferroelectric crystals by two different mechanisms. Figure 6 (a) shows flux-closure domain patterns associated with continuous dipole rotations have been reported in ferroelectric thin films (21-24, 39) or ferroelectric nanodots (40-42). These patterns involve continuous dipole rotations near the vertices of triangular or quadrantal domain boundaries. By reducing the thickness of the thin film, ferroelectric dipole vortex-antivortex pairs can be stabilized (24), as shown in Fig. 6(b). The continuous rotation of the dipoles in vortex structures can also result from depolarizing fields, which are created by incompletely compensated charges at the surfaces and interfaces (Fig. 6(c)). Experimental evidence for a continuous rotation of the dipoles

was reported by Jia et al. (20, 21) in $\text{Pb}(\text{Zr},\text{Ti})\text{O}_3$ at the 180° domain walls. The organization of dipoles in vortex structures reduces depolarizing fields.

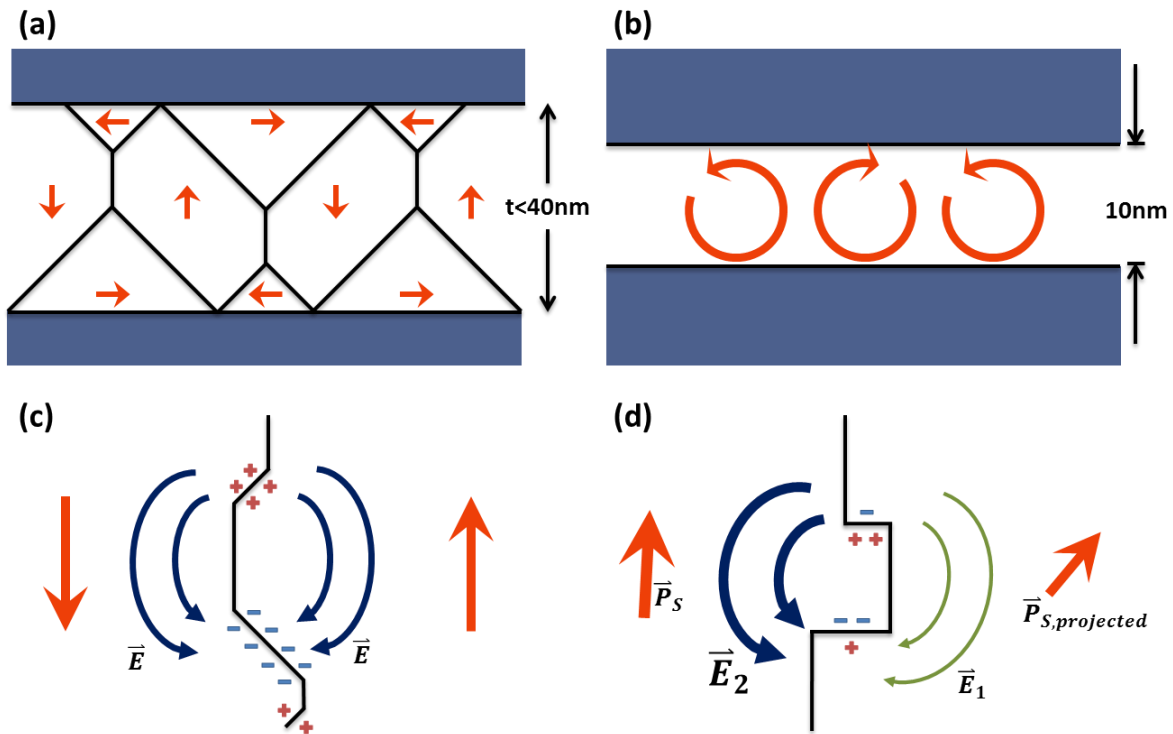


Figure 4.6. Schematic cartoon of various types of domain configurations, polarization orientation, and charge discontinuity. The reported (a) flux-closure quadrants, (b) dipole vortex-antivortex pairs, (c) 180° charged domain wall, and (d) our observation of 50° monoclinic charged domain wall. E_1 and E_2 represent the inhomogeneous electric field in type-1 and type-2 domains, respectively.

The rotation we observed is part of the lattice deformation matrix with displacement vector $u(\vec{r})$, defined by rigid body rotation tensor $\tilde{w}_{ij} = 1/2 (e_{ij} - e_{ji})$, where the strain tensor is $\varepsilon_{ij} = 1/2 (e_{ij} + e_{ji})$ and the quantity $e_{ij} = \frac{\partial u_i}{\partial x_j}$. For relaxor ferroelectric crystals with monoclinic symmetry, disinclination exists between two domains with an angular mismatch determined by unit cell parameters (27, 43). Strain accompanies the polarization rotation due to the strong electromechanical coupling (15, 16, 25). We speculate that the crystal rotation vortex can be a result of accommodating disinclination strain and charge discontinuity. First, the disinclination strain can be estimated by calculating Lagrangian finite strain tensors (44). Lattice parameters of two neighboring monoclinic Pm unit cells, distorted along two directions as depicted in Figure 5, are input parameters for calculating the strain tensors. The maximum strain at the domain wall is 1.3%, which is comparable to the 1.5% strain at the vertex core of rhombohedral BiFeO_3 (23).

Second, the depolarizing fields and effects on local dipoles can be simplified by considering the polarization of adjacent domains since $\vec{\nabla} \cdot \vec{P} = \rho_b$, where ρ_b is the bound charge density, and $\vec{\tau} = \vec{P} \times \vec{E}$, which is the torque acting on the dipoles by the depolarization field. At 180° charged DWs, the depolarization fields induced by bound charge are symmetrical and the forces on the dipoles are opposite on the two sides of the DWs, which creates a flux-closure vortex. However, this symmetry is broken in the case of a slightly charged monoclinic 50° DW, as shown in Fig. 6(d). The magnitude of inhomogeneous electric fields, E_1 and E_2 in type-1 and type-2 domains, respectively, are different due to strong dielectric anisotropy of the crystal (25). This torque is also

strongest when \vec{P} is normal to \vec{E} , and this torque is weak in the type-1 domain because its \vec{P} is pointing out of plane. This is consistent with our observation shown in Figs. 3(a) and 3(b), which the average magnitude of lattice rotation in type-2 domains is larger than that of in type-1 domains.

The above observation raises important questions about the roles of the lattice rotation vortex in domain switching in ferroelectric systems. Previously, first-principles calculations have predicted an intermediate state having a coexisting toroidal moment and out-of-plane-polarization in ferroelectric nanoparticles (45, 46). The occurrence of lattice rotation vortices at the ferroelectric domain walls suggests the interaction between 2D and 1D topological defects. An analogy can be made with the presence of magnetic vortices, known as skyrmions. The interplay between spin, orbital, charge, and strain degrees of freedom associated with skyrmions suggests a complex landscape of topological defects in ferroelectrics that may be explored for new applications and functionalities.

4.5. Conclusions

In conclusion, we observed local crystal rotation vortex at the 50° monoclinic domain boundary. The fractional crystal rotation vortex is attributed to depolarization fields due to charge discontinuity across the domain walls and their forces on local dipoles.

4.6. References

1. J. Seidel *et al.*, Conduction at domain walls in oxide multiferroics. *Nat Mater* **8**, 229 (Mar, 2009).
2. J. Guyonnet, I. Gaponenko, S. Gariglio, P. Paruch, Conduction at Domain Walls in Insulating $\text{Pb}(\text{Zr}_{0.2}\text{Ti}_{0.8})\text{O}_3$ Thin Films. *Adv Mater* **23**, 5377 (Dec 1, 2011).
3. G. Catalan, J. Seidel, R. Ramesh, J. F. Scott, Domain wall nanoelectronics. *Rev Mod Phys* **84**, 119 (Feb 3, 2012).
4. W. F. Rao, Y. U. Wang, Domain wall broadening mechanism for domain size effect of enhanced piezoelectricity in crystallographically engineered ferroelectric single crystals. *Appl Phys Lett* **90**, (Jan 22, 2007).
5. A. E. Renault, H. Dammak, G. Calvarin, M. P. Thi, P. Gaucher, Domain structures in monoclinic $\text{Pb}[(\text{Zn}_{1/3}\text{Nb}_{2/3})(0.91)\text{Ti}-0.09]\text{O}_3$ poled single crystals. *Jpn J Appl Phys I* **41**, 3846 (Jun, 2002).
6. M. Abplanalp *et al.*, Scanning force microscopy of domain structures in $\text{Pb}(\text{Zn}_{1/3}\text{Nb}_{2/3})\text{O}_3$ -8% PbTiO_3 and $\text{Pb}(\text{Mg}_{1/3}\text{Nb}_{2/3})\text{O}_3$ -29% PbTiO_3 . *J Appl Phys* **91**, 3797 (Mar 15, 2002).
7. T. Asada, T. Shibata, Y. Koyama, Ferroelectric domain structures near the MPB in $(1-x)\text{Pb}(\text{Zn}_{1/3}\text{Nb}_{2/3})\text{O}_3$ - $x\text{PbTiO}_3$. *Ferroelectrics* **347**, 17 (2007).
8. D. E. Cox *et al.*, Universal phase diagram for high-piezoelectric perovskite systems. *Appl Phys Lett* **79**, 400 (Jul 16, 2001).
9. J. S. Forrester, E. H. Kisi, Monoclinic PZN-8% PT [$\text{Pb}(\text{Zn}_{0.3066}\text{Nb}_{0.6133}\text{Ti}_{0.08})\text{O}_3$] at 4 K. *Acta Crystallogr C* **63**, I115 (Dec, 2007).
10. J. M. Kiat *et al.*, Monoclinic structure of unpoled morphotropic high piezoelectric PMN-PT and PZN-PT compounds. *Phys Rev B* **65**, (Feb 1, 2002).
11. K. H. Kim, D. A. Payne, J. M. Zuo, Ion-beam induced domain structure in piezoelectric PMN-PT single crystal. *Appl Phys Lett* **97**, (Dec 27, 2010).
12. E. H. Kisi, J. S. Forrester, The phase transition sequence in the relaxor ferroelectric PZN-8% PT. *J Phys-Condens Mat* **20**, (Apr 23, 2008).
13. D. La-Orautapong *et al.*, Phase diagram of the relaxor ferroelectric $(1-x)\text{Pb}(\text{Zn}_{1/3}\text{Nb}_{2/3})\text{O}_3$ - $x\text{PbTiO}_3$. *Phys Rev B* **65**, (Apr 1, 2002).
14. J. K. Lee, J. Y. Yi, K. S. Hong, S. E. Park, J. Millan, Domain configuration and crystal structure of $\text{Pb}(\text{Zn}_{1/3}\text{Nb}_{2/3})\text{O}_3$ -5% PbTiO_3 crystals as a function of the electric-field direction. *J Appl Phys* **91**, 4474 (Apr 1, 2002).

15. B. Noheda *et al.*, Polarization rotation via a monoclinic phase in the piezoelectric 92% $\text{PbZn}_{1/3}\text{Nb}_{2/3}\text{O}_3$ -8% PbTiO_3 . *Phys Rev Lett* **86**, 3891 (Apr 23, 2001).
16. B. Noheda *et al.*, Electric-field-induced phase transitions in rhombohedral $\text{Pb}(\text{Zn}_{1/3}\text{Nb}_{2/3})(1-x)\text{Ti}_x\text{O}_3$. *Phys Rev B* **65**, (Jun 1, 2002).
17. K. Ohwada, K. Hirota, P. W. Rehrig, Y. Fujii, G. Shirane, Neutron diffraction study of field-cooling effects on the relaxor ferroelectric $\text{Pb}[(\text{Zn}_{1/3}\text{Nb}_{2/3})(0.92)\text{Ti}_{0.08}]\text{O}_3$. *Phys Rev B* **67**, (Mar 1, 2003).
18. K. Ohwada *et al.*, Neutron diffraction study of the irreversible R-M-A-M-C phase transition in single crystal $\text{Pb}[(\text{Zn}_{1/3}\text{Nb}_{2/3})(1-x)\text{Ti}_x]\text{O}_3$. *J Phys Soc Jpn* **70**, 2778 (Sep, 2001).
19. D. Lee *et al.*, Mixed Bloch-Neel-Ising character of 180 degrees ferroelectric domain walls (vol 80, 060102, 2009). *Phys Rev B* **80**, (Oct, 2009).
20. C. L. Jia *et al.*, Atomic-scale study of electric dipoles near charged and uncharged domain walls in ferroelectric films. *Nat Mater* **7**, 57 (Jan, 2008).
21. C. L. Jia, K. W. Urban, M. Alexe, D. Hesse, I. Vrejoiu, Direct Observation of Continuous Electric Dipole Rotation in Flux-Closure Domains in Ferroelectric $\text{Pb}(\text{Zr,Ti})\text{O}_3$. *Science* **331**, 1420 (Mar 18, 2011).
22. C. T. Nelson *et al.*, Spontaneous Vortex Nanodomain Arrays at Ferroelectric Heterointerfaces. *Nano Lett* **11**, 828 (Feb, 2011).
23. Y. L. Tang *et al.*, Observation of a periodic array of flux-closure quadrants in strained ferroelectric PbTiO_3 films. *Science* **348**, 547 (May 1, 2015).
24. A. K. Yadav *et al.*, Observation of polar vortices in oxide superlattices. *Nature* **530**, 198 (Feb 11, 2016).
25. S. E. Park, T. R. ShROUT, Ultrahigh strain and piezoelectric behavior in relaxor based ferroelectric single crystals. *J Appl Phys* **82**, 1804 (Aug 15, 1997).
26. R. Bertram, G. Reck, R. Uecker, Growth and correlation between composition and structure of $(1-x)\text{Pb}(\text{Zn}_{1/3}\text{Nb}_{2/3})\text{O}_3$ - $x\text{PbTiO}_3$ crystals near the morphotropic phase boundary. *J Cryst Growth* **253**, 212 (Jun, 2003).
27. A. A. Bokov, Z. G. Ye, Domain structure in the monoclinic Pm phase of $\text{Pb}(\text{Mg}_{1/3}\text{Nb}_{2/3})\text{O}_3$ - PbTiO_3 single crystals. *J Appl Phys* **95**, 6347 (Jun 1, 2004).
28. J. Sapriel, Domain-Wall Orientations in Ferroelastics. *Phys Rev B* **12**, 5128 (1975).
29. B. Houchmandzadeh, J. Lajzerowicz, E. Salje, Order Parameter Coupling and Chirality of Domain-Walls. *J Phys-Condens Mat* **3**, 5163 (Jul 8, 1991).

30. M. Schaffer, B. Schaffer, Q. Ramasse, Sample preparation for atomic-resolution STEM at low voltages by FIB. *Ultramicroscopy* **114**, 62 (Mar, 2012).
31. Y.-T. Shao, J.-M. Zuo, Fundamental Symmetry of Barium Titanate Single Crystal Determined Using Energy-Filtered Scanning Convergent Beam Electron Diffraction. *Microscopy and Microanalysis* **22**, 516 (2016/007/001, 2016).
32. B. F. Buxton, J. A. Eades, J. W. Steeds, G. M. Rackham, The Symmetry of Electron Diffraction Zone Axis Patterns. *Philosophical Transactions of the Royal Society of London. Series A, Mathematical and Physical Sciences* **281**, 171 (1976).
33. J. P. Morniroli, J. W. Steeds, Microdiffraction as a Tool for Crystal-Structure Identification and Determination. *Ultramicroscopy* **45**, 219 (Sep, 1992).
34. M. Tanaka, K. Tsuda, Convergent-beam electron diffraction. *J Electron Microsc* **60**, S245 (Aug, 2011).
35. K. H. Kim, D. A. Payne, J. M. Zuo, Symmetry of piezoelectric $(1-x)\text{Pb}(\text{Mg}_{1/3}\text{Nb}_{2/3})\text{O}_3-x\text{PbTiO}_3$ ($x=0.31$) single crystal at different length scales in the morphotropic phase boundary region. *Phys Rev B* **86**, 184113 (Nov 29, 2012).
36. K. H. Kim, D. A. Payne, J. M. Zuo, Determination of 60 degrees polarization nanodomains in a relaxor-based ferroelectric single crystal. *Appl Phys Lett* **107**, 162902 (Oct 19, 2015).
37. K. H. Kim, J. M. Zuo, Symmetry quantification and mapping using convergent beam electron diffraction. *Ultramicroscopy* **124**, 71 (Jan, 2013).
38. K. H. Kim, H. Xing, J. M. Zuo, P. Zhang, H. F. Wang, TEM based high resolution and low-dose scanning electron nanodiffraction technique for nanostructure imaging and analysis. *Micron* **71**, 39 (Apr, 2015).
39. N. Balke *et al.*, Enhanced electric conductivity at ferroelectric vortex cores in BiFeO_3 . *Nat Phys* **8**, 81 (Jan, 2012).
40. A. Gruverman *et al.*, Vortex ferroelectric domains. *J Phys-Condens Mat* **20**, (Aug 27, 2008).
41. M. J. Polking *et al.*, Ferroelectric order in individual nanometre-scale crystals. *Nat Mater* **11**, 700 (Aug, 2012).
42. A. Schilling *et al.*, Domains in Ferroelectric Nanodots. *Nano Lett* **9**, 3359 (Sep, 2009).
43. J. Privratska, Disorientation angle expressed in terms of lattice parameters. *Ferroelectrics* **291**, 197 (2003).
44. M. I. Aroyo *et al.*, Crystallography online: Bilbao Crystallographic Server. *Bulg Chem Commun* **43**, 183 (2011).

45. B. J. Rodriguez *et al.*, Vortex Polarization States in Nanoscale Ferroelectric Arrays. *Nano Lett* **9**, 1127 (Mar, 2009).
46. M. G. Stachiotti, M. Sepiarsky, Toroidal Ferroelectricity in PbTiO₃ Nanoparticles. *Phys Rev Lett* **106**, (Mar 29, 2011).

CHAPTER 5

DIRECT IMAGING OF DISTORTED LATTICE IN A HIGH ENTROPY ALLOY

High entropy alloys (HEAs) feature severely distorted lattices arising from atomic size mismatch that has become a focal point of research for the study of their unusual properties. Lattice distortions can be measured by electron imaging or by diffraction through the study of pair distribution functions (PDF). However, the PDF results so far have only found small distortions within a small atomic radius. Here, we present quantitative imaging results of lattice distortions and local symmetry breaking in a single phase HEA, $\text{Al}_{0.1}\text{CrFeCoNi}$. Results revealed two types of lattice distortions in $\text{Al}_{0.1}\text{CrFeCoNi}$. One features 10 ± 3 nm, disc-shaped, clusters having $\sim 7.1\%$ tensile displacements along $\langle 110 \rangle$ directions distributed throughout the specimen, and the other gives rise to local fluctuating strain within $\pm 1.3\%$, which is slow-varying over ~ 50 nm. Both results suggest the non-ideal solid solution nature of HEA. Furthermore, peak broadening with increasing diffraction orders is consistent with the paracrystal model having lattice distortion parameter of 2.12%. Our observation is made possible using scanning convergent beam electron diffraction, and the results here thus demonstrate a new powerful experimental approach toward quantitative study of multi-principal element systems.

5.1. Introduction

Crystals possessing distorted lattice are ubiquitous in nature and often associated with functional material properties. Examples include polarization nanodomains in ferroelectrics and solid solution alloys. A common scheme to these systems is that there exists a distinction between local crystal symmetry and the average, macroscopic symmetry imposed by fluctuations in the crystal lattice. Understanding their local structures is a prerequisite for further understanding of the material's properties, however, requires robust and quantitative methods for probing crystallography at the nanoscale (1, 2). High entropy alloys (HEAs) represent an exemplar of crystals with distorted lattices. They are made of five or more elements in equal or near-equal molar percentage, and often forms a single solid solution phase (3-5). HEAs, including the more broadly defined multi-principal element alloys (MPEAs), have attracted much research attention for the discovery of outstanding mechanical properties at extreme temperatures and exceptional structural stability under irradiation (6-9). The lattice distortion is expected to be more severe than in dilute solid solution alloys, contributing to excess entropy, and impede dislocation movements leading to pronounced solid solution strengthening (10-14). Consequently, the severe lattice distortion effect is one of the core effects for describing MPEAs (15).

However, the characterization of lattice distortions in HEAs present a significant challenge to the materials research community (11-14, 16). The reported X-ray and neutron diffraction studies generally demonstrate sharp Bragg peaks (5, 17, 18), although the decrease in peak intensities may

result from effects such as lattice distortion, thermal vibration, and crystallographic texture (10, 12, 13, 19, 20). The lattice distortions in high-entropy alloys were further investigated based on pair distribution functions obtained from synchrotron X-ray or neutron scattering. However, the results of such analyses have provided contradictory pictures about lattice distortions in MPEAs. For example, a large deviation of the local structure from the average lattice was found in the body-centered cubic (bcc) ZrNbHf and Al_{1.3}CoCrCuFeNi (21, 22), whereas a negligible deviation was observed in the face-centered cubic (fcc) CrFeCoNi and CrMnFeCoNi (23, 24).

Here, we describe a systematic study of lattice distortion quantification in fcc Al_{0.1}CrFeCoNi alloy using a new electron imaging technique, namely, scanning convergent beam electron diffraction (SCBED). Unlike scanning transmission electron microscopy (STEM) which uses scattered electron intensity for imaging, images or maps can be constructed in SCBED based on an analysis of information recorded in the diffraction patterns. We employed three types of analyses here: 1) measurement of the d-spacing for imaging nanoscale strain variations, 2) quantification of the peak broadening with increasing diffraction orders for lattice distortion mapping, and 3) a determination of local symmetry using CBED. The combination of these measurements identified two types of lattice distortions in Al_{0.1}CrFeCoNi: one features 10±3 nm, disc-shaped, clusters having ~7.1% tensile displacements along <110> directions distributed throughout the specimen, and the other gives rise to local fluctuating strain within ±1.3%, which

is slow-varying over ~50 nm. Furthermore, the peak broadening with increasing diffraction orders revealed $\text{Al}_{0.1}\text{CrFeCoNi}$ as paracrystalline with lattice distortion parameter g of 2.12%.

5.2. Experimental methods

Polycrystalline $\text{Al}_{0.1}\text{CrFeCoNi}$ MPEA was prepared by vacuum induction melting and casting (Sophisticated Alloys Inc., Butler, PA). The as-cast samples were hot isostatic pressed at $1,100^\circ\text{C}$ for 1h under a 207MPa ultra-high-purity argon pressure to reduce porosity, which resulted large grain sizes ($\sim 10^2 \mu\text{m}$). The composition and chemical homogeneity were checked by atom probe tomography analysis (25). Thin TEM specimen were carefully prepared along [001] axis using focused ion beam (FIB) with the method described previously (26). The SCBED experiments were carried out using a Themis Z STEM (Thermo Fisher Scientific) operated at 300kV, and a JEOL 2200FS FEG TEM with an in-column Omega energy filter and operated at 200kV for energy-filtered CBED. SCBED works by rastering the focused electron probe over a selected area, and recording the electron diffraction pattern over each probe position using a pixelated detector (Fig. 1a, also see ref (27, 28)). Two types of diffraction patterns were recorded, one uses a semi-convergence angle of 1.4 mrad and probe size of 1.7 nm in FWHM (full-width at half-maximum) for a spot-like diffraction pattern (Fig. 1b) and another uses a semi-convergence angle of 5.5 mrad and probe size of 0.8 nm in FWHM for CBED (Fig. 1c). The spot-like diffraction patterns was used for strain analysis following the procedures described in ref (29), while the CBED pattern was quantified for its mirror and rotational symmetry using a correlation based

analysis (30, 31). Local lattice distortion can be identified by the breakdown of symmetry in CBED patterns deviating from perfect $4mm$ symmetry for a fcc crystal projected along [001] direction. With the aid of CBED simulations, the specimen thickness is determined as $\sim 186\text{nm}$.

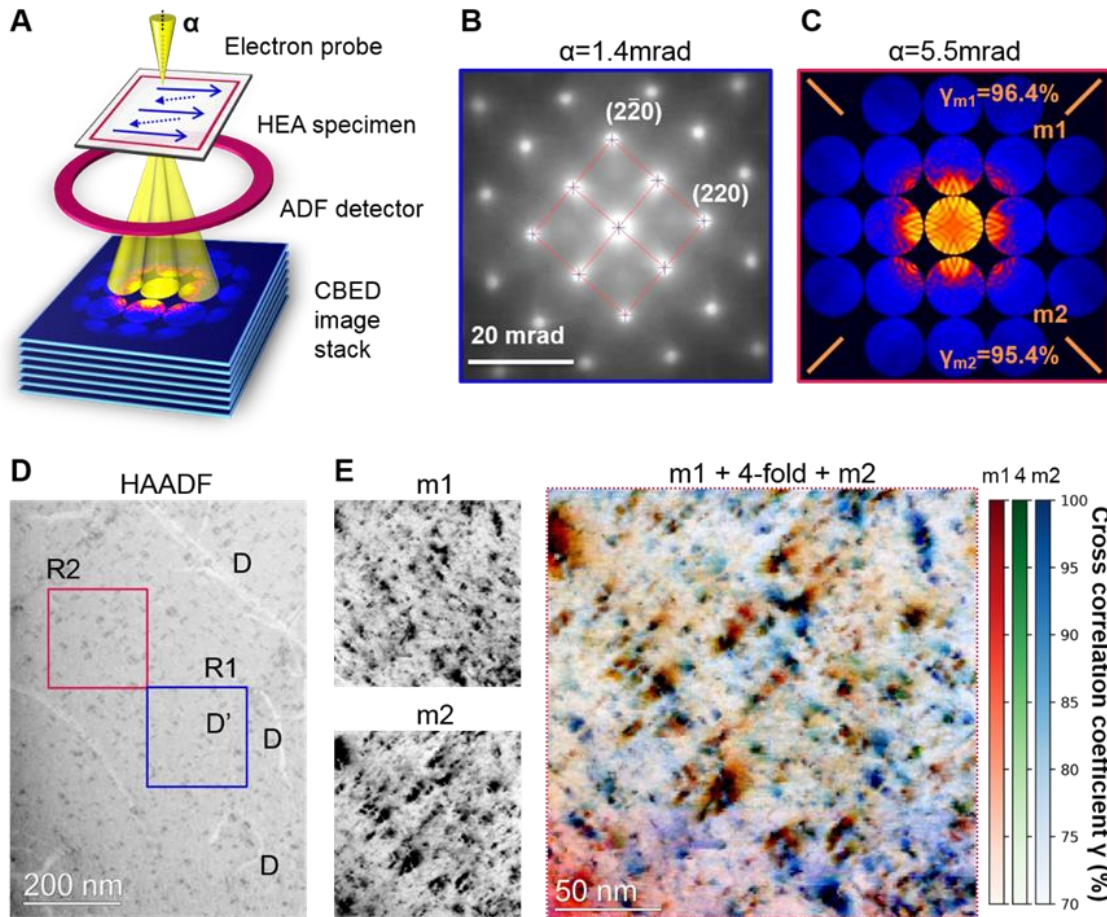


Figure 5.1. SCBED imaging. (a) Schematic of the SCBED technique with various probe semi-convergence angle α . As the convergent electron probe rasters over a region of interest, a CBED pattern is recorded at each probe position. Figure (b) shows a representative CBED pattern with α of 1.4mrad, strain can be obtained by measuring relative shifts in disk positions. (c) Representative experimental CBED pattern with α of 5.5mrad, having highest symmetry of $\gamma_4=95.9\%$, $\gamma_{m1}=96.4\%$, $\gamma_{m2}=95.4\%$. (d) HAADF image acquired with illumination semi-convergence angle α of 5.5mrad, inner collection angle of 60 mrad. R1 and R2 indicate the regions of the SCBED experiments performed with convergence angles in (B and C), respectively. D and D' indicate two types of defects, dislocation and “coffee bean”, respectively. (E) Overlay of symmetry maps obtained by quantifying symmetry in CBED patterns for 4-fold rotation (green), and along two different mirror plane directions, m1 (red) and m2 (blue).

5.3. Results

Two types of symmetry breaking are observed, “coffee bean” contrast and symmetry fluctuations. By quantifying each of the 40,000 CBED patterns taken from region R2 (Fig. 1D), symmetry maps can be reconstructed from the SCBED dataset (Figs. 1C, 1E, and S1) for 4-fold rotation (green), and along two mirror plane directions m_1 (red) and m_2 (blue). Symmetry in each CBED pattern reflects the distorted lattice averaged over the local volume illuminated by the electron beam. In column approximation, the illuminated volume of crystal is roughly the product of probe diameter squared and specimen thickness of 186nm. Small probes are hence more sensitive to crystal symmetry breaking (fig. S3).

The defects D' showing “coffee bean” contrast (Figs. 1D and 2A) feature anisotropic symmetry breaking along $\langle 110 \rangle$ directions, which is different from the diffraction contrast TEM micrographs of coherent spherical inclusions in conventional solid solution alloys (32, 33). If the inclusion were spherical, the 4-fold rotational symmetry would only be preserved when the electron beam be positioned at the very core of inclusion (34, 35). Moreover, the shape of the symmetry breaking are found in close resemblance of the projected normal stress field around an oblate spheroid calculated from the Eshelby's model for ellipsoid inclusions (Fig. 2B, also see refs. (36-40)). The tensile displacement fields from the inclusion can be verified by looking into individual CBED patterns. The CBED patterns in this region (Fig. 2A) can roughly be grouped into 3 categories: core, left-hand-side (LHS) and right-hand-side (RHS). For example, the

experimental CBED pattern taken from RHS of the cluster (Fig. 2C) shows a higher mirror symmetry along m_2 but a broken mirror symmetry along m_1 , with $\gamma_{m_2}=92.5\%$ and $\gamma_{m_1}=65.2\%$, respectively. CBED patterns of imperfect crystals having displacements were simulated using the Bloch-wave scattering matrix method (41-43). Along the electron beam path, the displacement fields was approximated as a column with a displaced block of 10nm (Fig. 2B). Figure 2D shows a simulated CBED pattern of a block located at 10nm from the surface and displaced $\sim 7.1\%$ along $(2\bar{2}0)$ from the column, which corresponds to the experimental CBED pattern (Fig. 2C). Within the 200nm x 200nm SCBED dataset (Region R2, Fig. 1D), 22 disc-shaped clusters were identified and found to be 10 ± 3 nm in diameter, all having tensile displacements from the cluster along one of the $\langle 110 \rangle$ directions.

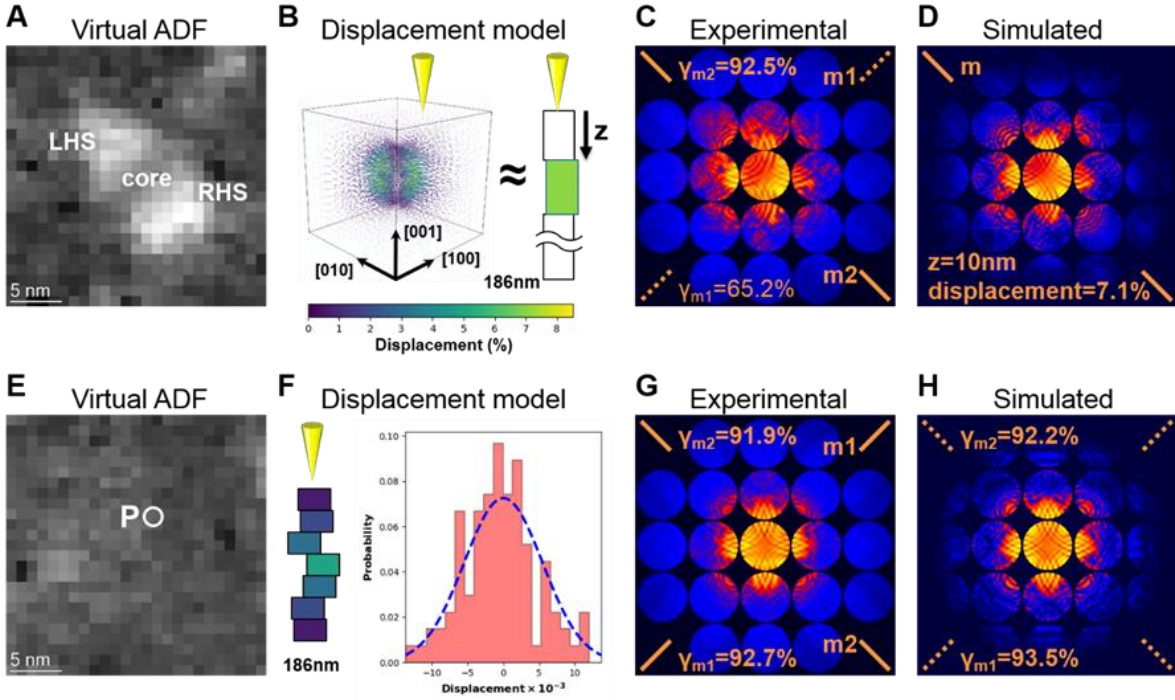


Figure 5.2. Displacement fields in $Al_{0.1}CrFeCoNi$ HEA provided by experimental and simulated CBED patterns. Virtual ADF images of (A) selected and (E) without “coffee bean” contrast. CBED patterns from imperfect crystals were simulated using the Bloch-wave scattering-matrix method. The lattice displacements along the electron beam path were approximated as a column having (B) a displaced block of 10nm, and (F) blocks of few nanometers with displacements following the Gaussian distribution. (B) The displacement fields from Eshelby’s theory of ellipsoidal inclusions calculated using finite element analysis method. Figures (D and H) show simulated CBED patterns corresponding to the experimental (C and G) patterns, respectively.

Symmetry fluctuations in regions free of inclusions (Figs. 1E and 2E) can be attributed to variations in atomic displacement. To estimate the amount of displacement fluctuations in HEAs, we performed a series of CBED simulations by dividing the 186-nm-thick crystal column into nm-sized blocks, each block having displacements (u_x, u_y, u_z) which follows the Gaussian distribution

with zero mean displacement (Fig. 2E). 625 CBED patterns were simulated and quantified for each combination of block size and standard deviation of displacement, ranging from 1-10nm and 0.35-0.65%, respectively. By comparing the distribution of 4-fold rotational symmetry of 4,375 experimental CBED patterns from regions free of coffee bean contrast with simulated CBED patterns, local symmetry fluctuation can be estimated by 3-8nm blocks having displacements following the Gaussian distribution with 0.55% standard deviation displacement (Fig. 5.3). For example, Fig. 2D shows a simulated CBED pattern of 5nm blocks having 0.55% standard deviation of displacements, which corresponds to the experimental CBED pattern shown in Fig. 2C.

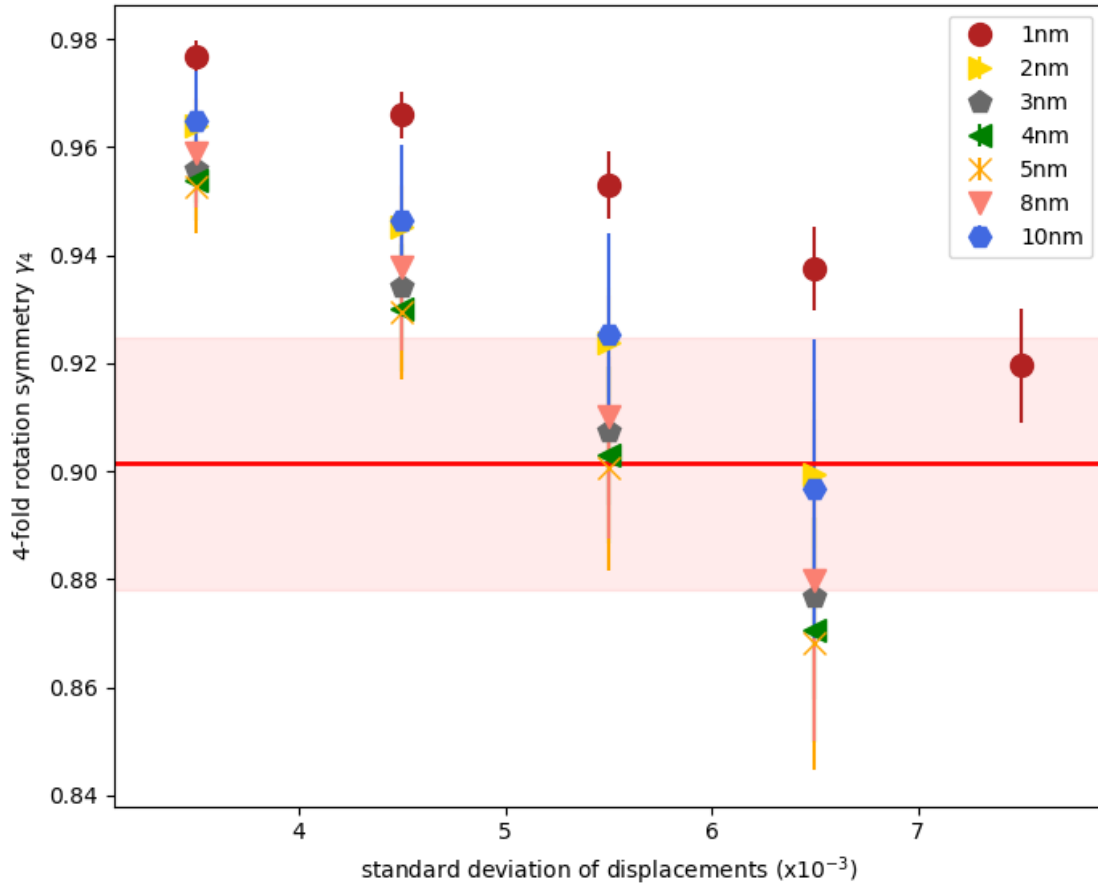


Figure 5.3. CBED symmetry fluctuations versus nm-sized blocks having displacements in $Al_{0.1}CrFeCoNi$ HEA. CBED patterns from imperfect crystals were simulated using the Bloch-wave scattering-matrix method. The lattice displacements along the electron beam path were approximated as a column having blocks of few nanometers with displacements following the Gaussian distribution. Each data point corresponds to the distribution of 4-fold rotational symmetry from 625 simulated CBED patterns. The red horizontal line (band) corresponds to the mean (standard deviation) of 4-fold rotational symmetry of 4375 experimental CBED patterns from regions without “coffee bean” contrast.

The strain maps along (220) and $(\bar{2}\bar{2}0)$ directions (Figs. 4b & 4c, respectively) are obtained by measuring the relative shifts in disk positions at region R1 (Fig. 1d). The precision of strain is

$\pm 0.13\%$, which is determined by the SCBED strain measurement on a Si [110] single crystal. The disc-shaped inclusions correspond to localized region with compressive strain in Fig. 2, B and C. In addition, no extra reflections were found from the SCBED dataset with semi-convergence angle α of 1.4mrad, which suggests the absence of ordering of inclusions (Fig. 1B). The line profiles (Line 1 and Line 2 in Fig. 4, C and D) taken from the strain maps show the strain to be slow-varying over $\sim 50\text{nm}$ while having fluctuations within $\pm 1.3\%$ in the range of a few nanometers.

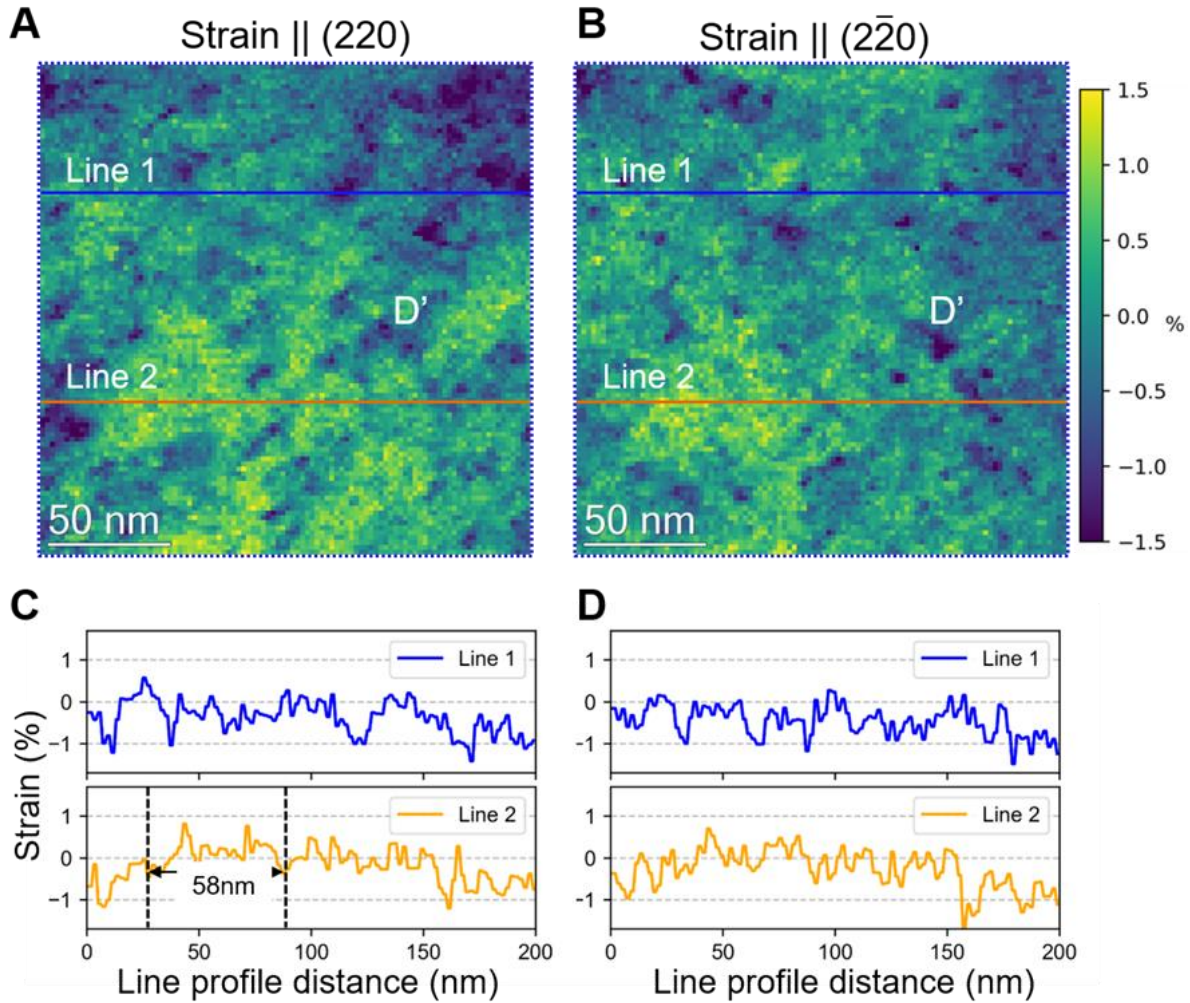


Figure 5.4. Local strain fluctuations in $Al_{0.1}CrFeCoNi$ MPEA. Strain maps of region R2 along the (A) (220) and (B) $(2\bar{2}0)$ directions were obtained by measuring relative shifts in disk positions. (C and D) Line profiles drawn from (A and B), respectively.

We noticed the peak broadening with increasing diffraction orders in the SCBED dataset (Fig. 5A). This observation could have two possible explanations: zone-axis effects and local lattice distortions. Along the zone axis orientation, all zero-order Laue zone (ZOLZ) reflections except (000) do not satisfy the Bragg conditions, which could lead to diffraction peak broadening resulting from the intersection of Ewald sphere and reciprocal lattice rods. In addition, the

inelastic, forward-scattered electrons would result in Ewald spheres with multiple radii and a consequent peak broadening. Second, the crystal lattices possessing nonuniform strain would also give rise to peak broadening in the diffraction patterns. For example, the paracrystal model, or lattice distortions of the second kind, suggests a quadratic increase in the integral breadths δb of successive diffracted orders (h) (44, 45). We excluded the peak broadening from the crystallites size effect since the region for performing SCBED is a single grain. The zone-axis effect was considered by performing SCBED on a Si single crystal along [110] zone axis, which defines the peak integral breadth measurement precision at $\pm 0.00315 \text{ \AA}^{-1}$. By fitting the (200), (400), and (600) reflections from 10,000 CBED patterns taken from region R1 (Fig. 1D), lattice distortion parameter map can be reconstructed from the SCBED dataset (Fig. 5C). The mean lattice distortion parameter g in this region was determined as 2.12% (Fig. 5B).

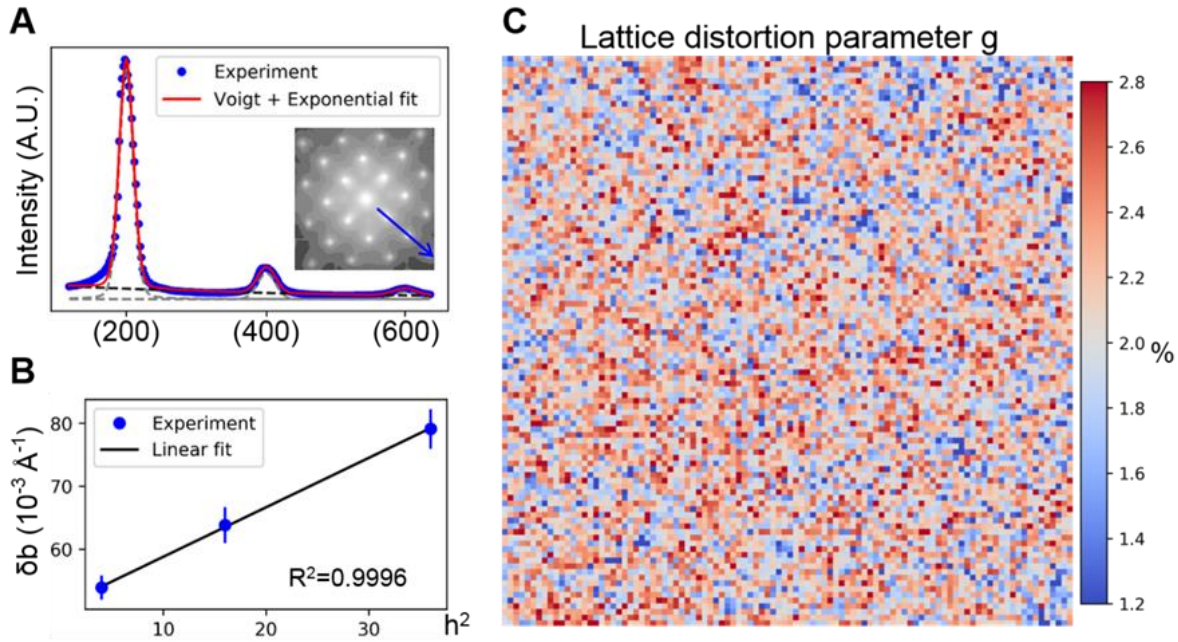


Figure 5.5. Lattice distortions of paracrystalline $Al_{0.1}CrFeCoNi$ HEA. (A) Example fit of an intensity profile with three orders of (200) reflections drawn from the averaged CBED pattern with $\alpha=1.4$ mrad. (B) Diagram of integral width δb versus square of reflection orders h^2 . Lattice distortion parameter g of 2.12% can be derived from the slope of the δb - h^2 diagram. The error bars represent the standard deviation of 400 measurements on standard Si along [110] zone axis. (C) Lattice distortion parameter map of region R2 obtained by measuring the peak broadening with increasing reflection orders.

The observed symmetry breaking in both transmitted and diffracted disks of experimental CBED patterns could have two possible explanations: microscope optics and local crystal imperfections. First, we exclude the effects of microscope optics by performing SCBED on a Si single crystal, which defines a figure of merit of $\gamma_4 \geq 95\%$ for a symmetrical CBED pattern. Secondly, symmetry in each CBED pattern reflects the imperfect lattice averaged over the local

volume illuminated by the electron beam. In column approximation, the illuminated volume of crystal is roughly the product of probe diameter squared and specimen thickness of 186nm. By performing SCBED using various probe sizes of 50nm, 10nm, 5nm, 1nm, the symmetry breaking in CBED patterns can be detected as the electron probe $\leq 10\text{nm}$ (Fig. 6), or illuminated volume $\leq 18,600\text{nm}^3$, which demonstrates the sensitivity of the SCBED technique.

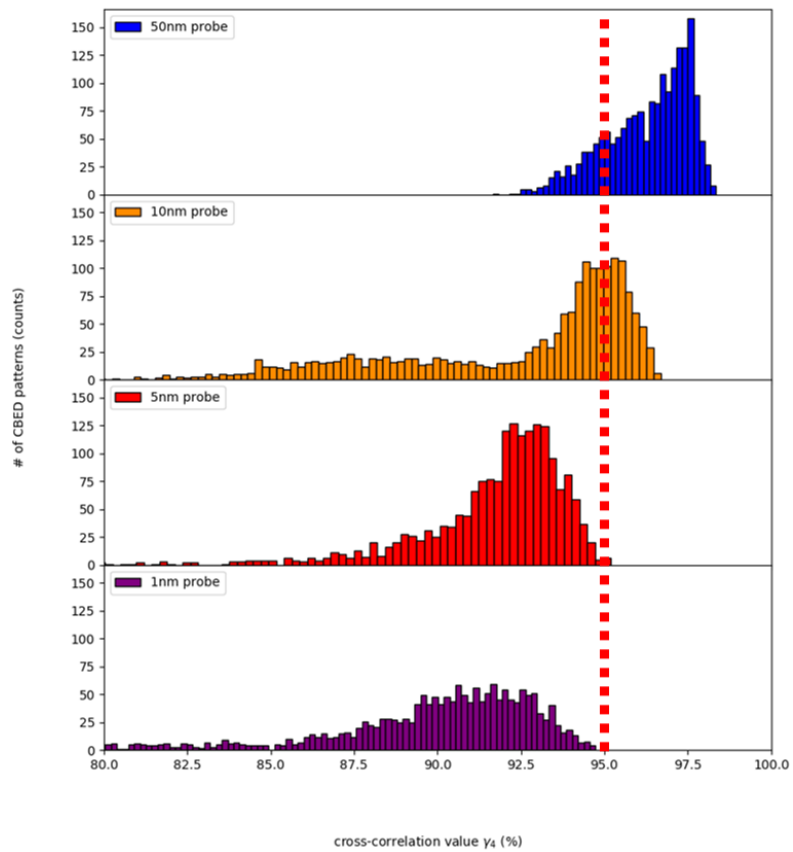


Figure 5.6. Probe size dependent symmetry in $Al_{0.1}CrFeCoNi$ HEA. For each probe size, more than 1875 CBED patterns were quantified with 4-fold rotational symmetry. The red dashed line was drawn along $\gamma_4=95\%$, indicating a figure of merit for symmetrical patterns.

5.4. Discussion

The distorted lattice in $\text{Al}_{0.1}\text{CrFeCoNi}$ HEA can be understood from comprehensive SCBED results of symmetry, strain, and lattice distortion parameters. First, the symmetry maps show there being regions with and without coherent, disordered inclusions (Figs. 1-2). The inclusions with tensile displacements can be assumed as Al-rich, since Al has the largest atomic size mismatch. However, no obvious elemental segregation were found in $\text{K}\text{-}\alpha$ peak ratio maps obtained from EDS-SI performed at same region as SCBED [Fig. 7]. This may be explained by the 7nm cluster embedded in a 186nm-thick MPEA specimen being well below the detection limits of our EDS system (46).

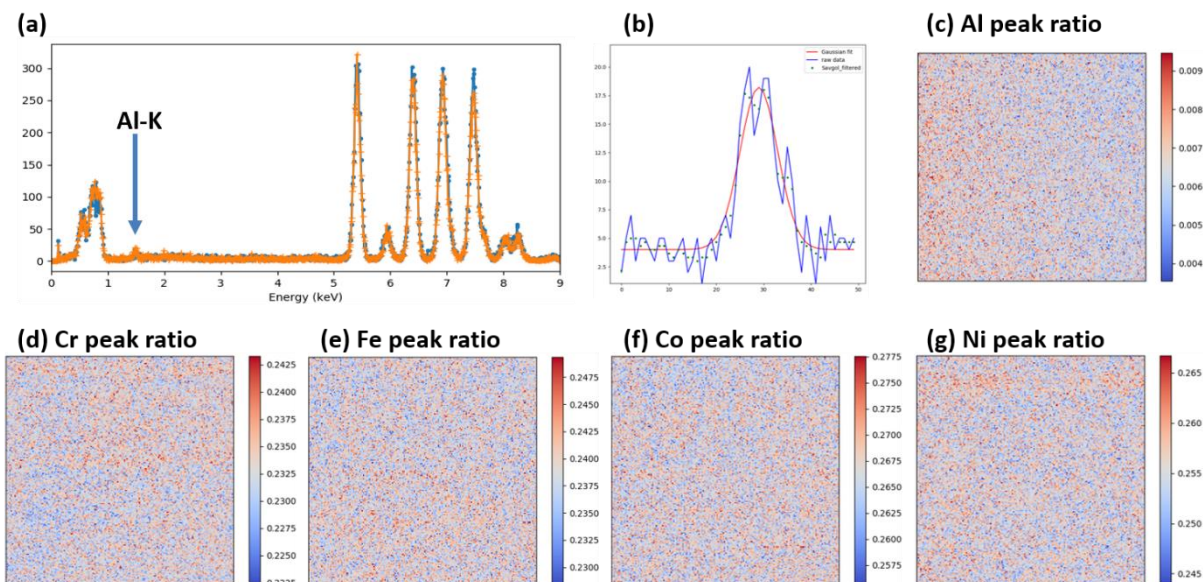


Figure 5.7. Energy dispersive X-ray spectrum images of $Al_{0.1}CrFeCoNi$ HEA. The EDS-spectrum image, 180×180 with step sizes of $1nm$, was acquired about the same region as for SCBED, with specimen tilted $\sim 6^\circ$ away from $[001]$ zone axis. Each spectrum was acquired for $1s$, spanning the total acquisition time of $\sim 11hrs$. Every $K\text{-}\alpha$ peak signal for each element was first smoothed with Savitzky–Golay filter, fitted with a Gaussian peak to obtain the peak height, then normalized with respect to total $K\text{-}\alpha$ peak heights in each spectrum. Each image were displayed with limits between ± 3 times of standard deviation about the average.

Second, the strain maps correspond to the local d-spacing averaged over all unit cells being illuminated by the electron beam, as shown in Figs. 3(a)-3(b). In the column approximation, the volume being illuminated is roughly the product of probe diameter squared and specimen thickness. Third, the lattice distortion parameter reflects the variance of the d-spacing of the column (Fig. 4c). In the paracrystal model, the lattice distortion parameter g was defined as $g^2 = \frac{\langle d_{hkl}^2 \rangle}{\langle d_{hkl} \rangle^2} - 1$, where $\langle d_{hkl} \rangle$ is the mean lattice d-spacing of the (hkl) plane. Putting things

together, besides inclusions, both the mean and the variance of the lattice d-spacing within a crystal volume of 537nm^3 are varying and inhomogeneously distributed at the nanometer-scale.

The lattice of HEAs was expected to be severely distorted based on the atomic size misfit. Several models based on hard sphere packing have been proposed to estimate the size mismatch in HEAs. For example, the delta factor $\delta = \sqrt{\sum_{i=1}^N c_i (1 - r_i/\bar{r})^2}$, where N is the number of elements in HEA, c_i and r_i indicate the atomic fraction and radius of ith element, respectively. The magnitudes of strain and lattice distortion parameter obtained from SCBED are comparable with that of estimated from delta factors of 2-4% (47), however, are about 10 times larger than that of measured from X-ray or neutron scattering for single phase fcc HEAs (23, 24).

The above observation raises important questions about the roles of the inhomogeneous lattice distortion in thermodynamic stability and deformation mechanisms. The occurrence of clusters with displacements of $\sim 7.1\%$ from the averaged lattice and slow-varying strain over $\sim 50\text{nm}$ (Figs. 2 and 3) suggest the non-ideal solid solution nature in $\text{Al}_{0.1}\text{CrFeCoNi}$ HEA system (11). The identified Al-rich clusters is in agreement with the Pd-Pd pairs in PdCrFeCoNi observed by EXAFS studies, which the strain field follows Eshelby's inclusion theory (48); while the slow-varying strain is consistent with the spinodal decomposition of Cr, Fe-rich versus Al, Ni, Co-rich segregations observed in $\text{Al}_x\text{CrFeCoNi}$ systems with higher Al content (49, 50), as well as the Cr ordering in CrFeCoNi observed by quantitative atomic resolution imaging (51). Previously, first-

principles calculations have suggested the effect of lattice distortion on solid solution strengthening and phase stability by considering difference in atomic sizes (52, 53) and magnetism or electronic effects (10, 51, 54-57). Furthermore, the reported slow, intermittent dislocation motion in $\text{Al}_{0.1}\text{CrFeCoNi}$ observed using in-situ TEM can be attributed to the observed severe lattice distortion using SCBED, which is known to increase the Peierls-Nabarro stress (25).

5.5. Conclusions

In conclusion, we have used a recent-developed SCBED technique to directly visualize the local symmetry and strain in $\text{Al}_{0.1}\text{CrFeCoNi}$ HEA. Two types of symmetry breaking were found. One features 10 ± 3 nm, disc-shaped, clusters having $\sim 7.1\%$ tensile displacements along $\langle 110 \rangle$ directions, and the other gives rise to local fluctuating strain within $\pm 1.3\%$, which is slow-varying over ~ 50 nm. Furthermore, the diffraction peaks broadening is consistent with the paracrystal model having lattice distortion parameter of 2.12%.

5.6. References

1. D. A. Keen, A. L. Goodwin, The crystallography of correlated disorder. *Nature* **521**, 303 (May 21, 2015).
2. S. J. L. Billinge, I. Levin, The problem with determining atomic structure at the nanoscale. *Science* **316**, 561 (Apr 27, 2007).
3. B. Cantor, I. T. H. Chang, P. Knight, A. J. B. Vincent, Microstructural development in equiatomic multicomponent alloys. *Mat Sci Eng a-Struct* **375**, 213 (Jul 15, 2004).
4. J. W. Yeh *et al.*, Formation of simple crystal structures in Cu-Co-Ni-Cr-Al-Fe-Ti-V alloys with multiprincipal metallic elements. *Metall Mater Trans A* **35A**, 2533 (Aug, 2004).
5. J. W. Yeh *et al.*, Nanostructured high-entropy alloys with multiple principal elements: Novel alloy design concepts and outcomes. *Adv Eng Mater* **6**, 299 (May, 2004).
6. B. Gludovatz *et al.*, A fracture-resistant high-entropy alloy for cryogenic applications. *Science* **345**, 1153 (Sep 5, 2014).
7. B. Gludovatz *et al.*, Exceptional damage-tolerance of a medium-entropy alloy CrCoNi at cryogenic temperatures. *Nat Commun* **7**, (Feb, 2016).
8. T. F. Yang *et al.*, Effects of temperature on the irradiation responses of Al_{0.1}CoCrFeNi high entropy alloy. *Scripta Mater* **144**, 31 (Feb, 2018).
9. T. F. Yang *et al.*, Precipitation behavior of Al_xCoCrFeNi high entropy alloys under ion irradiation. *Sci Rep-Uk* **6**, (Aug 26, 2016).
10. Q. F. He, Y. Yang, On Lattice Distortion in High Entropy Alloys. *Front Mater* **5**, (Jul 24, 2018).
11. D. B. Miracle, O. N. Senkov, A critical review of high entropy alloys and related concepts. *Acta Mater* **122**, 448 (Jan 1, 2017).
12. E. J. Pickering, N. G. Jones, High-entropy alloys: a critical assessment of their founding principles and future prospects. *Int Mater Rev* **61**, 183 (2016).
13. M. H. Tsai, J. W. Yeh, High-Entropy Alloys: A Critical Review. *Mater Res Lett* **2**, 107 (2014).
14. Y. Zhang *et al.*, Microstructures and properties of high-entropy alloys. *Prog Mater Sci* **61**, 1 (Apr, 2014).
15. J. W. Yeh, Recent progress in high-entropy alloys. *Ann Chim-Sci Mat* **31**, 633 (Nov-Dec, 2006).
16. L. R. Owen, N. G. Jones, Lattice distortions in high-entropy alloys. *Journal of Materials Research* **33**, 2954 (2018).
17. Y. F. Kao, T. J. Chen, S. K. Chen, J. W. Yeh, Microstructure and mechanical property of as-cast, -homogenized, and -deformed Al_xCoCrFeNi (0 ≤ x ≤ 2) high-entropy alloys. *J Alloy Compd* **488**, 57 (Nov 20, 2009).

18. W. R. Wang *et al.*, Effects of Al addition on the microstructure and mechanical property of Al_xCoCrFeNi high-entropy alloys. *Intermetallics* **26**, 44 (Jul, 2012).
19. J. W. Yeh, Physical Metallurgy of High-Entropy Alloys. *Jom-U*s **67**, 2254 (Oct, 2015).
20. J. W. Yeh, S. Y. Chang, Y. D. Hong, S. K. Chen, S. J. Lin, Anomalous decrease in X-ray diffraction intensities of Cu-Ni-Al-Co-Cr-Fe-Si alloy systems with multi-principal elements. *Mater Chem Phys* **103**, 41 (May 15, 2007).
21. W. Guo *et al.*, Local Atomic Structure of a High-Entropy Alloy: An X-Ray and Neutron Scattering Study. *Metall Mater Trans A* **44A**, 1994 (May, 2013).
22. L. J. Santodonato *et al.*, Deviation from high-entropy configurations in the atomic distributions of a multi-principal-element alloy. *Nat Commun* **6**, (Jan, 2015).
23. Y. Tong *et al.*, Local lattice distortion in NiCoCr, FeCoNiCr and FeCoNiCrMn concentrated alloys investigated by synchrotron X-ray diffraction. *Mater Design* **155**, 1 (Oct 5, 2018).
24. L. R. Owen *et al.*, An assessment of the lattice strain in the CrMnFeCoNi high-entropy alloy. *Acta Mater* **122**, 11 (Jan 1, 2017).
25. Y. Hu *et al.*, Dislocation avalanche mechanism in slowly compressed high entropy alloy nanopillars. *Communications Physics* **1**, 61 (2018/10/01, 2018).
26. M. Schaffer, B. Schaffer, Q. Ramasse, Sample preparation for atomic-resolution STEM at low voltages by FIB. *Ultramicroscopy* **114**, 62 (Mar, 2012).
27. K. H. Kim, D. A. Payne, J. M. Zuo, Determination of 60 degrees polarization nanodomains in a relaxor-based ferroelectric single crystal. *Appl Phys Lett* **107**, 162902 (Oct 19, 2015).
28. Y. T. Shao, J. M. Zuo, Lattice-Rotation Vortex at the Charged Monoclinic Domain Boundary in a Relaxor Ferroelectric Crystal. *Phys Rev Lett* **118**, 157601 (Apr 14, 2017).
29. R. Yuan, Y. Meng, J. Zhang, J.-M. Zuo, Accurate Diffraction Peak Identification for Scanning Electron Nanodiffraction Based on Automated Image Processing and Feature Detection. *Microscopy and Microanalysis* **23**, 180 (2017).
30. K. H. Kim, J. M. Zuo, Symmetry quantification and mapping using convergent beam electron diffraction. *Ultramicroscopy* **124**, 71 (Jan, 2013).
31. Y.-T. Shao, J.-M. Zuo, Fundamental Symmetry of Barium Titanate Single Crystal Determined Using Energy-Filtered Scanning Convergent Beam Electron Diffraction. *Microscopy and Microanalysis* **22**, 516 (2016/007/001, 2016).
32. H. P. Degischer, Diffraction Contrast from Coherent Precipitates in Elastically-Anisotropic Materials. *Philos Mag* **26**, 1137 (1972).
33. M. F. Ashby, L. M. Brown, On Diffraction Contrast from Inclusions. *Philos Mag* **8**, 1649 (1963).
34. M. F. Ashby, L. M. Brown, Diffraction Contrast from Spherically Symmetrical Coherency Strains. *Philos Mag* **8**, 1083 (1963).

35. N. F. Mott, F. R. N. Nabarro, An attempt to estimate the degree of precipitation hardening, with a simple model. *P Phys Soc* **52**, 86 (Jan, 1940).
36. J. D. Eshelby, The Continuum Theory of Lattice Defects. *Solid State Phys* **3**, 79 (1956).
37. J. D. Eshelby, The Determination of the Elastic Field of an Ellipsoidal Inclusion, and Related Problems. *Proc R Soc Lon Ser-A* **241**, 376 (1957).
38. J. D. Eshelby, The Elastic Field Outside an Ellipsoidal Inclusion. *Proc R Soc Lon Ser-A* **252**, 561 (1959).
39. D. Healy, Elastic field in 3D due to a spheroidal inclusion-MATLAB (TM) code for Eshelby's solution. *Comput Geosci-Uk* **35**, 2170 (Oct, 2009).
40. C. F. Meng, W. Heltsley, D. D. Pollard, Evaluation of the Eshelby solution for the ellipsoidal inclusion and heterogeneity. *Comput Geosci-Uk* **40**, 40 (Mar, 2012).
41. P. B. Hirsch, Howie, A., Nicholson, R., Pashley, D. W., Whelan, M. J., *Electron microscopy of thin crystals*. (R.E. Krieger Pub. Co., Huntington, N.Y., 1977).
42. L. Sturkey, Calculation of Electron Diffraction Intensities. *P Phys Soc Lond* **80**, 321 (1962).
43. J. M. Zuo, J. C. H. Spence, *Advanced Transmission Electron Microscopy*. Imaging and Diffraction in Nanoscience (New York: Springer, ed. 1, 2017), pp. XXVI, 729.
44. J. L. Eads, R. P. Millane, Diffraction by the ideal paracrystal. *Acta Crystallographica Section A* **57**, 507 (Sep, 2001).
45. R. Hosemann, A. M. Hindeleh, Structure of Crystalline and Paracrystalline Condensed Matter. *J Macromol Sci Phys* **B34**, 327 (1995).
46. W. Xu, J. H. Dycus, J. M. LeBeau, Numerical modeling of specimen geometry for quantitative energy dispersive X-ray spectroscopy. *Ultramicroscopy* **184**, 100 (Jan, 2018).
47. Y. F. Ye, Q. Wang, J. Lu, C. T. Liu, Y. Yang, High-entropy alloy: challenges and prospects. *Mater Today* **19**, 349 (Jul-Aug, 2016).
48. G. V. Y. Tong, T. Yang, K. Jin, C. Lu, H. Bei, J. Y. P. Ko, D. C. Pagan, R. Huang, Y. Zhang, L. Wang, and F. X. Zhang, Probing local lattice distortion in medium- and high-entropy alloys. *arXiv:1707.07745*, (2017).
49. A. Manzoni, H. Daoud, R. Volkl, U. Glatzel, N. Wanderka, Phase separation in equiatomic AlCoCrFeNi high-entropy alloy. *Ultramicroscopy* **132**, 212 (Sep, 2013).
50. T. F. Yang *et al.*, Effects of AL addition on microstructure and mechanical properties of Al_xCoCrFeNi High-entropy alloy. *Mat Sci Eng a-Struct* **648**, 15 (Nov 11, 2015).
51. C. Niu *et al.*, Spin-driven ordering of Cr in the equiatomic high entropy alloy NiFeCrCo. *Appl Phys Lett* **106**, (Apr 20, 2015).
52. N. L. Okamoto, K. Yuge, K. Tanaka, H. Inui, E. P. George, Atomic displacement in the CrMnFeCoNi high-entropy alloy - A scaling factor to predict solid solution strengthening. *Aip Adv* **6**, (Dec, 2016).

53. Y. Zhang, Y. J. Zhou, J. P. Lin, G. L. Chen, P. K. Liaw, Solid-solution phase formation rules for multi-component alloys. *Adv Eng Mater* **10**, 534 (Jun, 2008).
54. T. Egami, M. Ojha, O. Khorgolkhuu, D. M. Nicholson, G. M. Stocks, Local Electronic Effects and Irradiation Resistance in High-Entropy Alloys. *Jom-U.S.* **67**, 2345 (Oct, 2015).
55. H. S. Oh *et al.*, Lattice Distortions in the FeCoNiCrMn High Entropy Alloy Studied by Theory and Experiment. *Entropy-Switz* **18**, (Sep, 2016).
56. Y. F. Ye *et al.*, Atomic-scale distorted lattice in chemically disordered equimolar complex alloys. *Acta Mater* **150**, 182 (May 15, 2018).
57. H. Q. Song *et al.*, Local lattice distortion in high-entropy alloys. *Phy Rev Mater* **1**, (Jul 19, 2017).

CHAPTER 6

SUMMARY AND OUTLOOKS

6.1. Summary

In this study, we have further developed SCBED as a versatile and robust technique for characterization of local disorder in complex, multi-element crystals. Both local and average crystallographic symmetry can be determined by varying the illuminated sample volume, which can be achieved by using various electron probe sizes and specimen thicknesses.

We have further improved the symmetry quantification algorithm for SCBED, which demonstrated the sensitivity of detecting nanoscale symmetry fluctuations within a single domain in BaTiO₃ single crystals. The interpretation of the observed symmetry fluctuation is twofold: 1) the local symmetry breaking can be explained by the anharmonicity of soft phonons within the displacive model of ferroelectric phase transition; or alternatively, 2) the population variations of the $\langle 111 \rangle$ polarizations along the electron beam direction, which is consistent with the order-disorder phase transition mechanism.

For relaxor ferroelectric PZN-8%PT, we have successfully determined the 50° nanodomains of monoclinic *Pm* symmetry using SCBED. The local structure of PZN-8%PT is drastically different from that of PMN-31%PT, which the latter is found to be triclinic at nanoscale (1, 2). Furthermore, by measuring the intensity redistributions within the transmitted (000) disk, we found a new type of defect, lattice-rotation vortex, at the boundary of nanodomains. The observed lattice-rotation vortices can be explained by disinclination strain and depolarization fields due to charge discontinuity.

Besides polarization determination, we extend the application of SCBED by demonstrating the capability of imaging quantitatively the lattice distortions and local symmetry breaking in HEAs. Our results revealed two types of lattice distortions in $\text{Al}_{0.1}\text{CrFeCoNi}$: 1) 10 ± 3 nm, disc-shaped, clusters having $\sim 7.1\%$ tensile displacements along $\langle 110 \rangle$ directions distributed throughout the specimen, and 2) the local fluctuating strain within $\pm 1.3\%$, which is slow-varying over ~ 50 nm. Both suggest the non-ideal nature of solid solutions and thermodynamic instabilities, which contradict with previous speculations based on the high entropy hypothesis. Our results, made possible using SCBED, thus demonstrate a new powerful experimental approach towards quantitative study of complex, multi-element crystals.

6.2. Outlooks

6.2.1. Quantitative refinement of SCBED: SQCBED

The refinement of diffracted intensity in experimental CBED patterns using Bloch-wave method, or quantitative CBED (QCBED), have been shown to measure low order structure factors and crystal bonding charge density with accuracy of $< 0.09\%$ (3, 4). The fundamental assumption of Bloch-wave method is based on the translational symmetry of a unit cell. Disordered crystals, unfortunately cannot be applied in this regime.

Alternatively, dynamical diffraction intensities can be calculated from non-periodic structures using the multislice or the Bloch-wave scattering matrix methods (5-7). The retrieval of structural information based on the Bloch-wave scattering matrix method has been demonstrated by Pennington & Koch (8). Using simulated CBED data of BaTiO_3 , their algorithm was able to retrieve the 3D Ti displacements with lateral accuracy of 3pm

and depth resolution of 5-10nm. The success of this simulation experiment has demonstrated a promising possibility, the scanning quantitative CBED (SQCBED) technique, to retrieve the 3D structural information from every CBED pattern in the SCBED dataset, i.e., diffraction tomography without tilting. This is an ongoing effort in Zuo group in collaboration with Prof. Philip Nakashima's group (Monash University, Australia) to develop multislice-based SQCBED to study 3D structures of voids in metals.

6.2.2. Rocking beam SCBED: SRCBED

Another limitation of the SCBED technique is the disk size, or the convergence angle. To avoid the overlapping of disks, the largest disk radius, or semi-convergence angle α , is restricted by the Bragg angle θ_B . Hence for large unit cell crystals, there is limited angular range of data can be recorded in a CBED pattern. Large-angle CBED (LACBED) patterns obtained by the Tanaka method operates by defocusing the specimen plane, which drastically sacrifices the spatial resolution up to ~100s nm. Recently, Koch (9) and Beanland (10) groups have used computer control to rock/tilt the electron beam, which provides LACBED patterns and keeps the probe within a few nm by patching many CBED disks from individual beam tilts. We propose to develop LACBED with scanning based techniques, scanning rocking CBED (SRCBED), to map nanometer-scale structure variations in large unit cell crystals such as unconventional superconductors such as $\text{YBa}_2\text{Cu}_3\text{O}_{7-x}$. Furthermore, SRCBED can be extended by changing the electron beam into a low-dose, parallel illumination. By patching the spot-like Bragg reflections into disks allows the determination of local handedness and chirality variations in beam-sensitive

materials such as metal-organic framework or crystalline polymers. Effort is ongoing in Zuo group to develop SRCBED to study strongly correlated materials.

6.2.3. Time-resolved SCBED

The SCBED data in this thesis assumes that the specimen is static. The experimental acquisition time, hence the drift in specimen stage, is limited by the CCD acquisition speed of ~1-10 frames per second (fps). The temporal resolution of SCBED can be improved either by using fast cameras or by ultrafast pump-probe approach. First, recent developments of fast camera with speed of >1000fps has enabled atomic-resolution in-situ TEM with millisecond time resolution (11). In combination with SCBED, in-situ deformation for strain measurements has been demonstrated by Gammer *et al.* where time-resolved 2D strain maps can be correlated with the load-displacement curve (12). For relaxor ferroelectrics, we propose to study the switching behavior of nanodomains as well as the temperature-dependent behavior of PNRs by combining in-situ biasing/heating with SCBED. Second, ultrafast electron pulses generated by photoemission has enabled the study of transient structures with temporal resolution of ns to fs. Ultrafast CBED has been demonstrated for the determination of strain dynamics by utilizing the change in HOLZ lines (13) and Kikuchi bands (14). With the recently customized Hitachi 9500 environmental TEM at University of Illinois, we propose to study the phonon softening associated with structural phase transitions in the nanosecond to picosecond regime in correlated systems such as ferroelectrics.

6.3. References

1. K. H. Kim, D. A. Payne, J. M. Zuo, Symmetry of piezoelectric $(1-x)\text{Pb}(\text{Mg}_{1/3}\text{Nb}_{2/3})\text{O}-3-x\text{PbTiO}_3$ ($x=0.31$) single crystal at different length scales in the morphotropic phase boundary region. *Phys Rev B* **86**, 184113 (Nov 29, 2012).
2. K. H. Kim, D. A. Payne, J. M. Zuo, Determination of fluctuations in local symmetry and measurement by convergent beam electron diffraction: applications to a relaxor-based ferroelectric crystal after thermal annealing. *J Appl Crystallogr* **46**, 1331 (Oct, 2013).
3. P. N. H. Nakashima, A. E. Smith, J. Etheridge, B. C. Muddle, The Bonding Electron Density in Aluminum. *Science* **331**, 1583 (Mar 25, 2011).
4. J. M. Zuo, M. Kim, M. O'Keeffe, J. C. H. Spence, Direct observation of d-orbital holes and Cu-Cu bonding in Cu_2O . *Nature* **401**, 49 (Sep 2, 1999).
5. J. M. Cowley, A. F. Moodie, The Scattering of Electrons by Atoms and Crystals .1. A New Theoretical Approach. *Acta Crystallogr* **10**, 609 (1957).
6. K. Ishizuka, Multislice Formula for Inclined Illumination. *Acta Crystallographica Section A* **38**, 773 (1982).
7. L. Sturkey, Calculation of Electron Diffraction Intensities. *P Phys Soc Lond* **80**, 321 (1962).
8. R. S. Pennington, C. T. Koch, A three-dimensional polarization domain retrieval method from electron diffraction data. *Ultramicroscopy* **155**, 42 (Aug, 2015).
9. C. T. Koch, Aberration-compensated large-angle rocking-beam electron diffraction. *Ultramicroscopy* **111**, 828 (Jun, 2011).
10. R. Beanland, P. J. Thomas, D. I. Woodward, P. A. Thomas, R. A. Roemer, Digital electron diffraction - seeing the whole picture. *Acta Crystallographica Section A* **69**, 427 (Jul, 2013).
11. W. P. Gao *et al.*, Dynamics of Transformation from Platinum Icosahedral Nanoparticles to Larger FCC Crystal at Millisecond Time Resolution. *Sci Rep-Uk* **7**, (Dec 8, 2017).
12. C. Gammer *et al.*, Local and transient nanoscale strain mapping during in situ deformation. *Appl Phys Lett* **109**, (Aug 22, 2016).
13. A. Feist, N. R. da Silva, W. X. Liang, C. Ropers, S. Schaefer, Nanoscale diffractive probing of strain dynamics in ultrafast transmission electron microscopy. *Struct Dynam-Uk* **5**, (Jan, 2018).
14. A. Yurtsever, S. Schaefer, A. H. Zewail, Ultrafast Kikuchi Diffraction: Nanoscale Stress-Strain Dynamics of Wave-Guiding Structures. *Nano Lett* **12**, 3772 (Jul, 2012).

APPENDIX A:

DM SCRIPT FOR SCBED

A.1. Scanning electron diffraction acquisition

```
/*
Scanning_ED, (Scanning electron diffraction acquisition)
Yu-Tsun Shao, Ph.D. Candidate, U of Illinois

This script is for scanning electron diffraction. 'EMGet-' or 'EMSet-' functions are used to control TEM.

Start development: 05.05.10
10.05.07 - Dialog Box created
10.05.09 - Calibration part is done.
10.05.10 - Calibration part is added.
10.05.10 - Starts 'Acquire Part'
10.05.17 - Experimental conditions are added into result.
10.11.07 - Centered scan and check scan options added
11.10.30 - Tested for Cryo TEM (Image size changed from 1024 to 2048)
16.12.16 - Added for scan rotation (Yifei Meng, Univ. of Illinois)
17.04.07 - (Background) Thread
17.04.09 - Tested for threading (Tianyu Liu, Monash Uni. & Yu-Tsun Shao, Univ. of Illinois)
17.06.28 - Tested on JEOL ARM 200CF TEM-mode @NTNU Trondheim (Yu-Tsun Shao, Univ. of Illinois)
17.10.12 - debugged for scan rotation angle (Yu-Tsun Shao, Univ. of Illinois)
17.11.05 - debugged for "center" function; enable rectangular CCD (such as the camera on 2010 LaB6) (Yu-Tsun Shao, Univ. of Illinois)
*/

// Declaration of variables
TagGroup Binning, Exp // Binning and exposure time
TagGroup xNum, yNum // Data points along x and y direction
TagGroup xLength, yLength // Step length along x and y direction
TagGroup RealNum1, RealNum2, RealNum3, RealNum4, RealNum5, RealNum6, RealNum7, RealNum8, RealNum9, RealNum10, RealNum11, RealNum10_x,
RealNum10_y
TagGroup Name1, Name2, Name3 // Specimen name, Mode, Magnification
TagGroup ScanOption, CheckScan //Check scan option deleted on 2011/11/02
number abort=0 // mission aborted? for background thread

/* TagGroup description
RealNum1 = Binning
RealNum2 = Exposure time
RealNum3 = Data points X
RealNum4 = Data points Y
RealNum5 = Step Length X
RealNum6 = Step Length Y
RealNum7 = Spot Size
RealNum8 = Alpha
RealNum10 = CCD pixel size
RealNum10_x, RealNum10_y (for rectangular CCD)
RealNum11 = tilt angle degree
*/

// Thread
Class AcquThread: Thread
{
    void f_Start ( object self)
    {
        number angleDegree
        DLGGetValue(RealNum11,angleDegree)
        number tiltAngle = angleDegree*3.14159265359/180
        //Gets experimental conditions
        String Mode, Mag
        Number Alpha, SpotSize
        DLGGetValue (Name2, Mode)
        DLGGetValue (Name3, Mag)
        DLGGetValue (RealNum7, Alpha)
        DLGGetValue (RealNum8, SpotSize)

        //Gets a specimen name
        String SpecimenName
        DLGGetValue (Name1, SpecimenName)

        //Gets a CCD pixel size
        Number CCDPixelsX, CCDPixelsY
        DLGGetValue (RealNum10_x, CCDPixelsX)
        DLGGetValue (RealNum10_y, CCDPixelsY)

        //Gets a binning value
        number Binning
        DLGGetValue (RealNum1, Binning)

        //Gets an exposure time
        number ExpTime
        DLGGetValue (RealNum2, ExpTime)
    }
}
```

```

//Gets a data point
number XPoints, YPoints
DLGGetValue (RealNum3, XPoints)
DLGGetValue (RealNum4, YPoints)

//Gets a step length
number StepL_X, StepL_Y, CorF
DLGGetValue (RealNum5, StepL_X)
DLGGetValue (RealNum6, StepL_Y)

//Stores the setting values in TagBase("LastSettingValues")
String TagBase=("LastSettingValues_SED")
SetPersistentStringNote(TagBase+"Mode", Mode)
SetPersistentStringNote(TagBase+"Mag", Mag)
SetPersistentNumberNote(TagBase+"Alpha", Alpha)
SetPersistentNumberNote(TagBase+"SpotSize", SpotSize)
SetPersistentStringNote(TagBase+"SpecimenName", SpecimenName)
SetPersistentNumberNote(TagBase+"CCDPixelsX", CCDPixelsX)
SetPersistentNumberNote(TagBase+"CCDPixelsY", CCDPixelsY)
SetPersistentNumberNote(TagBase+"Binning", Binning)
SetPersistentNumberNote(TagBase+"ExpTime", ExpTime)
SetPersistentNumberNote(TagBase+"XPoints", XPoints)
SetPersistentNumberNote(TagBase+"YPoints", YPoints)
SetPersistentNumberNote(TagBase+"StepL_X", StepL_X)
SetPersistentNumberNote(TagBase+"StepL_Y", StepL_Y)
SetPersistentNumberNote(TagBase+"CorF", CorF)

// Recall the calibrated unit
TagBase = ("SED_Calibration")
String Units
GetPersistentStringNote(TagBase + "CalUnits", units)

// Recall the calibrated data
TagBase = ("SED_Calibration")
complexnumber c_Horz_UnitVector, c_Vert_UnitVector
number real_HorzScale, real_VertScale
GetPersistentNumberNote(tagBase + "HorzCal", real_HorzScale)
GetPersistentComplexNumberNote(tagBase + "c_Horz_UnitVector", c_Horz_UnitVector)
GetPersistentNumberNote(tagBase + "VertCal", real_VertScale)
GetPersistentComplexNumberNote(tagBase + "c_Vert_UnitVector", c_Vert_UnitVector)

// Store the initial value of deflector: This needs to move the beam back to the initial position after scanning function.
number TDefX_1, TDefY_1
EMGetBeamShift(TDefX_1, TDefY_1)
TagBase=("InitialDefValue0")
SetPersistentNumberNote(TagBase+"xDefValue0", TDefX_1)
SetPersistentNumberNote(TagBase+"yDefValue0", TDefY_1)

//Centered Scan option: The scanning rectangular area has the center with the initial beam position.
ComplexNumber StartDef
Number DefaultScanOption
DefaultScanOption=ScanOption.DlgGetValue()
If (DefaultScanOption==1)
{
number radiusDef = SQRT((XPoints-1)**2+(YPoints-1)**2)/2
number initAngle = pi() - atan((YPoints-1)/(XPoints-1))

StartDef = complex(TDefX_1, TDefY_1) + c_Horz_UnitVector*real_HorzScale*StepL_X*radiusDef*cos(initAngle-tiltAngle) -
c_Vert_UnitVector*real_VertScale*StepL_Y*radiusDef*sin(initAngle-tiltAngle)
//OLD: wrong
//StartDef=complex(TDefX_1, TDefY_1)-c_Vert_UnitVector*(0.5*(Ypoints-1)*StepL_Y*real_VertScale)-
c_Horz_UnitVector*(0.5*(Xpoints-1)*real_HorzScale*StepL_X)
SetPersistentComplexNumberNote(TagBase+"StartDef", StartDef)
}
Else
{
StartDef=complex(TDefX_1, TDefY_1)
SetPersistentComplexNumberNote(TagBase+"StartDef", StartDef)
}
// End

GetPersistentComplexNumberNote(TagBase+"StartDef", StartDef)

// Work Image
Number TotSlice=XPoints*YPoints
Image Img3D :=
IntegerImage(SpecimenName+"_"+XPoints+"by"+YPoints+"pts_"+"StepL_X"+"by"+StepL_Y+"units+"_"+"Mode+"_"+"Mag+"_Alpha("+Alpha+")"+"_S pot("+SpotSize+)",
2, 1, CCDPixelsX/Binning , CCDPixelsY/Binning , TotSlice) // IntegerImage ("Image name", # bytes, singed or not, pixels, pixels, total slice numbers)
Img3D.ShowImage()
Imagedisplay ImgDisp3D = Img3D.ImageGetImageDisplay(0)
Number Slice_n=0

// Processing time measurement
Number Start=GetHighResTickCount()

// Shift a beam and record an image
Number iY=0
ComplexNumber ScanningDef
while (iy<YPoints)
{
number ix=0

```

```

        while (ix<XPoints)
        {
            ScanningDef=StartDef+c_Horz_UnitVector*((ix*real_HorzScale*StepL_X)*cos(tiltAngle)-
            (iy*StepL_Y*real_VertScale)*sin(tiltAngle))+c_Vert_UnitVector*((iy*StepL_Y*real_VertScale)*cos(tiltAngle)+(ix*real_HorzScale*StepL_X)*sin(tiltAngle))
            // EMSetBeamShift(Real(ScanningDef), Imaginary(ScanningDef))
            Image WorkImage := slice2( Img3D,0,0,Slice_n,0,CCDPixelsX/Binning,1,1,CCDPixelsY/Binning,1) // void
            // stored on Z, Image pixels(x), --, --, Image pixels(y), --)
            SSCGainNormalizedBinnedAcquireInPlace (WorkImage , ExpTime, Binning, 0, 0, CCDPixelsX/Binning,
            CCDPixelsY/Binning)

            if(abort) {
                if(TwoButtonDialog("Abort scanning?","Yes","No")) {
                    showAlert("Scanning aborted!",1)
                    exit(-1)
                }
                else
                    abort=0
            }
            ImgDisp3D.ImageDisplaySetDisplayedLayers( Slice_n, Slice_n) //Show the image of slice number 'Real
            number, Real Number'

            Img3D.UpDateImage()
            OpenAndSetProgressWindow("Current Frame: "+Slice_n,"Total: "+TotSlice,"")
            ix++
            Slice_n++
        }
        ScanningDef=StartDef
        iy++
    }

    //Time Measurement
    Number End=GetHighResTickCount()
    number time_sec = CalcHighResSecondsBetween(start, end)
    number time_min = time_sec / 60
    Result("Experimental Results\n")
    Result("Total Slices: "+TotSlice+"\n")
    Result("Exposure time: "+ExpTime+"\n")
    Result("Total recording time: " + time_sec.format( "%.2g" ) + " sec. (" + time_min.format( "%.1f" ) + " min.)\n")
    Number SliceT=time_sec/TotSlice
    Result("Processing time for each slice: "+SliceT+"\n")

    //Image Calibration
    Img3D.ImageCopyCalibrationFrom(SSCUprocessedBinnedAcquire(0,Binning,0,0,32,32))
    Img3D.ImageSetDimensionUnitString( 2, "frame" )
    Img3D.ImageSetDimensionScale( 2, 1 )

    // Move the beam back to the initial position
    TagBase=("InitialDefValue0")
    GetPersistentNumberNote(TagBase+"xDefValue0", TDefX_1)
    GetPersistentNumberNote(TagBase+"yDefValue0", TDefY_1)
    EMSetBeamShift(TDefX_1, TDefY_1)
    OKDialog ("Acquition is done.")
}

Void AcquStop(Object self) { abort = 1; }

~AcquThread(Object self) { self.AcquStop(); }

Void RunThread(Object self)
{
    abort = 0
    self.f_Start()
}
}
// End thread

// The User Interface Frame creates the actions of the buttons
// Define fuctions of each button when it is pressed
class DialogLibraryTestClass4 : uiframe
{
    object thread

    // Creates actions of the buttons in Control Box 2
    //1. Calibration button
    void f_cal(object self) // Calibrate the instrument when 'Calibration button' is pressed.
    {

        IF(!OkCancelDialog("Start 'Search Mode' to calibrate TEM.\nIf TEM is not 'Search Mode', press 'Cancel' and run this program again!"))
        {
            exit(0)
        }

        IF(!OkCancelDialog("1. Please check not to run this mode under 'Diffraction Mode' (200kx GIF).\n2. Choose a proper sample area not
        to damage the CCD camera."))
        {
            exit(0)
        }

        image img := GetFrontImage()
        imagedisplay imgDisplay = img.ImageGetImageDisplay(0)

        // Gets image information
        Number CCDPixelsX, CCDPixelsY
        DLGGetValue (RealNum10_x, CCDPixelsX)
        DLGGetValue (RealNum10_y, CCDPixelsY)
    }
}

```

```

number width = img.ImageGetDimensionSize( 0 )
number height = img.ImageGetDimensionSize( 1 )
number bin = CCDPixelsY/height
number scale = img.ImageGetDimensionScale(0)
string units = img.ImageGetDimensionUnitString(0)

//Creates ROI boxes on the front image
imagedisplay imgdisp = img.ImageGetImageDisplay(0)
ROI ROI1=NewROI()
number top, left, bottom, right
top=height*0.2
left=width*0.2
bottom=height*0.8
right=width*0.8
ROI1.ROISetRectangle(top, left, bottom, right)
ROI1.ROISetVolatile(0)
ROI1.ROISetMoveable(0)
imgDisplay.ImageDisplayAddROI( ROI1 )

//Calculate a real scale from the image
number r_width=abs((bottom-top)*scale)
number r_height=abs((left-right)*scale)
result ("width="+r_width+" "+units+", "+r_height="+r_height+" "+units+"\n")

//Shows ROIs for beam position
//Beam box 1
ROI ROI2=NewROI()
number ROI2_top=top-50/bin
number ROI2_left=left-50/bin
number ROI2_bottom=top+50/bin
number ROI2_right=left+50/bin
ROI2.ROISetRectangle( ROI2_top, ROI2_left, ROI2_bottom, ROI2_right)
ROI2.ROISetVolatile(0)
ROI2.ROISetMoveable(0)
ROI2.ROISetColor(0,0,1)

String Label_ROI2="Locate a beam center on this box"
ROI2.ROISetLabel(label_ROI2)
imgDisplay.ImageDisplayAddROI( ROI2 )

//Get deflector's current - 1
number DefX_1, DefY_1
if(!OKCancelDialog("Use a beam shift knob to locate in the blue box.\nPress 'OK' when you are done.))
    exit(0)
EMGetBeamShift(DefX_1, DefY_1) //FasTEM_GetDefValue (Deflector number, xDefValue, yDefValue)
OKDialog ("Click to continue")
imgDisplay.ImageDisplayDeleteROI(ROI2)

//Beam box 2
ROI2_top=top+50/bin
ROI2_left=right-50/bin
ROI2_bottom=top-50/bin
ROI2_right=right+50/bin
ROI2.ROISetRectangle( ROI2_top, ROI2_left, ROI2_bottom, ROI2_right)
ROI2.ROISetVolatile(0)
ROI2.ROISetMoveable(0)
ROI2.ROISetColor(0,0,1)

ROI2.ROISetLabel(label_ROI2)
imgDisplay.ImageDisplayAddROI( ROI2 )

//Get deflector's current - 2
number DefX_2, DefY_2
if(!OKCancelDialog("Use a beam shift knob to locate in the blue box.\nPress 'OK' when you are done.))
    exit(0)
EMGetBeamShift(DefX_2, DefY_2)
OKDialog ("Click to continue")

//Beam box 3
ROI2_top=bottom+50/bin
ROI2_left=right-50/bin
ROI2_bottom=bottom-50/bin
ROI2_right=right+50/bin
ROI2.ROISetRectangle( ROI2_top, ROI2_left, ROI2_bottom, ROI2_right)
ROI2.ROISetVolatile(0)
ROI2.ROISetMoveable(0)
ROI2.ROISetColor(0,0,1)

ROI2.ROISetLabel(label_ROI2)
imgDisplay.ImageDisplayAddROI( ROI2 )

//Get deflector's current - 3
number DefX_3, DefY_3
if(!OKCancelDialog("Use a beam shift knob to locate in the blue box.\nPress 'OK' when you are done.))
    exit(0)
EMGetBeamShift(DefX_3, DefY_3)
OKDialog ("Click to continue")
imgDisplay.ImageDisplayDeleteROI(ROI1)
imgDisplay.ImageDisplayDeleteROI(ROI2)

//Print results
result("\n-----\n")
result("\n          Calibration results\n")

```

```

result("\n-----\n")

//Convert deflector's current to a real unit
complexnumber c_Horz=(complex(DefX_2, DefY_2)-complex(DefX_1, DefY_1)) // Convert the beam current change to a horizontal
vector component
number real_HorzScale=sqrt(norm(c_Horz))/r_width // Ratio of 'Beam current change' to 'Real unit' (# current/1 nm)
complexnumber c_Horz_UnitVector=c_Horz/sqrt(norm(c_Horz)) // Calculate a horizontal unit vector

complexnumber c_Vert=(complex(DefX_3, DefY_3)-complex(DefX_2, DefY_2)) // Convert the beam current change to a vertical vector
component
number real_VertScale=sqrt(norm(c_Vert))/r_height // Ratio of 'Beam current change' to 'Real unit' (# current/1 nm)
complexnumber c_Vert_UnitVector=c_Vert/sqrt(norm(c_Vert)) // Calculate a vertical unit vector

OKDialog ("Please check calibration by using 'Test' button in Calibration box.")

string Time=GetTime(1),Date=GetDate(1)

//Save the calibration result in script
String tagBase = ("SED_Calibration")
SetPersistentStringNote(TagBase + "CalUnits", units)
SetPersistentNumberNote(tagBase + "HorzCal", real_HorzScale)
SetPersistentComplexNumberNote(tagBase + "c_Horz_UnitVector", c_Horz_UnitVector)
SetPersistentNumberNote(tagBase + "VertCal", real_VertScale)
SetPersistentComplexNumberNote(tagBase + "c_Vert_UnitVector", c_Vert_UnitVector)
SetPersistentStringNote(tagBase + "CalUnits", units )
SetPersistentStringNote(tagBase + "CalDate", Date )
SetPersistentStringNote(tagBase + "CalTime", Time )
GetPersistentStringNote(TagBase + "CalDate", Date )
GetPersistentStringNote(TagBase + "CalTime", Time )
result("\n>Last Calibration: "+Date+" "+Time+"\n")

//For check
result("\nCalibrated area\n")
result ("Width= "+r_width+" "+units+", "+r_height+" "+units+"\n")
result("\nHorizontal Scale= "+real_HorzScale+" (# current/1 )"+units+"\n")
result("Vertical unit vector= "+c_Horz_UnitVector+" (current)\n")
result("\nVertical Scale= "+real_VertScale+" (# current/1 )"+units+"\n")
result("Horizontal unit vector= "+c_Vert_UnitVector+" (current)\n")
}
// End of scripts for 'Calibration button' in Control Box 2

Void Start(Object self) { thread.StartThread(); }
Void Stop(Object self) { thread.AcquStop(); }

Object Init(Object self, taggroup dialog, Number thread_id) {
    thread = GetScriptObjectFromID(thread_id)

    Return self.super.Init(dialog)
}

}

// Creates the buttons, fields and labels in the dialog
//Script Information
taggroup ScriptInfo()
{
    taggroup ScriptInfo=dlgcreateLabel("\nScanning Electron NanoDiffraction (SEND)\n")
    ScriptInfo.dlgexternalpadding(10,0)
    return ScriptInfo
}

// Creates the buttons in Control Box 1
TagGroup ExperimentalCondition()
{
    TagGroup Box0_Items
    TagGroup Box0=DlgCreateBox(" Experimental Conditions ", box0_items)

    //Recall the last setting values
    String TagBase=("LastSettingValues_SED")
    String Mode, Mag
    Number Alpha, SpotSize
    GetPersistentStringNote(TagBase+"Mode", Mode)
    GetPersistentStringNote(TagBase+"Mag", Mag)
    GetPersistentNumberNote(TagBase+"Alpha", Alpha)
    GetPersistentNumberNote(TagBase+"SpotSize", SpotSize)

    String Name
    TagGroup Label11=DLGCreateLabel(" Mode: ")
    Label11.DLGExternalPadding(0, 0)
    Name2=DLGCreateStringField (Name, 8)
    Name2.DLGExternalPadding(0, 0)
    DLGValue(Name2, Mode)

    TagGroup Label12=DLGCreateLabel(" Mag: ")
    Label12.DLGExternalPadding(0,0)
    Name3=DLGCreateStringField (Name, 10)
    Name3.DLGExternalPadding(0,0)
    DLGValue(Name3, Mag)

    TagGroup Group11=DLGGroupItems(Label11, Name2, Label12, Name3)
    Group11.DLGTableLayout(4, 1, 0)
    Box0_items.DLGAddElement(Group11)
    Group11.DLGExternalPadding(12,3)
}

```



```

TagGroup Label14=DLGCreateLabel(" Spot Size : ")
Label14.DLGEexternalPadding(0, 0)
RealNum8=DLGCreateRealField (0,7, 0)
RealNum8.DLGEexternalPadding(0,0)
DLGValue(RealNum8, SpotSize)

TagGroup Label13=DLGCreateLabel("Alpha : ")
Label13.DLGEexternalPadding(1,1)
RealNum7=DLGCreateRealField (0, 7, 0)
Name2.DLGEexternalPadding(0,0)
DLGValue(RealNum7, Alpha)

TagGroup Group12=DLGGroupItems(Label14, RealNum8, Label13, RealNum7)
Group12.DLGTableLayout(4, 1, 0)
Box0_items.DLGAddElement(Group12)
Group12.DLGEexternalPadding(19, 0)

Box0.DLGEexternalPadding(0, 0)
Return Box0
}

// Creates the buttons in Control Box 1
TagGroup MainControlBox1()
{
    // Make 'other buttons' - Group 2 starts from here
    taggroup box2_items //Control box 2 is grouped by 'box2_items//
    taggroup box2=dlgcreatebox(" Control Box 1 ", box2_items) // Label of 'Control Box 1'

    //Recall the last setting values
    String TagBase=("LastSettingValues_SED")
    number CCDPixelsX, CCDPixelsY, Binning, ExpTime, Xpoints, YPoints, StepL_X, StepL_Y, CorF, angleDegree
    String SpecimenName
    GetPersistentStringNote(TagBase+"SpecimenName", SpecimenName)
    GetPersistentNumberNote(TagBase+"CCDPixelsX", CCDPixelsX)
    GetPersistentNumberNote(TagBase+"CCDPixelsY", CCDPixelsY)
    GetPersistentNumberNote(TagBase+"Binning", Binning)
    GetPersistentNumberNote(TagBase+"ExpTime", ExpTime)
    GetPersistentNumberNote(TagBase+"XPoints", XPoints)
    GetPersistentNumberNote(TagBase+"YPoints", YPoints)
    GetPersistentNumberNote(TagBase+"StepL_X", StepL_X)
    GetPersistentNumberNote(TagBase+"StepL_Y", StepL_Y)
    GetPersistentNumberNote(TagBase+"CorF", CorF)
    GetPersistentNumberNote(TagBase+"angleDegree", angleDegree)

    // Specimen Name
    String Name
    TagGroup Label10=DLGCreateLabel("1. Specimen Name: ")
    Label10.DLGEexternalPadding(1,1)
    Name1=DLGCreateStringField (Name, 25)
    Name1.DLGEexternalPadding(0,0)
    DLGValue(Name1, SpecimenName)

    TagGroup Group10=DLGGroupItems(Label10, Name1)
    Group10.DLGTableLayout(2,1,0)
    Box2_items.DLGAddElement(Group10)
    Group10.DLGEexternalPadding(0,3)

    //CCD pixel size: 2010F(1024), 2100 Cryo (2048)
    TagGroup CCDLabelx=DLGcreateLabel("2. CCD pixel size X: ")
    CCDLabelx.DLGEexternalPadding(1,1)
    RealNum10_x=DLGCreateRealField(0,9,0)
    RealNum10_x.DLGEexternalPadding(0,0)
    TagGroup CCDLabely=DLGCreateLabel("pixel size Y: ")
    CCDLabely.DLGEexternalPadding(1,1)
    RealNum10_y=DLGCreateRealField(0,9,0)
    RealNum10_y.DLGEexternalPadding(0,0)
    DLGValue(RealNum10_x,CCDPixelsX)
    DLGValue(RealNum10_y,CCDPixelsY)

    TagGroup CCDGroup=DLGGroupItems(CCDLabelx, RealNum10_x, CCDLabely, RealNum10_y)
    CCDGroup.DLGTableLayout(4,1,0)
    Box2_items.DLGAddElement(CCDGroup)
    CCDGroup.DLGEexternalPadding(0,3)

    //Binning and Exposure time
    TagGroup label1 = DLGCreateLabel("3. Binning:")
    label1.dlgexternalpadding(1,1)
    RealNum1 = DLGCreateRealField(0, 7, 2)
    RealNum1.dlgexternalpadding(0,0)
    DLGValue(RealNum1,Binning)

    TagGroup label2 = DLGCreateLabel(" 4. Exp time:")
    label2.dlgexternalpadding(1,1)
    RealNum2 = DLGCreaterealField(0,7,2)
    RealNum2.dlgexternalpadding(0,0)
    DLGValue(RealNum2,ExpTime)

    TagGroup group1 = DLGGroupItems(label1, RealNum1,label2, RealNum2)
    group1.DLGTableLayout(6, 1, 0)
    box2_items.DLGAddElement(group1)
    group1.DLGEexternalPadding(0,3)
}

```

```

//2nd row - Step numbers and length
TagGroup label3=DLGCreateLabel("4. Data points   "+"x:")
label3.dlgexternalpadding(1,1)
RealNum3 = DLGCreateRealField(0, 7, 0)
RealNum3.dlgexternalpadding(0,0)
DLGValue(RealNum3,XPoints)

TagGroup label4 = DLGCreateLabel("  y:")
label4.dlgexternalpadding(1,1)
RealNum4 = DLGCreateRealField(0, 7, 0)
RealNum4.dlgexternalpadding(0,0)
dlgvalue(RealNum4,YPoints)

TagGroup group2 = DLGGroupItems(label3, RealNum3, label4, RealNum4)
group2.DLGTableLayout(7, 1, 0)
box2_items.dlgaddelement(group2)
group2.dlgexternalpadding(0,3)

//3rd row - Step length
TagBase = ("SED_Calibration")
String Units
GetPersistentStringNote(TagBase + "CalUnits", units)
TagGroup label5=DLGCreateLabel("5. Step Length ("+units+" ) "+"x:")
label5.dlgexternalpadding(1,1)
RealNum5 = DLGCreateRealField(0,7,2)
RealNum5.dlgexternalpadding(0,0)
dlgvalue(RealNum5,StepL_X)

TagGroup label6 = DLGCreateLabel("  y:")
label6.dlgexternalpadding(1,1)
RealNum6 = DLGCreateRealField(0,7,2)
RealNum6.dlgexternalpadding(0,0)
DLGValue(RealNum6,StepL_Y)

TagGroup group3 = DLGGroupItems(label5, RealNum5, label6, RealNum6)
group3.DLGTableLayout(4, 1, 0);
box2_items.dlgaddelement(group3)
group3.dlgexternalpadding(0,3)

TagGroup label7 = DLGCreateLabel("7. Scanning tilt angle (degree):").dlgexternalpadding(1,1)
RealNum11 = DLGCreateRealField(0,7,3).dlgexternalpadding(0,0)
DLGValue(RealNum11,angleDegree)
box2_items.dlgaddelement(dlggroupitems(label7,RealNum11).dlgtablelayout(2,1,0),"","West")

//Scan options
Number defaultscan=0
ScanOption=DLGCreateCheckBox("Check this box to set an initial position",defaultscan)
TagGroup ScanLabel=DLGCreateLabel("   as the center of scanning area.   ")
ScanLabel.DLGExternalPadding(1,1)

/*
Number defaultcheckscan=0
CheckScan=DLGCreateCheckBox("Check Scan",defaultcheckscan)
*/

/*
TagGroup ScanOptionsGroup=DLGGroupItems(ScanOption, CheckScan)
ScanOptionsGroup.DLGTableLayout(2,1,0)
box2_items.dlgaddelement(ScanOptionsGroup)
ScanOptionsGroup.dlgexternalpadding(0,3)
*/

TagGroup ScanOptionsGroup=DLGGroupItems(ScanOption, ScanLabel)
ScanOptionsGroup.DLGTableLayout(1,2,0)
box2_items.dlgaddelement(ScanOptionsGroup)
ScanOptionsGroup.dlgexternalpadding(0,3)

//Start button
TagGroup StartButton = DLGCreatePushButton("  Start  ", "Start")
StartButton.dlgexternalpadding(5,5)
//Stop button
TagGroup StopButton = DLGCreatePushButton("  Stop  ", "Stop").dlgexternalpadding(5,5)
Box2_Items.DIGAddElement(DLGGroupItems(StartButton,StopButton).DLGTableLayout(2,1,0),"Center","")

Box2.DLGExternalPadding(10, 0)
Return Box2
}

// Creates the buttons in Control Box 2
// Control Box 3 starts here
TagGroup MainControlBox2()
{
    taggroup box3_items //Control box 3 is grouped by 'box3_items//
taggroup box3=dlgcreatebox(" Control Box 2 ", box3_items) // Label of 'Control Box 2'

String tagBase = ("SED_Calibration")
String Units
GetPersistentStringNote(TagBase + "CalUnits", units)
TagGroup label7 = DLGCreateLabel("Currently Calibrated Units: "+units)
box3_items.dlgaddelement(label7)

```

```

//Calibration button
TagGroup CalButton = DLGCreatePushButton(" Calibration ", "f_Cal").DLGSide("Center")
CalButton.dlgexternalpadding(72,5)
box3_items.dlgaddelement(CalButton)
Box3.DLGEExternalPadding(10,0)
return box3
}

taggroup MyInfo()
{
    taggroup MyInfo=dlgcreatelabel("Yu-Tsun Shao, MatSE, U of Illinois")
    MyInfo.dlgexternalpadding(5,5)
    return MyInfo
}

// Function to assemble the compenents of the dialog into the dialog frame
void DialogLibraryScanningED()
{
    // Configure the positioning in the top right of the application window

    TagGroup position;
    position = DLGBuildPositionFromApplication()
    position.TagGroupSetTagAs TagGroup( "Width", DLGBuildAutoSize() )
    position.TagGroupSetTagAs TagGroup( "Height", DLGBuildAutoSize() )
    position.TagGroupSetTagAs TagGroup( "X", DLGBuildRelativePosition( "Inside", 1 ) )
    position.TagGroupSetTagAs TagGroup( "Y", DLGBuildRelativePosition( "Inside", -1.0 ) )

    TagGroup dialog_items;
    TagGroup dialog = DLGCreateDialog("SED", dialog_items).dlgposition(position);

    // Call each button
    Dialog_Items.DLGAddElement(ScriptInfo())
    Dialog_Items.DLGAddElement(ExperimentalCondition())
    dialog_items.DLGAddElement(MainControlBox1())
    dialog_items.DLGAddElement(MainControlBox2())
    dialog_items.DLGAddElement(MyInfo())

    object dialog_thread = alloc(AcquThread)
    object dialog_frame = alloc(DialogLibraryTestClass4).init(dialog,dialog_thread.ScriptObjectGetID())
    dialog_frame.display("Scanning Electron NanoDiffraction (SEND)");
}

// Call the main function which creates and displays the dialog
DialogLibraryScanningED()

```

A.2. Symmetry quantification

```
/*
QSymm (Symmetry quantification)
Yu-Tsun Shao, Ph.D. Candidate, U of Illinois
```

This script is used to quantify the symmetry of CBED whole pattern using normalized cross-correlation. Some of the legacy functions from Dr. Kyou-Hyun Kim are used.

Usage:

1. circle annotations in an array of lattice; switch on/off indexing by pressing "T"
2. adjust circle positions interactively with "0", "g", "h", and arrow keys
3. adjust circle radius with "r", and "R"
4. calculate cross-correlation coefficient for mirror with "m"; rotational symmetry by pressing "2", "3", "4", "6"
5. press "space bar" to stop adjusting
6. Export annotations compatible with "Symm Quant." script initiated by Dr. K.-H. Kim

```
*/

number nint(number x) {
    number isign = 1
    if (x < 0) {
        isign = -1
        x = abs(x)
    }
    return isign*(x-mod(x,1))
}

number IsInBox(number x, number y, number xmin, number xmax, number ymin, number ymax) {
    if (x > xmin && x < xmax && y > ymin && y < ymax)
        return 1
    else
        return 0
}

void deleteovals(image img) {
    number anns, ann, type, n, i
    anns = CountAnnotations(img)
    n = anns
    i = 0
    while (n > 0)
    {
        ann = GetNthAnnotationID(img, i)
        type = AnnotationType(img,ann)
        if ((type == 6) || (type == 5) || (type == 13) || (type == 29))
        {
            DeleteAnnotation(img, ann)
        }
        else
        {
            i += 1
        }
        n -= 1
    }
}

void ROIInfo(number TopX, number TopY, number BotX, Number &CenX, Number &CenY, Number &Radius)
{
    Radius=abs(TopX-BotX)*0.5
    CenX=TopX+Radius
    CenY=TopY+Radius
}

number DegToRad(number Degree)
{
    Return (pi()/180)*Degree
}

number RadToAng(number Radian)
{
    Return (180/pi()*Radian)
}

number slope(number aX, number aY, number bX, number bY)
{
    Number Angle
    If(aY==bY)
    {
        Angle=0
    }
    Else If(aX==bX)
    {
        Angle=DegToRad(90)
    }
    ELSE
    {
        Number Slope=(bX-aX)/(bY-aY)
        If(Slope>0)
        {
            Angle=RadToAng(atan(slope))-90
        }
    }
}

```

```

        }
        Angle=RadToAng(atan(slope))+90
    }
    Angle=-DegToRad(Angle)
}
return Angle
}

Image Mask(image Template, number Bot, number Top, number xSize, number ySize, number Correction)
{
    Image Template:=ReallImage("", 4, xSize, ySize)
    Number Radius=abs((Bot-Top))*0.5
    Template=tert(iradius<Radius*Correction, 1, 0)
    return Template
}

Image Rotation(number ImgID, number TopY, number TopX, number BotY, number BotX, number rotation)
{
    Image Temporary:=GetImageFromID(ImgID)[TopY, TopX, BotY, BotX]
    Image TempR_A:=Rotate(Temporary, Rotation)
    ScrapCopy(TempR_A)
    Number Width, Height
    Number Radius=abs(BotX-TopX)*0.5
    Get2Dsize(TempR_A, Width, Height)
    //Width = TempR_A.ImageGetDimensionSize(0)
    //Height = TempR_A.ImageGetDimensionSize(1)
    Image TempR_B:=ReallImage("", 4, Width, Height)
    ScrapPaste(TempR_B)
    ScrapMerge(TempR_B)
    return TempR_B
}

// Cross-correlation coefficient calculation
Number XCorr(Image ImgA, Image ImgB, Image Mask, Number Pixels)
{
    Number Numer, Denom, NCC
    Number ImgAMean=sum(ImgA)/pixels
    Number ImgBMean=sum(ImgB)/pixels
    Numer=sum(((ImgA-ImgAMean)*(ImgB-ImgBMean))*Mask)
    Denom=sum(((ImgA-ImgAMean)*Mask)**2)*sum(((ImgB-ImgBMean)*Mask)**2)
    Denom=sqrt(Denom)
    NCC = Numer/Denom
    If (Denom == 0)
    {
        NCC=0
    }
    return NCC
}

// Crop Image function
Image ImageCrop(Image ResultImage, Number ROIradius, number CutOff)
{
    Image Temp
    Number Width, Height, Coeff=0
    Get2DSize(ResultImage, Width, Height)
    //Width = ResultImage.ImageGetDimensionSize(0)
    //Height = ResultImage.ImageGetDimensionSize(1)
    ScrapCopy(ResultImage[Height*0.5-ROIradius, Width*0.5-ROIradius, Height*0.5+ROIradius+Coeff, Width*0.5+ROIradius+Coeff])
    Temp:=ReallImage("", 4, 2*ROIradius+Coeff, 2*ROIradius+Coeff)
    ScrapPaste(Temp)
    ScrapMerge(Temp)
    return Temp
}

// creates an array of oval annotations
void DrawLattice(image front, Number x0, Number y0, Number gx, Number gy, Number hx, Number hy, Number r0, Number N_hkl, Number TextLabel)
{
    Number x, y, i, j, Nx, Ny, Mx, My, xx, yy, xsize, ysize
    GetSize(front,xsize,ysize)

    Number N_root
    N_root = SQRT(N_hkl)/2-mod(SQRT(N_hkl)/2,1)
    For (i=-N_root; i<N_root+1; i++)
    {
        For (j=-N_root; j<N_root+1; j++)
        {
            y=x0+i*gx+j*hx
            x=y0+i*gy+j*hy
            if (x<xsize || y<ysize)
            {
                front.CreateOvalAnnotation(x-r0,y-r0,x+r0,y+r0)
                if (TextLabel ==1)
                {
                    CreateTextAnnotation(front, x, y-r0, "(+i+","+(-j)+)") //top, left: label the order
                }
            }
        }
    }
}

// function to copy all annotations into a clone image
void CopyAnnotations(Image img, Image clonefront)

```

```

{
Number ncol, nrow, value=0
ImageDisplay Disp1, Disp2
Disp1 = Disp1 = img.ImageGetImageDisplay(0)
GetSize(img, ncol, nrow)
number AnnotN = CountAnnotations(img)
number i
for (i=0; i<AnnotN; i++)
{
Number AnnotID = GetNthAnnotationID(img,i)
number AnnotType=AnnotationType(img, AnnotID)
Number a,b,c,d
If (AnnotType == 6)
{
GetAnnotationRect(img, AnnotID, a,b,c,d)
CreateOvalAnnotation(clonefront, a, b, c, d)
}
Else If (AnnotType == 5)
{
GetAnnotationRect(img, AnnotID, a,b,c,d)
CreateBoxAnnotation(clonefront, a, b, c, d)
}
}
}

// Gauss ladder function
number gauss(number x) {
number isign = 1
if (x < 0) {
isign = -1
x = abs(x-1)
}
return isign*(x-mod(x,1))
}

//create circular ROI
ROI cs_CreateCircleROI(Number cx, Number cy, Number radius, Number points)
{
Number px, py, phi, count
ROI roi = NewRoi()
roi.ROISetName("CircleROI_r"+radius+"_p"+points) // name the ROI including creation paramters
If (points<3) points = Trunc(2*Pi()*radius / abs(points))+1 // calculate number of vertices on circle
points=max(points,3)
For (count=0; count<points; count++) // calculate vertices on circle
{
phi = count * 2*Pi()/points //points defines how smooth the ROI is
px = cx+radius*cos(phi)
py = cy+radius*sin(phi)
roi.ROIAddVertex(px,py)
}
pROI.ROISetIsClosed(1) // connect first with last vertex
return pROI
}

// A simple calculation to sort out the indexing (m,n) by computing the nearest integer
//(x,y)=(gx,hx),(gy,hy))X(m,n)
//(m,n)=A^-1*(hy,-hx),(gy,hy))X(disX,disY)
void GetCircleCoor(Number x0, Number y0, Number x, Number y, Number gx, Number gy, Number hx, Number hy, Number &m, Number &n)
{
Number disX=x-x0
Number disY=y-y0
Number detA=abs(gx*hy-gy*hx)
If (detA==0)
{
detA=1
}
m=(1/detA)*(hy*disX-hx*disY)
n=(1/detA)*(gx*disY-gy*disX)
m=gauss(m+0.5)
n=gauss(n+0.5)
}

//Determine mirror and counterpart
void Reflection(Number m, Number n, Number mX, Number mY, Number &m_prime, Number &n_prime)
{
If (mX==mY)
{
m_prime=n
n_prime=m
}
Else if (mY==0)
{
m_prime=m
n_prime=-n
}
Else if (mX==0)
{
m_prime=-m
n_prime=n
}
Else if (mX==mY)
{
m_prime=-n
}
}

```

```

n_prime=-m
}
Else
{
number angle
angle = abs(abs(slope(m,n,0,0))-abs(slope(mX,mY,0,0)))
m_prime = abs(m)*cos(2*angle)+abs(n)*sin(2*angle)
n_prime = abs(m)*sin(2*angle)-abs(n)*cos(2*angle)
m_prime = gauss(m_prime+0.5)
n_prime = gauss(n_prime+0.5)
}
}

// deletes the annotation outside of image
void DeleteOutBound(Image front)
{
Number i,n, N_markers=CountAnnotations(front)
number xsize = front.ImageGetDimensionSize(0)
number ysize = front.ImageGetDimensionSize(1)
n=N_markers
i=0
while (n>0)
{
number AnnotID=GetNthAnnotationID(front,i)
number A_AnnTy, A_AnnTx, A_AnnBy, A_AnnBx
GetAnnotationRect(front, AnnotID, A_AnnTy, A_AnnTx, A_AnnBy, A_AnnBx)
number A_CenterX, A_CenterY, RadiusA
ROIInfo(A_AnnTx, A_AnnTy, A_AnnBx, A_CenterX, A_CenterY, RadiusA)
If ((A_CenterX-RadiusA)<0)
{
DeleteAnnotation(front,AnnotID)
}
Else if ((A_CenterY-RadiusA)<0)
{
DeleteAnnotation(front,AnnotID)
}
Else if ((A_CenterY+RadiusA)>ysize)
{
DeleteAnnotation(front,AnnotID)
}
Else if ((A_CenterX+RadiusA)>xsize)
{
DeleteAnnotation(front,AnnotID)
}
Else
{
i+=1
}
}
n-=1
}
}

void All_ROItoMask(image front, image SavedID, image mask)
{
ImageDisplay disp
disp = front.ImageGetImageDisplay(0)
number N_markers=CountAnnotations(front)
number i, xsize, ysize
front.GetSize(xsize, ysize)
mask = 0
ROI tempROI
For (i=0; i<(N_markers); i++)
{
//function GetNthAnnotationID
number AnnotID=GetPixel(SavedID,0,i+0)
number AnnotType=AnnotationType(front, AnnotID)
If (AnnotType!=2)
{
number A_AnnTy, A_AnnTx, A_AnnBy, A_AnnBx
GetAnnotationRect(front, AnnotID, A_AnnTy, A_AnnTx, A_AnnBy, A_AnnBx)
number A_CenterX, A_CenterY, RadiusA
ROIInfo(A_AnnTx, A_AnnTy, A_AnnBx, A_CenterX, A_CenterY, RadiusA)
tempROI = cs_CreateCircleROI(A_CenterX,A_CenterY,RadiusA,-3)
disp.ImageDisplayAddRoi(tempROI)
//Result("n ID= "+AIDSID+", center_x= "+A_CenterX+", center_y= "+A_CenterY+", radius= "+RadiusA)
//put ROI into mask image
tempROI.ROIAddToMask(mask, 0, 0, xsize, ysize)
//delete temporary ROI
number tempROI_ID=GetNthAnnotationID(front,0)
DeleteAnnotation(front, tempROI_ID)
}
}
}

// An image that registers Annotation-ID for mirror counterparts
void MatchReflectionCircle(image front,image SavedID, image MirrorID, Number mX, Number mY, Number &Useful, Number Print)
{
number i, j, n,row, N_markers
i=0
row=0
N_markers=CountAnnotations(front)
For (i=0; i<(N_markers); i++) //N_markers = 0 then there's bug
{

```

```

number AnnotID = SavedID.GetPixel(0,i)
number AnnotType=AnnotationType(front, AnnotID)
number A_AnnTy, A_AnnTx, A_AnnBy, A_AnnBx
GetAnnotationRect(front, AnnotID, A_AnnTy, A_AnnTx, A_AnnBy, A_AnnBx)
number A_CenterX, A_CenterY, RadiusA
ROIInfo(A_AnnTx, A_AnnTy, A_AnnBx, A_CenterX, A_CenterY, RadiusA)
number m = SavedID.GetPixel(6,i)
number n = SavedID.GetPixel(7,i)
number m_prime, n_prime
Reflection(m,n,mX,mY,m_prime,n_prime)
For (j=0; j<(N_markers); j++)
{
//search for second set of circles
number AnnotID2 = SavedID.GetPixel(0,j)
number AnnotType2=AnnotationType(front, AnnotID2)
number A_AnnTy2, A_AnnTx2, A_AnnBy2, A_AnnBx2
GetAnnotationRect(front, AnnotID2, A_AnnTy2, A_AnnTx2, A_AnnBy2, A_AnnBx2)
number A_CenterX2, A_CenterY2, RadiusA2
ROIInfo(A_AnnTx2, A_AnnTy2, A_AnnBx2, A_CenterX2, A_CenterY2, RadiusA2)
number m2 = SavedID.GetPixel(6,j)
number n2 = SavedID.GetPixel(7,j)
//this causes problem if no counterpart in image i.e., (m2=n2=0, but not BF disc)
//delete un-matched circles
If ((m!=0) && (n!=0) && (m_prime==0) && (n_prime==0))
{
DeleteAnnotation(front,AnnotID)
}
Else If ((m2==m_prime) && (n2==n_prime) && (m2!=100000))
{
MirrorID.SetPixel(0,row+0,AnnotID)
MirrorID.SetPixel(1,row+0,A_CenterX)
MirrorID.SetPixel(2,row+0,A_CenterY)
MirrorID.SetPixel(3,row+0,m)
MirrorID.SetPixel(4,row+0,n)
MirrorID.SetPixel(5,row+0,AnnotID2)
MirrorID.SetPixel(6,row+0,A_CenterX2)
MirrorID.SetPixel(7,row+0,A_CenterY2)
MirrorID.SetPixel(8,row+0,m2)
MirrorID.SetPixel(9,row+0,n2)
row+=1
If (Print==1)
{
result("n #="+row)+"(m,n)="+m+" "+n+"),(m',n')="+m_prime+" "+n_prime+"),(m'',n'")="+m2+" "+n2+"")
}
}
}
Useful=row-1
If (Print==1)
{
result("n Total of "+(Useful)+" discs used for mirror quantification.")
}
}

//An image that registers Annotation-ID for convenience of tracing
void AnnotIDSave(image front, image SaveID, Number x0, Number y0, Number gx, Number gy, Number hx, Number hy, Number Print)
// (image with ROI, image to be saved)
{
number i, N_square, N_circle, N_markers=CountAnnotations(front)
For (i=0; i<(N_markers); i++)
{
//function GetNthAnnotationID
number AnnotID=GetNthAnnotationID(front,i)

//function AnnotationType
//5=box; 6=oval
number AnnotType=AnnotationType(front, AnnotID)
/*
If (AnnotType == 5)
{
AnnotType = 5
}
*/
number A_AnnTy, A_AnnTx, A_AnnBy, A_AnnBx
GetAnnotationRect(front, AnnotID, A_AnnTy, A_AnnTx, A_AnnBy, A_AnnBx)
number A_CenterX, A_CenterY, RadiusA
ROIInfo(A_AnnTx, A_AnnTy, A_AnnBx, A_CenterX, A_CenterY, RadiusA)
number m, n
GetCircleCoor(x0, y0, A_CenterX, A_CenterY, gx, gy, hx, hy, m, n)
//now save all values on image SaveID
SaveID.SetPixel(0, i+0, AnnotID) //for further Annot ID read-in
SaveID.SetPixel(1, i+0, AnnotType) //for further Annot Type read-in
SaveID.SetPixel(2, i+0, A_CenterX) //for further Annot x read-in
SaveID.SetPixel(3, i+0, A_CenterY) //for further Annot y read-in
SaveID.SetPixel(4, i+0, RadiusA) //for further Annot radius read-in
SaveID.SetPixel(5, i+0, i+1) //for further Annot ordering read-in
If (AnnotType==6)
{
SaveID.SetPixel(6, i+0, m) //for further Annot radius read-in
SaveID.SetPixel(7, i+0, n) //for further Annot radius read-in
}
}
Else

```



```

    {
    m=100000
    n=100000
    SaveID.SetPixel(6, i+0, m) //for further Annot radius read-in
    SaveID.SetPixel(7, i+0, n) //for further Annot radius read-in
    }
    If (Print==1)
    {
    Result("\n #"+(i+1)+" ID= "+AnnotID+", Annotation Type= "+AnnotType+", (x,y)= (" +A_CenterX+", "+A_CenterY+", ), radius= "+RadiusA+", (m,n)= (" +m+", "+n+")")
    }
    }
}

// Re-generate in the mirror order
//on the mirror plane: exclude (0,0);
//others: generate 2 sets
void Regenerate(Image front, Image MirrorID, Number Useful, Number RadiusA, Number Box)
{
DeleteOvals(front)
ImageDisplay disp
disp = front.ImageGetImageDisplay(0)
Image Panel:=ReallImage("Info", 4, 15, 200)
Number TempID, TempID2, TempID3
Number i, j, k, A_CenterX, A_CenterY, A_CenterX2, A_CenterY2, m,n,m2,n2, m3,n3
Number B_CenterX, B_CenterY, B_CenterX2, B_CenterY2
Useful+=1
j=0
Number BoxCount=0
ROI TempROI //for BF disc
//Box for mirror plane
For (i=0; i<Useful; i++)
{
A_CenterX=GetPixel(MirrorID, 1,i+0)
A_CenterY=GetPixel(MirrorID, 2,i+0)
A_CenterX2=GetPixel(MirrorID, 6,i+0)
A_CenterY2=GetPixel(MirrorID, 7,i+0)
m=GetPixel(MirrorID,3,i+0)
n=GetPixel(MirrorID,4,i+0)
m2=GetPixel(MirrorID,8,i+0)
n2=GetPixel(MirrorID,9,i+0)
Panel.SetPixel(0,i+0,m)
Panel.SetPixel(1,i+0,n)
Panel.SetPixel(2,i+0,m2)
Panel.SetPixel(3,i+0,n2)
If ((m==m2) && (n==n2))
{
If (Box==1)
{
CreateBoxAnnotation(Front, (A_CenterY-RadiusA), (A_CenterX-RadiusA), (A_CenterY+RadiusA), (A_CenterX+RadiusA))
}
Else
{
CreateOvalAnnotation(Front, (A_CenterY-RadiusA), (A_CenterX-RadiusA), (A_CenterY+RadiusA), (A_CenterX+RadiusA))
}
BoxCount++
}
If ((m==0) && (n==0) && (Box==1))
{
TempID=GetNthAnnotationID(front,0)
DeleteAnnotation(front, TempID)
BoxCount-=1
tempROI = cs_CreateCircleROI(A_CenterX,A_CenterY,RadiusA,-3)
disp.ImageDisplayAddRoi(tempROI)
}
}
Result("\n # of Boxes="+BoxCount)
If (mod(BoxCount,2)==1)
{
TempID=GetNthAnnotationID(front,0)
DeleteAnnotation(front, TempID)
}
}

//Circle for off-mirror plane
For (j=0; j<Useful; j++)
{
B_CenterX=GetPixel(MirrorID, 1,j+0)
B_CenterY=GetPixel(MirrorID, 2,j+0)
B_CenterX2=GetPixel(MirrorID, 6,j+0)
B_CenterY2=GetPixel(MirrorID, 7,j+0)
m=GetPixel(MirrorID,3,j+0)
n=GetPixel(MirrorID,4,j+0)
m2=GetPixel(MirrorID,8,j+0)
n2=GetPixel(MirrorID,9,j+0)
Panel.SetPixel(0,j+0,m)
Panel.SetPixel(1,j+0,n)
Panel.SetPixel(2,j+0,m2)
Panel.SetPixel(3,j+0,n2)
If ((m!=m2) || (n!=n2))
{
CreateOvalAnnotation(Front, (B_CenterY-RadiusA), (B_CenterX-RadiusA), (B_CenterY+RadiusA), (B_CenterX+RadiusA))
CreateOvalAnnotation(Front, (B_CenterY2-RadiusA), (B_CenterX2-RadiusA), (B_CenterY2+RadiusA), (B_CenterX2+RadiusA))
}
}
For (k=0; k<j; k++)

```

```

{
  m3=Panel.GetPixel(2,k+0)
  n3=Panel.GetPixel(3,k+0)
  If ((m==m3) && (n==n3))
  {
    TempID2=GetNthAnnotationID(front,0)
    TempID3=GetNthAnnotationID(front,1)
    DeleteAnnotation(front,TempID2)
    DeleteAnnotation(front,TempID3)
  }
}
}
}

// Calculate weighted cross-correlation of Mirror
Number Gamma(Image front, Number Delete)
{
  //Get image info
  ImageDisplay ImgDisp = front.ImageGetImageDisplay(0)
  Number xsize = front.ImageGetDimensionSize(0)
  Number ysize = front.ImageGetDimensionSize(1)

  //Temporary scrap image for rotate , mask & crosscorrelate
  Image TempScrap:=ReallImage("Temp Scrap", 4, xsize, ysize)
  TempScrap=ImgDisp.ImageDisplayGetDisplayedImage()
  Number ImageID=GetImageID(TempScrap)

  // Register IDs
  // Assign annotations' IDs to AnnotA and AnnotB
  Image AnnotIDSave:=ReallImage("Pair Info", 4, 10, 200)
  Image AnnotIDSave2:=ReallImage("Mirror Plane Info", 4, 10, 200)
  Number SetsCount=0
  Number Sets=1
  Number SetTemp
  Number Row=0, Row2=0, i=0, ix=0
  Number NoOfAnnot=CountAnnotations(front), TempAnnotID, TypeOfAnnot
  Number AnnotA,A_AnnTy,A_AnnTx,A_AnnBy,A_AnnBx,A_CenterX,A_CenterY,RadiusA
  Number AnnotB,B_AnnTy,B_AnnTx,B_AnnBy,B_AnnBx,B_CenterX,B_CenterY,RadiusB

  While (i<NoOfAnnot)
  {
    TempAnnotID=GetNthAnnotationID(Front, i)
    TypeOfAnnot=AnnotationType(Front, TempAnnotID)
    If (TypeOfAnnot==5||TypeOfAnnot==6)
    {
      If (TypeOfAnnot==6)
      {
        AnnotIDSave.SetPixel(0, row, TempAnnotID)
        row++
      }
      If (TypeOfAnnot==5)
      {
        AnnotIDSave2.SetPixel(0, row2, TempAnnotID)
        row2++
        ix++
      }
      i++
      Sets++
    }
    Else
    {
      i++
    }
  }
  Sets=(Sets-1)/2+0.5*ix
  Result("\n>"+Sets+" set(s) selected")
  Result("\n>"+ix+" discs are placed on the mirror plane")

  //Some values for calculations
  number CrossCorrelationCoeff=0
  number TotalIntensity=0
  number Temp_CrossCorrelation=0
  Number SetsCountB=0
  Number RotAngleTemp, RotAngle
  Number nxx=0, nyy=0
  Result("\n\n          X-corr          r-Factor          Intensity Sum")

  While (SetsCount<Sets) //*****
  {
    // Allocate annotations' IDs and get annotations' info

    If (SetsCount<(Sets-ix))
    {
      AnnotA=AnnotIDSave.GetPixel(0, SetsCount*2+1)
      AnnotB=AnnotIDSave.GetPixel(0, SetsCount*2)
      GetAnnotationRect(Front, AnnotA, A_AnnTy, A_AnnTx, A_AnnBy, A_AnnBx)
      GetAnnotationRect(Front, AnnotB, B_AnnTy, B_AnnTx, B_AnnBy, B_AnnBx)

      //Calculate Radius & Rotation Angle
      ROIInfo(A_AnnTx, A_AnnTy, A_AnnBx, A_CenterX, A_CenterY, RadiusA)
      ROIInfo(B_AnnTx, B_AnnTy, B_AnnBx, B_CenterX, B_CenterY, RadiusB)
      If (RadiusA!=RadiusB)

```

```

    {
        B_AnnTx=B_centerX-RadiusA
        B_AnnTy=B_centerY-RadiusA
        B_AnnBx=B_centerX+RadiusA
        B_AnnBy=B_centerY+RadiusA
    }
    //CreateTextAnnotation(Front, A_CenterY, A_CenterX, "A"+(SetsCount+1))
    //CreateTextAnnotation(Front, B_CenterY, B_CenterX, "B"+(SetsCount+1))
    RotAngle=slope(A_CenterX, A_CenterY, B_CenterX, B_CenterY)
    /*
        Result ("\n\nRotation angle="+Rad2Ang(RotAngle)+"\n")
    */
}
If (SetsCount>=(Sets-ix))
{
    If (nxx<1) //nx used to calculate rotation angle of disc lied on the mirror axis for one time
    {
        AnnotA=AnnotIDSave2.GetPixel(0, SetsCountB+1)
        AnnotB=AnnotIDSave2.GetPixel(0, SetsCountB)
        GetAnnotationRect(Front, AnnotA, A_AnnTy, A_AnnTx, A_AnnBy, A_AnnBx)
        GetAnnotationRect(Front, AnnotB, B_AnnTy, B_AnnTx, B_AnnBy, B_AnnBx)
        ROIInfo(A_AnnTx, A_AnnTy, A_AnnBx, A_CenterX, A_CenterY, RadiusA)
        ROIInfo(B_AnnTx, B_AnnTy, B_AnnBx, B_CenterX, B_CenterY, RadiusB)
        If (RadiusA!=RadiusB)
        {
            B_AnnTx=B_centerX-RadiusA
            B_AnnTy=B_centerY-RadiusA
            B_AnnBx=B_centerX+RadiusA
            B_AnnBy=B_centerY+RadiusA
        }
        //CreateTextAnnotation(Front, A_CenterY, A_CenterX, "m"+(SetsCountB+2))
        //CreateTextAnnotation(Front, B_CenterY, B_CenterX, "m"+(SetsCountB+1))
        RotAngleTemp=slope(A_CenterX, A_CenterY, B_CenterX, B_CenterY) //Calculate rotation angle first
        SetsCountB=SetsCountB+2
    }
}
Image Temp_A, Temp_B, TempMask
Image TempAAA, TempBBB
Number xWidth, yHeight
// Mirror symmetry
If (SetsCount>=(Sets-ix))
{
    TempAAA=Rotation(ImageID, A_AnnTy, A_AnnTx, A_AnnBy, A_AnnBx, RotAngleTemp)
    TempBBB=Rotation(ImageID, B_AnnTy, B_AnnTx, B_AnnBy, B_AnnBx, RotAngleTemp)
    If (nyy==0)
    {
        Temp_A=TempBBB //I switched the order of TempAAA & TempBBB s.t. the indices in both "image"&"result" the same
        Temp_B=TempBBB
        nxx++
        nyy++
    }
    Else If (nyy==1)
    {
        Temp_A=TempAAA
        Temp_B=TempAAA
        nyy=0
        nxx=0
    }
}
Else
{
    /*
        Result("\n"+A_AnnTy+" "+A_AnnTx+" "+A_AnnBy+" "+A_AnnBx)
        Result("\n"+B_AnnTy+" "+B_AnnTx+" "+B_AnnBy+" "+B_AnnBx)
    */
    Temp_A=Rotation(ImageID, A_AnnTy, A_AnnTx, A_AnnBy, A_AnnBx, RotAngle)
    Temp_B=Rotation(ImageID, B_AnnTy, B_AnnTx, B_AnnBy, B_AnnBx, RotAngle)
}

//Create a mask
Get2Dsize(Temp_A, xWidth, yHeight)
//xWidth = Temp_A.ImageGetDimensionSize(0)
//yHeight = Temp_A.ImageGetDimensionSize(1)
TempMask=Mask(TempMask, A_AnnBx, A_AnnTx, xWidth, yHeight, 0.9)
Number NoOfPixels=sum(TempMask) //Calculate a number of pixels inside the created mask (to be used for quantification)

// Generate Mask Image -> generate mirror image -> apply
//(4) Mask x Image
Temp_A=Temp_A*TempMask

Image Temp_AA, Temp_BB, FlipTemp
If (SetsCount>=(Sets-ix))
{
    Temp_A.SetName("aligned m_Set "+(SetsCount+1))
    FlipVertical(Temp_B)
    Temp_B=Temp_B*TempMask
    Temp_B.SetName("mirror applied_Set "+(SetsCount+1))
}
Else
{
    Temp_A.SetName("aligned A_Set "+(SetsCount+1))
    FlipHorizontal(Temp_B)
}
/*

```

```

Temp_A.ShowImage()
Temp_B.ShowImage()
TempMask.ShowImage()
*/
Temp_B=Temp_B*TempMask
Temp_B.SetName("symm applied B_set "+(SetsCount+1))
Temp_BB=Temp_B
FlipHorizontal(Temp_BB)
Temp_BB.SetName("aligned B_set "+(SetsCount+1))
}
// Cross-correlation coefficient
Number Temp_XCross=XCorr(Temp_A, Temp_B, TempMask, NoOfPixels)
//Sum of intensity of discs, for weighted gamma use
Number IntensityA, IntensityB, IntensityAB
IntensityA=sum(Temp_A*TempMask)
IntensityB=sum(Temp_B*TempMask)
IntensityAB=(IntensityA+IntensityB)/2
Temp_A.DeleteImage()
Temp_B.DeleteImage()
//Return values
If (SetsCount<=(Sets-ix))
{
Result("\nSet "+(SetsCount+1)+" "+" "+Temp_XCross+" "+IntensityAB)
}
Else
{
Result("\nSet "+"m"+(SetsCount-(Sets-ix)+1)+" "+Temp_XCross+" "+IntensityAB)
}
CrossCorrelationCoeff=CrossCorrelationCoeff+Temp_XCross
//numerator
Temp_CrossCorrelation=Temp_CrossCorrelation+Temp_XCross*IntensityAB
//denominator
TotalIntensity=TotalIntensity+IntensityAB

SetsCount++
}
Result("\n\nWeight "+Temp_CrossCorrelation/TotalIntensity)
If (Delete==1)
{
DeleteOvals(front)
}

return RotAngleTemp
}

//Rotational Symmetry
void TwoFold(Number m, Number n, Number &m_prime, Number &n_prime)
{
m_prime=-m
n_prime=-n
}

void FourFold(Number m, Number n, Number &m2, Number &n2, Number &m3, Number &n3, Number &m4, Number &n4)
{
m2=-n
n2=m
m3=-m
n3=-n
m4=n
n4=-m
}

void SixFold(Number angle, Number m, Number n, Number &m2, Number &n2, Number &m3, Number &n3, Number &m4, Number &n4, Number &m5, Number
&n5, Number &m6, Number &n6)
{
//depends on how one drew the g, h lines
If (angle==1) // acute angle
{
m3=n
n3=-(m+n)
}
Else if (angle==0) // blunt angle
{
m3=-m
n3=-n
}
m2=m+m3
n2=n+n3
m4=-m
n4=-n
m5=-m2
n5=-n2
m6=-m3
n6=-n3
}

void MatchTwoFold(image front,image SavedID, image TwoFoldID, Number &Useful, Number Print)
{
number i, j, row, N_markers=CountAnnotations(front)
i=0
j=0
row=0
For (i=0; i<N_markers; i++)

```

```

{
number AnnotID = SavedID.GetPixel(0,i)
number AnnotType=AnnotationType(front, AnnotID)
number A_AnnTy, A_AnnTx, A_AnnBy, A_AnnBx
GetAnnotationRect(front, AnnotID, A_AnnTy, A_AnnTx, A_AnnBy, A_AnnBx)
number A_CenterX, A_CenterY, RadiusA
ROInfo(A_AnnTx, A_AnnTy, A_AnnBx, A_CenterX, A_CenterY, RadiusA)
number m = SavedID.GetPixel(6,i)
number n = SavedID.GetPixel(7,i)
number m_prime, n_prime
TwoFold(m,n,m_prime,n_prime)
For (j=0; j<(N_markers); j++)
{
//search for second set of circles
number AnnotID2 = SavedID.GetPixel(0,j)
number AnnotType2=AnnotationType(front, AnnotID2)
number A_AnnTy2, A_AnnTx2, A_AnnBy2, A_AnnBx2
GetAnnotationRect(front, AnnotID2, A_AnnTy2, A_AnnTx2, A_AnnBy2, A_AnnBx2)
number A_CenterX2, A_CenterY2, RadiusA2
ROInfo(A_AnnTx2, A_AnnTy2, A_AnnBx2, A_CenterX2, A_CenterY2, RadiusA2)
number m2 = SavedID.GetPixel(6,j)
number n2 = SavedID.GetPixel(7,j)
If ((m!=0) && (n!=0) && (m_prime==0) && (n_prime==0))
{
DeleteAnnotation(front,AnnotID)
}
Else If ((m2==m_prime) && (n2==n_prime) && (m2!=100000))
{
TwoFoldID.SetPixel(0,row+0,AnnotID)
TwoFoldID.SetPixel(1,row+0,A_CenterX)
TwoFoldID.SetPixel(2,row+0,A_CenterY)
TwoFoldID.SetPixel(3,row+0,m)
TwoFoldID.SetPixel(4,row+0,n)
TwoFoldID.SetPixel(5,row+0,AnnotID2)
TwoFoldID.SetPixel(6,row+0,A_CenterX2)
TwoFoldID.SetPixel(7,row+0,A_CenterY2)
TwoFoldID.SetPixel(8,row+0,m2)
TwoFoldID.SetPixel(9,row+0,n2)
row+=1
If (Print==1)
{
result("\n #="+row)+"(m,n)="+m+", "+n+",(m',n')="+m_prime+", "+n_prime+",(m'',n'')="+m2+", "+n2+"")
}
}
}
Useful=row
If (Print==1)
{
result("\n Total of "+Useful+" discs used for 2-fold quantification.")
}
}

//Match the 4R circles
void FourR(image front, image SavedID, image FourFoldID, Number &Useful, Number Print)
{
image Temp:=ReallImage("Certified 4R", 4, 15, 2000)
number i, j, N_markers=CountAnnotations(front)
i=0
j=0
number set = 0
//1st loop: use image Temp to record all the circles
// who has their full 4R counterparts
For (i=0; i<N_markers; i++)
{
number AnnotID = SavedID.GetPixel(0,i)
number AnnotType=AnnotationType(front, AnnotID)
number A_CenterX, A_CenterY, RadiusA
A_CenterX = SavedID.GetPixel(2,i)
A_CenterY = SavedID.GetPixel(3,i)
number m = SavedID.GetPixel(6,i)
number n = SavedID.GetPixel(7,i)
number m2, n2, m3, n3, m4, n4, m_dummy, n_dummy
FourFold(m,n,m2,n2,m3,n3,m4,n4)
number count=0
For (j=0; j<(N_markers); j++)
{
//search for following sets of circles
number AnnotID2 = SavedID.GetPixel(0,j)
number AnnotType2=AnnotationType(front, AnnotID2)
number A_CenterX2, A_CenterY2, RadiusA2
A_CenterX2 = SavedID.GetPixel(2,j)
A_CenterY2 = SavedID.GetPixel(3,j)
number m_dummy = SavedID.GetPixel(6,j)
number n_dummy = SavedID.GetPixel(7,j)
If ((m!=0) && (n!=0) && (m2==0) && (n2==0) && (m3==0) && (n3==0) && (m4==0) && (n4==0))
{
DeleteAnnotation(front,AnnotID)
}
Else if (m_dummy == m2 && n_dummy == n2)
{
count+=1
}
}
}
}

```

```

}
Else if (m_dummy == m3 && n_dummy == n3)
{
count+=1
}
Else if (m_dummy == m4 && n_dummy == n4)
{
count+=1
}
}
If (count==3)
{
Temp.SetPixel(0,0+set,AnnotID)
Temp.SetPixel(1,0+set,m)
Temp.SetPixel(2,0+set,n)
Temp.SetPixel(3,0+set,A_CenterX)
Temp.SetPixel(4,0+set,A_CenterY)
set++
}
}
}

// 2nd-loop
// read image Temp and writes in the image FourFoldID
// with (m,n) & (m2,n2) s.t. it'll be easier to re-generate
For (i=0; i<set; i++)
{
number m2,n2,m3,n3,m4,n4
number AnnotID = Temp.GetPixel(0,i)
number m = Temp.GetPixel(1,i)
number n = Temp.GetPixel(2,i)
number A_CenterX = Temp.GetPixel(3,i)
number A_CenterY = Temp.GetPixel(4,i)
FourFold(m,n,m2,n2,m3,n3,m4,n4)
For (j=0; j<set; j++)
{
number AnnotID2 = Temp.GetPixel(0,j)
number m_pr = Temp.GetPixel(1,j)
number n_pr = Temp.GetPixel(2,j)
number A_CenterX2 = Temp.GetPixel(3,j)
number A_CenterY2 = Temp.GetPixel(4,j)
If (m_pr == m4 && n_pr == n4)
{
FourFoldID.SetPixel(0,j+0,AnnotID)
FourFoldID.SetPixel(1,j+0,m)
FourFoldID.SetPixel(2,j+0,n)
FourFoldID.SetPixel(3,j+0,A_CenterX)
FourFoldID.SetPixel(4,j+0,A_CenterY)
FourFoldID.SetPixel(5,j+0,AnnotID2)
FourFoldID.SetPixel(6,j+0,m_pr)
FourFoldID.SetPixel(7,j+0,n_pr)
FourFoldID.SetPixel(8,j+0,A_CenterX2)
FourFoldID.SetPixel(9,j+0,A_CenterY2)
If (print==1)
{
result("\n 2 neighboring 4R-certified circles: (m,n)=(\"+m+\",\"+n+\"),(m2,n2)=(\"+m_pr+\",\"+n_pr+)\")
}
}
}
}
}
Useful = set
}

//Match the 6R circles up to 20 circles (2016. April. 28th)
void SixR(image front, image SavedID, image SixFoldID, Number angle, Number Select, Number &Useful, Number Print)
{
image Temp:=ReallImage("Certified 6R", 4, 15, 2000)
number i, j, N_markers=CountAnnotations(front)
i=0
j=0
number set = 0
//1st loop: use image Temp to record all the circles
// who has their full 6R counterparts
For (i=0; i<N_markers; i++)
{
number AnnotID = SavedID.GetPixel(0,i)
number AnnotType=AnnotationType(front, AnnotID)
number A_CenterX, A_CenterY, RadiusA
A_CenterX = SavedID.GetPixel(2,i)
A_CenterY = SavedID.GetPixel(3,i)
number m = SavedID.GetPixel(6,i)
number n = SavedID.GetPixel(7,i)
number m2, n2, m3, n3, m4, n4, m5, n5, m6, n6, m_dummy, n_dummy
SixFold(angle, m, n, m2, n2, m3, n3, m4, n4, m5, n5, m6, n6)
number count=0
For (j=0; j<(N_markers); j++)
{
//search for following sets of circles
number AnnotID2 = SavedID.GetPixel(0,j)
number AnnotType2=AnnotationType(front, AnnotID2)
number A_CenterX2, A_CenterY2, RadiusA2
A_CenterX2 = SavedID.GetPixel(2,j)
A_CenterY2 = SavedID.GetPixel(3,j)
number m_dummy = SavedID.GetPixel(6,j)

```

```

number n_dummy = SavedID.GetPixel(7,j)
If ((m!=0) && (n!=0) && (m2==0) && (n2==0) && (m3==0) && (n3==0) && (m4==0) && (n4==0) && (m5==0) && (n5==0) && (m6==0) && (n6==0))
{
DeleteAnnotation(front,AnnotID)
}
Else if (m_dummy == m2 && n_dummy == n2)
{
count+=1
}
Else if (m_dummy == m3 && n_dummy == n3)
{
count+=1
}
Else if (m_dummy == m4 && n_dummy == n4)
{
count+=1
}
Else if (m_dummy == m5 && n_dummy == n5)
{
count+=1
}
Else if (m_dummy == m6 && n_dummy == n6)
{
count+=1
}
}
If (count==5)
{
Temp.SetPixel(0,0+set,AnnotID)
Temp.SetPixel(1,0+set,m)
Temp.SetPixel(2,0+set,n)
Temp.SetPixel(3,0+set,A_CenterX)
Temp.SetPixel(4,0+set,A_CenterY)
set++
}
}

For (i=0; i<set; i++)
{
number AnnotID = Temp.GetPixel(0,i)
number m = Temp.GetPixel(1,i)
number n = Temp.GetPixel(2,i)
number A_CenterX = Temp.GetPixel(3,i)
number A_CenterY = Temp.GetPixel(4,i)
Number m_select, n_select,m2,n2,m3,n3,m4,n4,m5,n5,m6,n6
SixFold(angle,m,n,m2,n2,m3,n3,m4,n4,m5,n5,m6,n6)
// This is where we distinguish 3R & 6R
If (Select==6)
{
If (angle==1)
{
m_select=m2
n_select=n2
}
Else if (angle==0)
{
m_select=m6
n_select=n6
}
}
Else if (Select==3) //3R
{
If (angle==1)
{
m_select=m3
n_select=n3
}
Else if (angle==0)
{
m_select=m5
n_select=n5
}
}
}
//result("\n m_select,n_select="+m_select+","+n_select+")
For (j=0; j<set; j++)
{
number AnnotID2 = Temp.GetPixel(0,j)
number m_pr = Temp.GetPixel(1,j)
number n_pr = Temp.GetPixel(2,j)
number A_CenterX2 = Temp.GetPixel(3,j)
number A_CenterY2 = Temp.GetPixel(4,j)
If (m_pr == m_select && n_pr == n_select)
{
SixFoldID.SetPixel(0,j+0,AnnotID)
SixFoldID.SetPixel(1,j+0,m)
SixFoldID.SetPixel(2,j+0,n)
SixFoldID.SetPixel(3,j+0,A_CenterX)
SixFoldID.SetPixel(4,j+0,A_CenterY)
SixFoldID.SetPixel(5,j+0,AnnotID2)
SixFoldID.SetPixel(6,j+0,m_pr)
SixFoldID.SetPixel(7,j+0,n_pr)
SixFoldID.SetPixel(8,j+0,A_CenterX2)
SixFoldID.SetPixel(9,j+0,A_CenterY2)
}
}
}

```

```

    If (print==1)
    {
        result("\n 2 neighboring 6R-certified circles: (m,n)=(\"+m+\",\"+n+\"),(m2,n2)=(\"+m_pr+\",\"+n_pr+\")")
    }
}
}
Useful = set
}

void TwoFoldRegenerate(Image front, Image TwoFoldID, Number Useful, Number RadiusA)
{
    DeleteOvals(front)
    ImageDisplay disp
    disp = front.Image.GetImageDisplay(0)
    Image Panel:=ReallImage("Info", 4, 15, 2000)
    Number TempID, TempID2, TempID3
    Number i, j, k, A_CenterX, A_CenterY, A_CenterX2, A_CenterY2, m,n,m2,n2, m3,n3
    Number B_CenterX, B_CenterY, B_CenterX2, B_CenterY2
    j=0

    //delete BF disc; not useful for QSymm
    For (i=0; i<Useful; i++)
    {
        A_CenterX=GetPixel(TwoFoldID, 1,i+0)
        A_CenterY=GetPixel(TwoFoldID, 2,i+0)
        A_CenterX2=GetPixel(TwoFoldID, 6,i+0)
        A_CenterY2=GetPixel(TwoFoldID, 7,i+0)
        m=GetPixel(TwoFoldID,3,i+0)
        n=GetPixel(TwoFoldID,4,i+0)
        m2=GetPixel(TwoFoldID,8,i+0)
        n2=GetPixel(TwoFoldID,9,i+0)
        TempID=GetNthAnnotationID(front,0)
        number TempType=AnnotationType(front,TempID)
        If (TempType == 6)
        {
            {
                If ((m==0) && (n==0))
                {
                    DeleteAnnotation(front, TempID)
                }
            }
        }
    }
    //other than BF disc
    For (j=0; j<Useful; j++)
    {
        B_CenterX=GetPixel(TwoFoldID, 1,j+0)
        B_CenterY=GetPixel(TwoFoldID, 2,j+0)
        B_CenterX2=GetPixel(TwoFoldID, 6,j+0)
        B_CenterY2=GetPixel(TwoFoldID, 7,j+0)
        m=GetPixel(TwoFoldID,3,j+0)
        n=GetPixel(TwoFoldID,4,j+0)
        m2=GetPixel(TwoFoldID,8,j+0)
        n2=GetPixel(TwoFoldID,9,j+0)
        Panel.SetPixel(0,j+0,m)
        Panel.SetPixel(1,j+0,n)
        Panel.SetPixel(2,j+0,m2)
        Panel.SetPixel(3,j+0,n2)
        If ((m!=m2) || (n!=n2))
        {
            CreateOvalAnnotation(Front, (B_CenterY-RadiusA), (B_CenterX-RadiusA), (B_CenterY+RadiusA), (B_CenterX+RadiusA))
            CreateOvalAnnotation(Front, (B_CenterY2-RadiusA), (B_CenterX2-RadiusA), (B_CenterY2+RadiusA), (B_CenterX2+RadiusA))
        }
        For (k=0; k<j; k++)
        {
            m3=Panel.GetPixel(2,k+0)
            n3=Panel.GetPixel(3,k+0)
            If ((m==m3) && (n==n3))
            {
                TempID2=GetNthAnnotationID(front,0)
                TempID3=GetNthAnnotationID(front,1)
                DeleteAnnotation(front,TempID2)
                DeleteAnnotation(front,TempID3)
            }
        }
    }
}

void FourFoldRegenerate(image front, image FourFoldID, Number Useful, Number RadiusA)
{
    DeleteOvals(front)
    ImageDisplay disp
    disp = front.Image.GetImageDisplay(0)
    Image Panel:=ReallImage("Info", 4, 15, 2000)
    Number TempID, TempID2, TempID3
    Number i, j, k, A_CenterX, A_CenterY, A_CenterX2, A_CenterY2, m,n,m2,n2, m3,n3
    Number B_CenterX, B_CenterY, B_CenterX2, B_CenterY2
    j=0

    For (i=0; i<(Useful); i++)
    {
        A_CenterX=GetPixel(FourFoldID, 3,i+0)
        A_CenterY=GetPixel(FourFoldID, 4,i+0)
        A_CenterX2=GetPixel(FourFoldID, 8,i+0)

```



```

A_CenterY2=GetPixel(FourFoldID, 9,i+0)
m=GetPixel(FourFoldID,1,i+0)
n=GetPixel(FourFoldID,2,i+0)
m2=GetPixel(FourFoldID,6,i+0)
n2=GetPixel(FourFoldID,7,i+0)
TempID=GetNthAnnotationID(front,0)
number TempType=AnnotationType(front,TempID)
If (TempType == 6)
{
  If ((m==0) && (n==0))
  {
    DeleteAnnotation(front, TempID)
  }
}
}
For (j=0; j<(Useful); j++)
{
  B_CenterX = FourFoldID.GetPixel(3,j+0)
  B_CenterY = FourFoldID.GetPixel(4,j+0)
  B_CenterX2 = FourFoldID.GetPixel(8,j+0)
  B_CenterY2 = FourFoldID.GetPixel(9,j+0)
  If (B_CenterX!=0 && B_CenterY!=0 && B_CenterX2!=0 && B_CenterY2!=0)
  {
    CreateOvalAnnotation(Front, (B_CenterY-RadiusA), (B_CenterX-RadiusA), (B_CenterY+RadiusA), (B_CenterX+RadiusA))
    CreateOvalAnnotation(Front, (B_CenterY2-RadiusA), (B_CenterX2-RadiusA), (B_CenterY2+RadiusA), (B_CenterX2+RadiusA))
  }
}
}

void SixFoldRegenerate(image front, image SixFoldID, Number Useful, Number RadiusA)
{
  DeleteOvals(front)
  ImageDisplay disp
  disp = front.ImageGetImageDisplay(0)
  Image Panel:=RealImage("Info", 4, 15, 2000)
  Number TempID, TempID2, TempID3
  Number i, j, k, A_CenterX, A_CenterY, A_CenterX2, A_CenterY2, m,n,m2,n2, m3,n3
  Number B_CenterX, B_CenterY, B_CenterX2, B_CenterY2
  j=0
  For (i=0; i<(Useful); i++)
  {
    A_CenterX=GetPixel(SixFoldID, 3,i+0)
    A_CenterY=GetPixel(SixFoldID, 4,i+0)
    A_CenterX2=GetPixel(SixFoldID, 8,i+0)
    A_CenterY2=GetPixel(SixFoldID, 9,i+0)
    m=GetPixel(SixFoldID,1,i+0)
    n=GetPixel(SixFoldID,2,i+0)
    m2=GetPixel(SixFoldID,6,i+0)
    n2=GetPixel(SixFoldID,7,i+0)
    TempID=GetNthAnnotationID(front,0)
    number TempType=AnnotationType(front,TempID)
    If (TempType == 6)
    {
      If ((m==0) && (n==0))
      {
        DeleteAnnotation(front, TempID)
      }
    }
  }
}
For (j=0; j<(Useful); j++)
{
  B_CenterX = SixFoldID.GetPixel(3,j+0)
  B_CenterY = SixFoldID.GetPixel(4,j+0)
  B_CenterX2 = SixFoldID.GetPixel(8,j+0)
  B_CenterY2 = SixFoldID.GetPixel(9,j+0)
  If (B_CenterX!=0 && B_CenterY!=0 && B_CenterX2!=0 && B_CenterY2!=0)
  {
    CreateOvalAnnotation(Front, (B_CenterY-RadiusA), (B_CenterX-RadiusA), (B_CenterY+RadiusA), (B_CenterX+RadiusA))
    CreateOvalAnnotation(Front, (B_CenterY2-RadiusA), (B_CenterX2-RadiusA), (B_CenterY2+RadiusA), (B_CenterX2+RadiusA))
  }
}
}

// Calculate weighted cross-correlation of 2R,4R
void GammaRotate(Image front, Number Delete, Number RotateSelect)
{
  //Get image info
  ImageDisplay ImgDisp = front.ImageGetImageDisplay(0)
  Number xsize = front.ImageGetDimensionSize(0)
  Number ysize = front.ImageGetDimensionSize(1)

  //Temporary scrap image for rotate , mask & crosscorrelate
  Image TempScrap:=RealImage("Temp Scrap", 4, xsize, ysize)
  TempScrap=ImgDisp.ImageDisplayGetDisplayedImage()
  Number ImageID=GetImageID(TempScrap)

  // Register IDs
  // Assign annotations' IDs to AnnotA and AnnotB
  Image AnnotIDSave:=RealImage("Pair Info", 4, 40, 2000)
  Image AnnotIDSave2:=RealImage("Mirror Plane Info", 4, 40, 2000)
  Number SetsCount=0
  Number Sets=1
  Number SetTemp

```

```

Number Row=0, Row2=0, i=0, ix=0
Number NoOfAnnot=CountAnnotations(front, TempAnnotID, TypeOfAnnot
Number AnnotA,A_AnnTy,A_AnnTx,A_AnnBy,A_AnnBx,A_CenterX,A_CenterY,RadiusA
Number AnnotB,B_AnnTy,B_AnnTx,B_AnnBy,B_AnnBx,B_CenterX,B_CenterY,RadiusB

While (i<NoOfAnnot)
{
TempAnnotID=GetNthAnnotationID(Front, i)
TypeOfAnnot=AnnotationType(Front, TempAnnotID)
If (TypeOfAnnot==5||TypeOfAnnot==6)
{
If (TypeOfAnnot==6)
{
AnnotIDSave.SetPixel(0, row, TempAnnotID)
row++
}
If (TypeOfAnnot==5)
{
AnnotIDSave2.SetPixel(0, row2, TempAnnotID)
row2++
ix++
}
i++
Sets++
}
Else
{
i++
}
}
Sets=(Sets-1)/2+0.5*ix
Result("\n>"+Sets+" set(s) selected")
Result("\n>"+ix+" discs are placed on the mirror plane")

//Some values for calculations
number CrossCorrelationCoeff=0
number TotalIntensity=0
number Temp_CrossCorrelation=0
Number SetsCountB=0
Number RotAngleTemp, RotAngle
Number nxx=0, nyy=0
Result("\n\n X-corr          r-Factor    Intensity Sum")
While (SetsCount<Sets)
{
// Allocate annotations' IDs and get annotations' info
If (SetsCount<-(Sets-ix))
{
AnnotA=AnnotIDSave.GetPixel(0, SetsCount*2+1)
AnnotB=AnnotIDSave2.GetPixel(0, SetsCount*2)
GetAnnotationRect(Front, AnnotA, A_AnnTy, A_AnnTx, A_AnnBy, A_AnnBx)
GetAnnotationRect(Front, AnnotB, B_AnnTy, B_AnnTx, B_AnnBy, B_AnnBx)
//Calculate Radius & Rotation Angle
ROInfo(A_AnnTx, A_AnnTy, A_AnnBx, A_CenterX, A_CenterY, RadiusA)
ROInfo(B_AnnTx, B_AnnTy, B_AnnBx, B_CenterX, B_CenterY, RadiusB)
If (RadiusA!=RadiusB)
{
B_AnnTx=B_centerX-RadiusA
B_AnnTy=B_centerY-RadiusA
B_AnnBx=B_centerX+RadiusA
B_AnnBy=B_centerY+RadiusA
}
RotAngle=slope(A_CenterX, A_CenterY, B_CenterX, B_CenterY)
}
If (SetsCount>=(Sets-ix))
{
If (nxx<1)
{
AnnotA=AnnotIDSave2.GetPixel(0, SetsCountB+1)
AnnotB=AnnotIDSave2.GetPixel(0, SetsCountB)
GetAnnotationRect(Front, AnnotA, A_AnnTy, A_AnnTx, A_AnnBy, A_AnnBx)
GetAnnotationRect(Front, AnnotB, B_AnnTy, B_AnnTx, B_AnnBy, B_AnnBx)
ROInfo(A_AnnTx, A_AnnTy, A_AnnBx, A_CenterX, A_CenterY, RadiusA)
ROInfo(B_AnnTx, B_AnnTy, B_AnnBx, B_CenterX, B_CenterY, RadiusB)
If (RadiusA!=RadiusB)
{
B_AnnTx=B_centerX-RadiusA
B_AnnTy=B_centerY-RadiusA
B_AnnBx=B_centerX+RadiusA
B_AnnBy=B_centerY+RadiusA
}
RotAngleTemp=slope(A_CenterX, A_CenterY, B_CenterX, B_CenterY) //Calculate rotation angle first
SetsCountB=SetsCountB+2
}
}
}
Image Temp_A, Temp_B, TempMask
Image TempAAA, TempBBB
Number xWidth, yHeight
// Rotational Symmetry
If (RotateSelect==2 || RotateSelect==3 || RotateSelect==4 || RotateSelect==6)
{
RotAngle=0
Image TempSymm_A=Rotation(ImagelD, A_AnnTy, A_AnnTx, A_AnnBy, A_AnnBx, RotAngle)
Temp_A=ImageCrop(TempSymm_A, RadiusA, 1)
}
}

```

```

Image TempSymm_B=Rotation(ImageID, B_AnnTy, B_AnnTx, B_AnnBy, B_AnnBx, RotAngle)
If (RotateSelect==2)
{
  RotAngle=DegToRad(180)
}
If (RotateSelect==3)
{
  RotAngle=DegToRad(120)
}
If (RotateSelect==4)
{
  RotAngle=DegToRad(90)
}
If (RotateSelect==6)
{
  RotAngle=DegToRad(60)
}
Temp_B:=ImageCrop(Rotate(TempSymm_B, RotAngle), RadiusA, 1)
Temp_A.SetName("Disk A_Set "+(SetsCount+1))
Temp_B.SetName("Disk B_Set "+(SetsCount+1))
}

//Create a mask
Get2Dsize(Temp_A, xWidth, yHeight)
TempMask=Mask(TempMask, A_AnnBx, A_AnnTx, xWidth, yHeight, 0.9)
Number NoOfPixels=sum(TempMask) //number of pixels inside the created mask
Temp_A=Temp_A*TempMask
Image Temp_AA, Temp_BB, FlipTemp
Temp_B=Temp_B*TempMask
Temp_B.SetName("Disk B_Set "+(SetsCount+1))
// Cross-correlation coefficient
Number Temp_XCross=XCORR(Temp_A, Temp_B, TempMask, NoOfPixels)
//Sum of intensity of discs, for weighted gamma use
Number IntensityA, IntensityB, IntensityAB
IntensityA=sum(Temp_A*TempMask)
IntensityB=sum(Temp_B*TempMask)
IntensityAB=(IntensityA+IntensityB)/2
//Return values
If (SetsCount<(Sets-ix))
{
  Result("\nSet "+(SetsCount+1)+" "+" "+Temp_XCross+" "+IntensityAB)
}
Else
{
  Result("\nSet "+"m"+(SetsCount-(Sets-ix)+1)+" "+Temp_XCross+" "+IntensityAB)
}
CrossCorrelationCoeff=CrossCorrelationCoeff+Temp_XCross
//numerator
Temp_CrossCorrelation=Temp_CrossCorrelation+Temp_XCross*IntensityAB
//denominator
TotalIntensity=TotalIntensity+IntensityAB
Temp_A.DeleteImage()
Temp_B.DeleteImage()
SetsCount++
}
Result("\n\nWeight "+Temp_CrossCorrelation/TotalIntensity)
If (Delete==1)
{
  DeleteOvals(front)
}
}

// This quantifies the BF symmetry
void BF(image front, Number x0, Number y0, Number r0, Number RotAngleTemp, Number mode)
{
  ImageDisplay ImgDisp = front.ImageGetImageDisplay(0)
  Number xsize = front.ImageGetDimensionSize(0)
  Number ysize = front.ImageGetDimensionSize(1)
  Number A_AnnTy, A_AnnTx, A_AnnBy, A_AnnBx
  A_AnnTx = x0 - r0
  A_AnnTy = y0 - r0
  A_AnnBx = x0 + r0
  A_AnnBy = y0 + r0

  //Temporary scrap image for rotate , mask & crosscorrelate
  Image TempScrap:=RealImage("Temp Scrap", 4, xsize, ysize)
  TempScrap=ImgDisp.ImageDisplayGetDisplayedImage()
  Number ImageID=GetImageID(TempScrap)
  Image TempAAA, TempBBB
  Image TempMask, Temp_A, Temp_B
  Number xWidth, yHeight, NoOfPixels, RotAngle

  if (mode == 1) // mirror
  {
    TempAAA=Rotation(ImageID, A_AnnTy, A_AnnTx, A_AnnBy, A_AnnBx, RotAngleTemp)
    TempBBB=Rotation(ImageID, A_AnnTy, A_AnnTx, A_AnnBy, A_AnnBx, RotAngleTemp)
    xWidth = TempAAA.ImageGetDimensionSize(0)
    yHeight = TempAAA.ImageGetDimensionSize(1)
    TempMask=Mask(TempMask, A_AnnBx, A_AnnTx, xWidth, yHeight, 0.9)
    NoOfPixels=sum(TempMask)
    // Generate Mask Image -> generate mirror image -> apply
    Temp_A=TempAAA*TempMask
    Temp_A.SetName("aligned BF")
    FlipVertical(TempBBB)
  }
}

```

```

Temp_B=TempBBB*TempMask
Temp_B.SetName("mirror applied BF")
Number Temp_XCross=XCorr(Temp_A, Temp_B, TempMask, NoOfPixels)
Result("\nBF disk "+Temp_XCross)
}
else // rotational symmetry
{
    RotAngle=0
    Image TempSymm_A=Rotation(ImageID, A_AnnTy, A_AnnTx, A_AnnBy, A_AnnBx, RotAngle)
    Image TempSymm_B=Rotation(ImageID, A_AnnTy, A_AnnTx, A_AnnBy, A_AnnBx, RotAngle)
    Temp_A=ImageCrop(TempSymm_A, r0, 1)
    //Create a mask
    xWidth = Temp_A.ImageGetDimensionSize(0)
    yHeight = Temp_A.ImageGetDimensionSize(1)
    TempMask=Mask(TempMask, A_AnnBx, A_AnnTx, xWidth, yHeight, 0.9)
    Number NoOfPixels=sum(TempMask)
    if (mode==2)
    {
        RotAngle=DegToRad(180)
    }
    if (mode==3)
    {
        RotAngle=DegToRad(120)
    }
    if (mode==4)
    {
        RotAngle=DegToRad(90)
    }
    if (mode==6)
    {
        RotAngle=DegToRad(60)
    }
    Temp_B:=ImageCrop(Rotate(TempSymm_B, RotAngle), r0, 1)
    Temp_A=Temp_A*TempMask
    Temp_A.SetName("Aligned BF")
    Temp_B=Temp_B*TempMask
    Temp_B.SetName("Rotated BF")
    Number Temp_XCross=XCorr(Temp_A, Temp_B, TempMask, NoOfPixels)
    Result("\nBF "+Temp_XCross)
}
}

// Two vectors drawn manually with line annotations:
// g= (gflag*gx, gflag*gy)
// h= (hflag*hx, hflag*hy)
image img
if(!GetFrontImage(img) )
{
    OkDialog("You must have an image to operate on!")
    exit(0)
}
number nrow, ncol, zsize
ncol = img.ImageGetDimensionSize(0)
nrow = img.ImageGetDimensionSize(1)
number i, j, ann, anntype, annot, maskid
number row1, col1, row2, col2, col0, row0, row3, col3
annot = CountAnnotations(img)

//find two base lines marked on the image
j=0
for (i = 0; i< annot; i++) {
    ann = GetNthAnnotationID(img, i)
    anntype = AnnotationType(img, ann)
    if (anntype == 2) { // a line
        j += 1
        if (j==1) GetAnnotationRect(img, ann, row0, col0, row1, col1)
        if (j==2) GetAnnotationRect(img, ann, row2, col2, row3, col3)
        if (j==3) Result("Skipped lines after first two lines\n")
    }
}

if (j<2) // must have two line2
{
    OkDialog("Must have two lines")
    exit(0)
}

Image mask := CreateFloatImage( "mask", ncol, nrow )
mask = 0
imgdisp imgdisp = img.ImageGetImageDisplay(0)

if (imgdisp.ImageDisplayCountROIs() > 0)
{
    mask = 0
    imgdisp.ImageDisplayAccumulateROIsToMask( mask, 0, 0, nrow, ncol, 1 )
    maskid = 1
} else {
    mask = 1
    maskid = 0
}

number d1, d2, id=0
d1=(row0-row2)**2+(col0-col2)**2

```

```

if ( (d2=(row0-row3)**2+(col0-col3)**2) < d1) {
  id = 1
  d1 = d2
}
if ( (d2=(row1-row2)**2+(col1-col2)**2) < d1) {
  id = 2
  d1 = d2
}
if ( (d2=(row1-row3)**2+(col1-col3)**2) < d1) {
  id = 3
  d1 = d2
}

number gx, gy, hx, hy, x0, y0, gflag = 1, hflag = 1
if (id == 0) {
  x0 = (col0+col2)/2
  y0 = (row0+row2)/2
  gx = col1-x0
  gy = row1-y0
  hx = col3-x0
  hy = row3-y0
} else if (id == 1) {
  x0 = (col0+col3)/2
  y0 = (row0+row3)/2
  gx = col1-x0
  gy = row1-y0
  hx = col2-x0
  hy = row2-y0
} else if (id == 2) {
  x0 = (col1+col2)/2
  y0 = (row1+row2)/2
  gx = col0-x0
  gy = row0-y0
  hx = col3-x0
  hy = row3-y0
} else if (id == 3) {
  x0 = (col1+col3)/2
  y0 = (row1+row3)/2
  gx = col0-x0
  gy = row0-y0
  hx = col2-x0
  hy = row2-y0
}

if (abs(gx) < abs(gy)) {
  row0 = gx
  col0 = gy
  gx = hx
  gy = hy
  hx = row0
  hy = col0
}

if (gx < 0) {
  gx *= -1
  gy *= -1
  gflag = -1
}
if (hy < 0) {
  hx *= -1
  hy *= -1
  hflag = -1
}

// for 3R & 6R purposes
number tt = gflag*hflag*((gx*hx)+(gy*hy))
number angleSix
If (tt>0)
{
  angleSix=1
}
Else if (tt<0)
{
  angleSix=0
}

// Adjust circles interactively
number mag=1
gx /= mag
gy /= mag
hx /= mag
hy /= mag
number dx = gx/4
number dy = hy/4
number n0,n1,m0,m1
n0 = nint(1.5*(-x0)/dx)
n1 = nint(1.5*(ncol-x0)/dx)
m0 = nint(1.5*(-y0)/dy)
m1 = nint(1.5*(nrow-y0)/dy)

Result("Use following keys to adjust lattice, press Space to exit\n")
Result("0 to shift lattice\n")
Result("g to adjust 1st base vector\n")

```

```

Result("h to adjust 2nd base vector\n")
Result("Press arrow keys to make changes\n")
Result("r and R to adjust circle diameter\n")
Result("+ and - to adjust increment\n")
Result("T to switch on/off index \n")
Result("m to check mirror cross-correlation values\n")
Result("M to switch between mirror plane\n")
Result("2 to check Two-fold rotational cross-correlation values\n")
Result("3 to check Three-fold rotational cross-correlation values\n")
Result("4 to check Four-fold rotational cross-correlation values\n")
Result("6 to check Six-fold rotational cross-correlation values\n")

number px, py, r0 = 30, inc = 1
number key = 0, value, LabelText=1
id = 0
//specify the mirror direction
Number mX,mY
if(!getnumber("Enter mirror plane: vector g component="(gflag*gx+"+gflag*gy+")", 1, mX)) exit(0)
if(!getnumber("Enter mirror plane: vector h component="(hflag*hx+"+hflag*hy+")", 1, mY)) exit(0)

number N_hkl
if (!GetNumber("Estimated number of reflections? (odd squared)",25, N_hkl)) exit(0)
image AnnotationRegister:=ReallImage("Circle ID, type, x, y, radius, order, m, n", 4, 10, 2000)
image MirrorRegister:=ReallImage("Circle Order", 4, 15, 2000)
image TwoFoldRegister:=ReallImage("Two Fold Order", 4, 15, 2000)
image ThreeFoldRegister:=ReallImage("Three Fold Order", 4, 15, 2000)
image FourFoldRegister:=ReallImage("Four Fold Order", 4, 15, 2000)
image SixFoldRegister:=ReallImage("Six Fold Order", 4, 15, 2000)

Number Useful, RotAngleTemp=0
// Perform a while loop until space bar is hit
while(key != 32) //space bar
{
deleteovals(img)
DrawLattice(img,x0,y0,gx,gy,hx,hy,r0, N_hkl,LabelText)
DeleteOutBound(img)
// Get the key stroke...
key = GetKey()
if (key == 29) //right arrow key
{
if (id == 0) x0 += inc
if (id == 1) gx += inc
if (id == 2) hx += inc
}
else if (key == 28) //left arrow key
{
if (id == 0) x0 -= inc
if (id == 1) gx -= inc
if (id == 2) hx -= inc
}
else if (key == 30) //up arrow key
{
if (id == 0) y0 += inc
if (id == 1) gy += inc
if (id == 2) hy += inc
}
else if (key == 31) //down arrow key
{
if (id == 0) y0 -= inc
if (id == 1) gy -= inc
if (id == 2) hy -= inc
}
else if (key == 48) // "0" key
{
id = 0
}
else if (key == 103) //"g"
{
id = 1
}
else if (key == 104) //"h"
{
id = 2
}
else if (key == 114) //"r"
{
r0 -= inc
result("\n Radius="+r0)
}
else if (key == 82) //"R"
{
r0 += inc
result("\n Radius="+r0)
}
else if (key == 43) //"+"
{
inc *= 2
}
else if (key == 45) //"-"
{
inc *= 0.5
}
}

```

```

Else If (key == 77) //M
{
if(!getnumber("Enter mirror plane: vector g component=(+gflag*gx+","gflag*gy+)", 1, mX)) exit(0)
if(!getnumber("Enter mirror plane: vector h component=(+hflag*hx+","hflag*hy+)", 1, mY)) exit(0)
OpenResultsWindow()
Result("\n\n ***Now mirror plane is along (m,n)=(+mX+","mY+") \n")
}
Else If (key == 109) //m
{
OpenResultsWindow()
Result("\n\n ***mirror operation")
AnnotIDSave(img, AnnotationRegister, x0,y0,gflag*gx,gflag*gy,hflag*hx,hflag*hy,0)
MatchReflectionCircle(img,AnnotationRegister, MirrorRegister, mX, mY, Useful, 0)
Regenerate(img, MirrorRegister, Useful, r0, 1)
RotAngleTemp=Gamma(img,1)
BF(img, x0, y0, r0, RotAngleTemp, 1)
}
Else If (key == 50) //2R
{
OpenResultsWindow()
Result("\n\n ***Two-Fold Rotation operation")
AnnotIDSave(img, AnnotationRegister, x0,y0,gflag*gx,gflag*gy,hflag*hx,hflag*hy,0)
MatchTwoFold(img,AnnotationRegister, TwoFoldRegister,Useful,0)
TwoFoldRegenerate(img, TwoFoldRegister, Useful, r0)
GammaRotate(img,0,2)
BF(img, x0, y0, r0, RotAngleTemp, 2)
}
Else If (key == 51) //3R
{
OpenResultsWindow()
Result("\n\n ***Three-Fold Rotation operation")
AnnotIDSave(img, AnnotationRegister, x0,y0,gflag*gx,gflag*gy,hflag*hx,hflag*hy,0)
SixR(img,AnnotationRegister, ThreeFoldRegister,angleSix,3,Useful,0)
SixFoldRegenerate(img, ThreeFoldRegister, Useful, r0)
GammaRotate(img,0,3)
BF(img, x0, y0, r0, RotAngleTemp, 3)
}
Else If (key == 52) //4R
{
OpenResultsWindow()
Result("\n\n ***Four-Fold Rotation operation")
AnnotIDSave(img, AnnotationRegister, x0,y0,gflag*gx,gflag*gy,hflag*hx,hflag*hy,0)
FourR(img,AnnotationRegister, FourFoldRegister,Useful,0)
FourFoldRegenerate(img, FourFoldRegister, Useful, r0)
GammaRotate(img,0,4)
BF(img, x0, y0, r0, RotAngleTemp, 4)
}
Else If (key == 54) //6R
{
OpenResultsWindow()
Result("\n\n ***Six-Fold Rotation operation")
AnnotIDSave(img, AnnotationRegister, x0,y0,gflag*gx,gflag*gy,hflag*hx,hflag*hy,0)
SixR(img,AnnotationRegister, SixFoldRegister,angleSix,6,Useful,0)
SixFoldRegenerate(img, SixFoldRegister, Useful, r0)
GammaRotate(img,0,6)
BF(img, x0, y0, r0, RotAngleTemp, 6)
}
Else if (key == 84 ) // "T"
{
LabelText *= -1
}
}

Result("\n Center, g and h in (col, row) "+x0+" "+y0+" "+gflag*gx+" "+gflag*gy+" "+hflag*hx+" "+hflag*hy+"\n");
number gl, alpha, gy2, hy2
gl=sqrt(gx*gx+gy*gy)
gy2 = -gy //caution!
alpha=asin(gy/gl)*180/3.141592654
Result("g length angle "+gl+" , "+alpha+"\n");
gl=sqrt(hx*hx+hy*hy)
hy2 = -hy //caution!
alpha=asin(hy/gl)*180/3.141592654
if (hx < 0) {
if (hy < 0) alpha = -180-alpha
if (hy > 0) alpha = 180-alpha
}
Result("h length angle "+gl+" , "+alpha+"\n");
Image BasisVector = RealImage("",4,8,20+N_hkl)
BasisVector.SetName("Basis vectors for 0, g and h")
BasisVector.SetPixel(0,0,x0)
BasisVector.SetPixel(1,0,y0)
BasisVector.SetPixel(0,1,gx)
BasisVector.SetPixel(1,1,gy)
BasisVector.SetPixel(0,2,hx)
BasisVector.SetPixel(1,2,hy)
BasisVector.SetPixel(0,3,r0)
BasisVector.SetPixel(0,4,N_hkl)

BasisVector.Showimage()
BasisVector.SetDisplayType(5)

// Output all annotation info

```

```

// 0th-column:ID
// 1st-column:type
// 2nd-column:x position
// 3rd-column:y position
// 4th-column:radius
// 5th-column:order
// 6th-column:m
// 7th-column:n
// 8th, 9th-column:
//      1st-row:(x0,y0)
//      2nd-row:(gx,gy)
//      3rd-row:(hx,hy)
AnnotIDSave(img, AnnotationRegister, x0,y0,gflag*gx,gflag*gy,hflag*hx,hflag*hy,1)
AnnotationRegister.SetPixel(8,0,x0)
AnnotationRegister.SetPixel(9,0,y0)
AnnotationRegister.SetPixel(8,1,gflag*gx)
AnnotationRegister.SetPixel(9,1,gflag*gy)
AnnotationRegister.SetPixel(8,2,hflag*hx)
AnnotationRegister.SetPixel(9,2,hflag*hy)
ShowImage(AnnotationRegister)
AnnotationRegister.SetDisplayType(5)

// Copy Annotations and duplicate //
OkDialog("Proceed to duplicate images & annotations for image stack purpose. Press c to stop")
Image clonefront := img[0,0,0,ncol, nrow,1]
while(key != 99) // "c" key
{
    key = GetKey()
    deleteovals(img)
    DrawLattice(img,x0,y0,gx,gy,hx,hy,r0, N_hkl,LabelText)
    DeleteOutBound(img)
    If (key == 109) //m
    {
        AnnotIDSave(img, AnnotationRegister, x0,y0,gflag*gx,gflag*gy,hflag*hx,hflag*hy,0)
        if(!getnumber("Enter mirror plane: vector g component=(+gflag*gx+;+gflag*gy+)", 1, mX)) exit(0)
        if(!getnumber("Enter mirror plane: vector h component=(+hflag*hx+;+hflag*hy+)", 1, mY)) exit(0)
        MatchReflectionCircle(img,AnnotationRegister, MirrorRegister, mX, mY, Useful, 0)
        Regenerate(img, MirrorRegister, Useful, r0, 1)
        Image temp = clonefront
        CopyAnnotations(img, temp)
        ShowImage(temp)
        SetName(temp, "(clone)mirror "+mX+", "+mY+")")
    }
    Else If (key == 50) //2R
    {
        AnnotIDSave(img, AnnotationRegister, x0,y0,gflag*gx,gflag*gy,hflag*hx,hflag*hy,0)
        MatchTwoFold(img,AnnotationRegister, TwoFoldRegister,Useful,0)
        TwoFoldRegenerate(img, TwoFoldRegister, Useful, r0)
        Image temp = clonefront
        CopyAnnotations(img, temp)
        ShowImage(temp)
        SetName(temp, "(clone)Two-fold rotation")
    }
    Else If (key == 51) //3R
    {
        AnnotIDSave(img, AnnotationRegister, x0,y0,gflag*gx,gflag*gy,hflag*hx,hflag*hy,0)
        SixR(img,AnnotationRegister, ThreeFoldRegister,angleSix,3,Useful,0)
        SixFoldRegenerate(img, ThreeFoldRegister, Useful, r0)
        Image temp = clonefront
        CopyAnnotations(img, temp)
        ShowImage(temp)
        SetName(temp, "(clone)Three-fold rotation")
    }
    Else If (key == 52) //4R
    {
        AnnotIDSave(img, AnnotationRegister, x0,y0,gflag*gx,gflag*gy,hflag*hx,hflag*hy,0)
        FourR(img,AnnotationRegister, FourFoldRegister,Useful,0)
        FourFoldRegenerate(img, FourFoldRegister, Useful, r0)
        Image temp = clonefront
        CopyAnnotations(img, temp)
        ShowImage(temp)
        SetName(temp, "(clone)Four-fold rotation")
    }
    Else If (key == 54) //6R
    {
        AnnotIDSave(img, AnnotationRegister, x0,y0,gflag*gx,gflag*gy,hflag*hx,hflag*hy,0)
        SixR(img,AnnotationRegister, SixFoldRegister,angleSix,6,Useful,0)
        SixFoldRegenerate(img, SixFoldRegister, Useful, r0)
        Image temp = clonefront
        CopyAnnotations(img, temp)
        ShowImage(temp)
        SetName(temp, "(clone)Six-fold rotation")
    }
}
}

```


APPENDIX B:

PYTHON SCRIPT FOR SCBED SIMULATION

B.1. CBED simulation of $\text{Al}_{0.1}\text{CrFeCoNi}$ with random displacements

```

"""
A simple script to automate CBED simulation using scattering matrix method.
This example demonstrates the simulation of CBED patterns of  $\text{Al}_{0.1}\text{CrFeCoNi}$  HEA by:

1. Divide a crystal column into N blocks. Each block is randomly displaced from the ideal lattice.
2. Specify the mean, standard deviation of Gaussian distribution of the displacement (unit: fraction of unit cell)
3. Simulate CBED patterns and save into a single .img binary file (can be imported into DM)

Yu-Tsun Shao, PhD candidate,
University of Illinois at Urbana-Champaign, 2018
"""

# -*- coding: utf-8 -*-
import time
import numpy as np
import matplotlib.pyplot as plt
import subprocess

def safe_div(x,y):
    if y == 0:
        return 1
    return x / y

def cmd_Bloch(commands):
    subprocess.call(commands, shell=True)

def loading(filename):
    """Load data matrix from .img file; Return 2d array and the file header. """
    with open(filename, 'rb') as fin:
        dt_header = np.dtype([('ncol', 'i2'), ('nrow', 'i2'),
                              ('bytesperpixel', 'i2'), ('type', 'i2')])
        header = np.fromfile(fin, dtype=dt_header, count=1)[0]
        data = np.fromfile(fin, dtype='f4').reshape((header['ncol'],
                                                    header['nrow']))
    return data, header

# Displace the blocks which follows the random distribution
def RandomStrainBox(displ_mean, displ_std, N_slab, dz, N_scan):
    """ list of displacements along (column, probe_position) """
    JazzRndmColumn = np.zeros((N_slab, 5, N_scan)) ## (row, col, probe_position); [t1, t1+dt, disp_x, disp_y, disp_z]
    NameList = [] ## each probe position = 1 CBED pattern
    for probe in range(N_scan):
        rnd_dx = np.random.normal(displ_mean[0], displ_std[0], N_slab) ## a list of random numbers for each probe position
        rnd_dy = np.random.normal(displ_mean[1], displ_std[1], N_slab) ## a list of random numbers for each probe position
        rnd_dz = np.random.normal(displ_mean[2], displ_std[2], N_slab) ## a list of random numbers for each probe position
        f_temp = "probe_"+str(probe) ## temporary filename
        for mosaic in range(N_slab):
            t1 = int(mosaic*dz) ## [A]
            disp_x = "{0:.5f}".format(rnd_dx[mosaic])
            disp_y = "{0:.5f}".format(rnd_dy[mosaic])
            disp_z = "{0:.5f}".format(rnd_dz[mosaic])
            JazzRndmColumn[mosaic, :, probe] = np.array([t1, t1+dz, disp_x, disp_y, disp_z])
        NameList.append(f_temp)
        print("probe position at: ", probe)
    return NameList, JazzRndmColumn

## Generate input files for scbed.exe
def TXYZFile(thickness, dz, NameList, JazzRndmColumn):
    """For each probe position,
    generates a .xyz file according to NameList, JazzNBlues"""
    N_slab, rxyz, N_scan = JazzRndmColumn.shape
    for probe_position in range(N_scan):
        JazzNBlues = JazzRndmColumn[:, :, probe_position] ## the list for each probe position
        f_temp = NameList[probe_position] ## temporary filename
        ## writes the .dat file
        with open(f_temp+".xyz", 'w') as f:
            LineOne = "0.0 0.0 0.0 0.0 0.0 \n"
            f.writelines(LineOne)
            for i in range(len(JazzNBlues)):
                t1_temp = JazzNBlues[i][0] ## temporary t1
                t1_prime = JazzNBlues[i][1] ## temporary t1+dt
                disp_x = JazzNBlues[i][2]
                disp_y = JazzNBlues[i][3]
                disp_z = JazzNBlues[i][4]

                Lines = str(t1_prime)+" "+str(disp_x)+" "+str(disp_y)+" "+str(disp_z)+"\n"
                f.writelines(Lines)
            LastLine = str(thickness)+" 0.0 0.0 0.0 \n"
            f.writelines(LastLine)
        f.close()

```

```

## call the program scbed.exe
def StrainCBED_Bloch(fname, NameList, x0, y0, g_length, g_angle, npix):
    print("\n**Generating a .bzt file using Blochz.exe ...")
    commands = "blochz "+fname+".dat"
    cmd_Bloch(commands)
    print("\n**Generating .img files using SCBED.exe ...")
    for i in range(len(NameList)):
        f_temp = NameList[i] ## temporary filename
        ## now run the scbed.exe --> rename .img
        commandOne = "scbed "+fname+" "+f_temp+".xyz "+str(x0)+" "+str(y0)+" "+str(g_length)+" "+str(g_angle)+" -s "+str(npix)
        cmd_Bloch(commandOne)
        commandTwo = "rename "+fname+".img "+f_temp+".img"
        cmd_Bloch(commandTwo)
        print("progress: "+str(i+1)+" "+str(int(len(NameList)))+" images")
        ## removes the .xyz files
    for i in range(len(NameList)):
        f_temp = NameList[i] ## temporary filename
        try:
            os.remove(f_temp+".xyz")
        except OSError:
            pass

## Stack the CBED patterns into a binary file of image stack, which can be imported into DM with header of 8 bytes
def StrainCBED_stackIMG(fname_out, NameList, npix):
    CBED_array = np.zeros((npix, npix, len(NameList)))
    print("\n**Generating .img stack from .img files...")
    temp_data = np.empty([npix, npix], dtype='f4')
    f_temp = NameList[0] + ".img"
    useless_data, header = loadimg(f_temp)
    ## writes the output .img (stack)
    with open(fname_out+'.img', 'wb') as fout:
        fout.write(header)
        for i in range(0, len(NameList)):
            f_temp = NameList[i] + ".img" ## temporary filename
            temp_data, header = loadimg(f_temp)
            CBED_array[:, :, i] = temp_data
            temp_data = np.asarray(CBED_array[:, :, i], dtype='float32', order='C')
            fout.write(temp_data)
        fout.close()
    for i in range(len(NameList)):
        f_temp = NameList[i]
        try:
            os.remove(f_temp+".img")
        except OSError:
            pass
    print(" Done! ")
    ##return CBED_array

## This binary image file saves the displacements of individual block
def SaveJazzRandom(fname_out, JazzRndmColumn):
    datatype = np.dtype([('ncol', 'i2'), ('nrow', 'i2'), ('bytesperpixel', 'i2'), ('type', 'i2')])
    header = np.array([512, 512, 4, 2], dtype=datatype)
    N_slab, xyz, N_scan = JazzRndmColumn.shape
    temp_data = np.empty([N_slab, xyz], dtype='f4')
    with open(fname_out+'.DispList.img', 'wb') as fout:
        fout.write(header)
        for i in range(N_scan):
            temp_data = temp_data + np.asarray(JazzRndmColumn[:, :, i], dtype='float32', order='C')
            fout.write(temp_data)
        fout.close()

''' Input parameters '''
thickness = 1650 ## thickness of TEM specimen [units: Angstrom]
N_slab = 33 ## number of blocks
dz = 50 ## thickness of each block [units: Angstrom]
disp_mean = [0.0, 0.0, 0.0] ##[mean_x, mean_y, mean_z]
disp_std = [0.0055, 0.0055, 0.0055] ## 0.35% = 0.0035
N_scan = 625 ## 25x25 images

## file name
fname = "HEA" ## file name of the crystal data (.dat)
fname_out = fname+" "+str(thickness)+"_slab_"+str(N_slab)+"_mean_"+str(disp_mean)+"_std_"+str(disp_std)

## define output image format
x0 = 256 ## pixel x coordinate of (000) disk
y0 = 256 ## pixel y coordinate of (000) disk
g_length = 90 ## length of g, diffracted beam, in pixels
g_angle = 0 ## rotation angle of g
npix = 512 ## pixel size of the image

''' Run the functions '''
time_start = time.clock()
NameList, JazzRndmColumn = RandomStrainBox(disp_mean, disp_std, N_slab, dz, N_scan)
XYZFile(thickness, dz, NameList, JazzRndmColumn)
StrainCBED_Bloch(fname, NameList, x0, y0, g_length, g_angle, npix)
StrainCBED_stackIMG(fname_out, NameList, npix)
SaveJazzRandom(fname_out, JazzRndmColumn)
time_fin = time.clock()
print("time elapsed : "+str(time_fin - time_start))

```

APPENDIX C: INPUT DATA FILES FOR CBED SIMULATION

C.1. Data file of $(1-x)\text{Pb}(\text{Zn}_{1/3}\text{Nb}_{2/3})\text{O}_3-x\text{PbTiO}_3$ ($x=0.08$) (see J.-M. Kiat *et al.*, Phys. Rev. B 65, 064106 (2002) for atomic positions)

```
#!Written by QED, (C) JM ZUO
#!crystal
crystal PZN-8PT: dw = iso occ = par
cell 4.06080 4.00840 4.05290 90.000 90.250 90.000
atom Pb#1 0.000000 0.000000 0.000000 2.8000 1.00000
atom Zn#1 0.528900 0.500000 0.474800 0.6300 0.30330
atom Nb#1 0.528900 0.500000 0.474800 0.6300 0.60670
atom Ti#1 0.528900 0.500000 0.474800 0.6300 0.09000
atom O#1 0.588200 0.000000 0.456100 0.2600 1.00000
atom O#2 -0.006000 0.500000 0.528500 1.0300 1.00000
atom O#3 0.523500 0.500000 0.009000 0.1700 1.00000
spg 6 1

#! diffraction condition
hv 200.00
zone 1 1 0
norm 1 1 0
kt 0.000000 0.000000 0.000000
xaxi 0 0 1
kmax 0.115000
samp 16

# beam selection rules
sele 2.000000 3.5 0.1 0
sgmin 0.3
omeg 20.0

# define output
aper 1.5
abs 0.0
```

C.2. Data file of tetragonal BaTiO_3 (see A. Rother *et al.*, Phys. Rev. B 74, 134116 (2006) for atomic positions)

```
#!Written by QED, (C) JM ZUO
#!crystal
crystal tetragonl BTO: dw = uij occ = par
cell 3.994600 3.994600 4.038800 90.000000 90.000000 90.000000
atom Ba#1 0.000000 0.000000 0.000000 0.00560 0.00560 0.00630 0.00000 0.00000
0.00000 1.00000
atom Ti#1 0.500000 0.500000 0.488300 0.00760 0.00760 0.00760 0.00000 0.00000
0.00000 1.00000
atom O#1 0.500000 0.500000 0.024700 0.00770 0.00770 0.00550 0.00000 0.00000
0.00000 1.00000
atom N#1 0.500000 0.000000 0.513900 0.00740 0.00670 0.00860 0.00000 0.00000
0.00000 1.00000
spg 99 1

#! diffraction condition
hv 200.00
zone 1 0 0
norm 1 0 0
```

```

kt 0.000000 0.000000 0.000000
xaxi 0 0 1
kmax 0.120000
samp 32

# beam slection rules
sele 2.000000 3.5 0.1 0
sgmin 0.3
omeg 20.0

# define output
aper 1.5
abs 0.0

```

C.3. Data file of FCC Al_{0.1}CrFeCoNi (see Y. Hu *et al.*, *Comm. Phys.* **1**, 61 (2018) for composition)

```

#!Written by QED, (C) JM ZUO
#!crystal
crystal Al0.1CrFeCoNi : dw = iso occ = par
cell 3.5900 3.5900 3.5900 90.0000 90.0000 90.0000
atom Al 0.000000 0.000000 0.000000 0.800000 0.023600
atom Co 0.000000 0.000000 0.000000 0.800000 0.251500
atom Cr 0.000000 0.000000 0.000000 0.800000 0.244800
atom Fe 0.000000 0.000000 0.000000 0.800000 0.250400
atom Ni 0.000000 0.000000 0.000000 0.800000 0.229400
spg 225 1

#! diffraction condition
hv 200.00
zone 0 0 1
norm 0 0 1
kt 0.000000 0.000000 0.000000
xaxi 2 0 0
kmax 0.260000
samp 32

# beam slection rules
sele 2.000000 3.5 0.1 0
sgmin 0.3
omeg 20.0

# define output
aper 1.5
abs 0.0

```